`

INVESTIGATION INTO CONDUCTIVE PATTERNS AND RECEPTOR DESIGNS FOR EFFECTIVE LIGHTNING INTERCEPTION

By

Sidharth Arunkumar

Submitted in Partial Fulfillment
of the Requirements for the

Master of Mechanical Engineering
Specialization in *Solid Mechanics*

New Mexico Institute of Mining and Technology
Department of Mechanical Engineering

Socorro, New Mexico
(September, 2017)

`

ABSTRACT

This research presents an investigation of the electrostatic effects of changing receptor shapes on wind turbine blades. Existing research regarding lighting receptors are based on material definition, and the effects of lightning damage once it enters the composite laminates. Very limited research is found on the effect of changing the shape of the receptor to increase lightning capture efficiency. Literature and previous studies regarding lightning have proven that shape of the lightning receptor has a vital role in attracting lightning towards it, hence the widespread use of the lightning rod as a receptor due to the concentration of electric field on the sharp tip, which attracts lightning towards it. Turbine blades being one of the most lightning prone regions of the turbine needs to be well protected against lightning, and as such, the current research focuses on changes in receptor shapes to increase the peak electric field at the turbine tip, which could potentially increase the lightning capture efficiency.

Through the current research, numerical models of new receptor designs are developed, which show increase in electric field, compared to standard circular receptors in use today. High voltage tests were done to observe the general behavior of spark propagation, and attachment. Using results from such observations, new designs are proposed as possible replacement for current receptor shapes. In addition, some limitations of electrostatic analysis were found, which could be alleviated by developing dynamic spark propagation models.

Keywords: Lightning receptors, Lightning Electric field, Finite Element Modelling, Conductive patterns, blade lightning receptor

`

ACKNOWLEDGEMENTS

I would like to express my sincere gratitude to my academic advisor Dr. Ashok Ghosh, for allowing me to undertake this work and whose guidance has supported me throughout my Masters and in this research.

I would also like to thank my research advisor, Dr. Richard Sonnenfeld, who has provided immense technical support and constant encouragement throughout my research, without which this work would never have been possible. I am also grateful to my thesis committee member, Dr. Donghyeon Ryu, for sharing his expertise towards the development of my research, and for providing the feedback for writing my thesis.

My sincere thanks goes to Dr. Chelsea Hargather, Gary Chandler, Dr. Clinton Richardson, Dr. Ashok Ghosh and Dr. Julie Ford for providing me with teaching assignments and projects during the course of my Masters, which has not only helped in financing my education at New Mexico Tech, but was immensely helpful in developing my skills and deeper understanding of engineering and professional communication. These assignments have been some of the biggest sources of my education and learning here at New Mexico Tech, and it would not have been possible without the opportunities they provided to me.

I would also like to thank my colleagues at New Mexico Tech – Anant Agarwal, for the countless discussions and encouragement about how to make the most use out of the opportunities open to us – within and outside NMT; Varun Rao, for the immense help he provided in securing funding for my studies, and for the work we have accomplished together in developing our communication skills; Amrut for his leadership in the extra-curricular activities we were involved in – and to everyone else who have made my time in New Mexico Tech memorable and fun-filled. In addition, I would like to appreciate the time and effort taken by Edward Gangemi, to help in fabricating the experimental setup for this study.

Finally, I express the deepest gratitude towards my family, who have always supported me in all my endeavors and constantly pushed me to achieve my true potential. I will always be indebted to my Dad, Mom, Sister and Fiancé, for the person I am today, and for giving me the encouragement to achieve my goals in the future.

TABLE OF CONTENTS

`

`

LIST OF TABLES

`

LIST OF FIGURES

`

`

`

`

`

`

`

LIST OF ABBREVIATIONS AND SYMBOLS

CFRP   Carbon Fiber Reinforced Polymer

LPS   Lightning Protection System

EWEA   European Wind Energy Association

UNFCCC   United Nations Framework Convention on Climate Change

GWEC   Global Wind Energy Council

ROW   Rest Of the world

RF   Radio Frequency

LMA   Lightning Mapping Array

IC   Intra Cloud

GFRP   Glass Fiber Reinforced Polymer

IEC   International Electro-technical Commission

SAE   Society of Automotive Engineers

FEM   Finite Element Method

UV   Ultra-violet

HV   High Voltage

NREL   National Renewable Energy Laboratory

I_{peak} Peak current through lightning channel (kA)

ξ Length along lightning leader (m)

$\rho(\xi)$ Charge per unit length (C/m)

Z_0 Leader tip height above ground surface (m)

H   Height of cloud surface above ground (m)

E   Electric field (V/m)

`

ρ_v Charge source (C)

φ Electric potential

ε_o Permittivity value of air

r   Radius of lightning channel
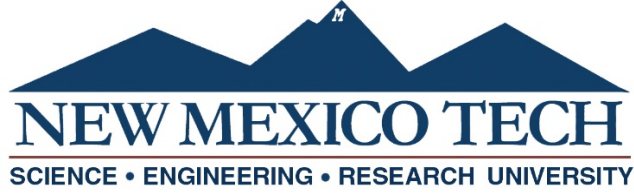
This thesis is accepted on behalf of the faculty
of the Institute by the following committee:

Dr. Ashok Ghosh

_____

Academic Advisor

Dr. Richard Sonnenfeld

_____

Research Advisor

Dr. Richard Sonnenfeld

_____

Committee Member

Dr. Donghyeon Ryu

_____

Committee Member

I release this document to New Mexico Institute of Mining and Technology

Sidharth Arunkumar

_____   _____

Student Signature   Date

CHAPTER 1 . INTRODUCTION

OVERALL RESEARCH GOAL

The objective of this research is to develop a novel lightning protection receptor consisting of patterned conductive elements, potentially providing increased lightning strike attachment efficiency compared to lightning receptors, while being considerably cheaper and lighter than a completely covered metal mesh, or conductive layer.

Researchers in the field of lightning protection point towards the direction of improved lightning protections systems, which involves coating of CFRP (Carbon Fiber Reinforced Polymer) with special materials to effectively transport lightning strike away from non-conducting surfaces (Yokoyama et al., 2014).

Although there is significant research being done on lightning protection coatings and layers consisting of varying materials, scarce research is found about the effect of conductive patterns as LPS (Lightning Protection Systems) on the lightning attachment probability and subsequent damage on the composite surface. Literature suggests that a higher electric field would be ideal to intercept lighting towards the receptors and away from the composite blades (Hernandez et. al., 2010). The most commonly used LPS method makes use of the round receptor on turbine surfaces, while in theory, a receptor consisting of sharp edges would provide a higher electric field around it, which could potentially intercept lightning better.

Combining this hypothesis with the intent to develop a receptor network which can cover more of the blade surface to improve the lightning capture efficiency, the motivation for the current research is to study the impact of receptor shapes on electric field, and to generate pattern designs which could potentially offer better lightning protection to wind turbine blades by generating higher electric field. The current research aims at designing a more effective lightning attachment point for wind-turbine blades, which would increase probability of intercepting a lightning strike without adding weight to the turbine blade. Modeling of static electric fields was used and studies of laboratory sparks was done on test patterns to understand what factors were important in pattern design.

INTRODUCTION

In recent years, there has been a steady increase in the use of renewable energy for meeting power requirements across the globe. Wind energy, along with solar power have been key players in the renewable energy sector, and within the last 30 years, they have grown steadily to contribute a significant part of the global energy requirements. Wind

energy is the one of the fastest growing sources of electric energy with an installed capacity of more than 70 GW globally (Rachidi et. al., 2008).

Within the wind energy sector, there is a recent increase in commissioning of offshore turbines due to lower operational costs per kilowatt-hour along with steady and faster winds blowing at sea compared to land. These turbines are taller in size, and as such, there is an increased threat of lightning strikes on these taller turbine blades

Turbine blades are currently made from high strength composites for weight reduction. These non-conductive composite materials are susceptible to damage from lightning strikes. This damage requires the blade to either be repaired in-situ or replaced entirely. Either operation causes massive financial losses from repairs and turbine down-time. Damaged composites may be patched if damage is not too severe, but they lose structural strength in doing so. If the huge currents passing through the composites are not captured and diverted, it can cause various types of damage to the blade, including complete rupture and explosion (due to sudden expansion of internal gases). As such, an effective lightning protection system is an essential part of a wind turbine blade.

1.1 Recent developments in Wind Energy

During the period between 2005 and 2015, wind energy utilization within the European Union increased by three and half times to 142 GW at the end of 2015, with a wind energy production of 15.6% (EWEA-Annual Statistics, 2015) and further plans to achieve 27% wind energy production by the year 2030 (Arantegui et. al, 2017). In 2015, 12,800 MW of wind energy was added to the European Union, which was a 6.3% increase from the previous year. The total wind energy installed in Europe is currently 142 GW, and the energy contributions from different sources is shown in *Figure 1*.
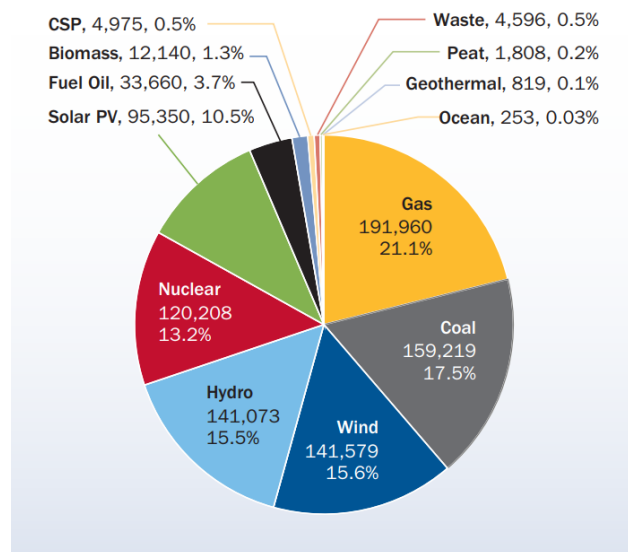
Figure 1 - Distribution of energy sources in Europe (EWEA-Annual Statistics, 2015)

`

Similar to the advances in the Wind energy sector shown in Europe, other nations are following suit to increase their presence in the renewable energy sector. With the advent of international agreements like the United Nations Framework Convention on Climate Change (UNFCCC), also known as the "Paris agreement", nations have come together to agree on policies that reduce the maximum global temperature increase to less than 1.5°C. Development of new wind turbine technologies is an important step in this direction because currently, 65% percent of the world's carbon emissions are due to the use of fossil fuels for electricity generation. The additionally installed wind turbines around the world in 2015 alone contributed to 4% of the global energy requirements.
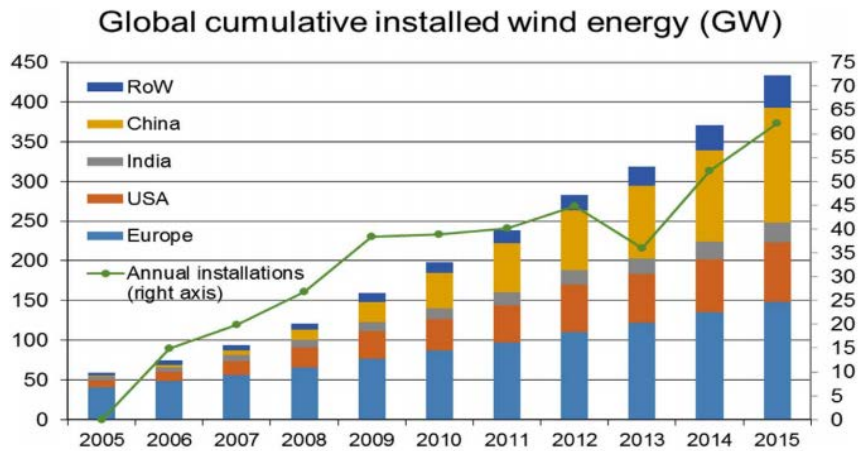
Figure 2 - GWEC's Annual market update adjusted for offshore installed but non-connected capacity in Europe, and other minor adjustments
(Arantegui et. al., 2017)

According to reports by the Global Wind Energy Council (GWEC), the global offshore installed wind energy increased steadily from 2005 to 2015 as shown in ***Figure 2***. The annual as well as cumulative offshore installed energy can be observed from the Figure for China, India, USA, Europe and the rest of the world (ROW). Both Total wind capacity and Annual additional capacity has increased steadily, with China leading the global market, closely followed by the USA and Germany.

1.2 Lightning Physics

It is well known that differential sedimentation of different hydrometeor types in thunderclouds leads to charge stratification. Typically there is a positively charged layer at 8-10 km from the ground, where glaciation is complete, and a lower negatively charged layer in the mixed phase region of the cloud where riming ice is present (Krehbiel et. al., 1986). These layers can be observed by balloon-borne electric field meters (Marshall et. al., 1982) or indirectly by RF (Radio-Frequency) emissions of the lightning. ***Figure 3*** (provided by R. Sonnenfeld) shows the charge layers in the cloud, measured by

5

an LMA (Lightning Mapping Array) and categorized by the RF emissions. Most lightning initiates between the main positive and negative charge layers, where the electric field is highest. Many flashes remain in the clouds (intra-cloud or IC flashes) while some propagate to ground. However, only the cloud-ground flashes are of concern to wind-turbine developers.

Figure 3 - Distribution of charge within clouds, recorded using LMA
(Image courtesy of Dr. R. Sonnenfeld)

The propagation of charge through the lightning channels occur through a mechanism called stepped leaders. The downward movement of charge towards the ground occurs in the form of approximately one microsecond long steps with intervals of the order of 50 microseconds between each downward step. This discontinuous movement of lightning discharge towards the ground is termed stepped leader. Even though the lightning leader propagates randomly through the air, the general trend it follows is the direction of highest electric field.

As the leader progressed towards the ground, at a certain distance, electric breakdown of the ground structure occurs, and an upward charge flow emanates from the structure, which is commonly called upward streamer, answering leader or connecting leader (Eriksson et al., 1979). This distance between the ground surface and leader tip is termed strike distance and the phenomenon connects the downward stepped leader and the ground structure through the connecting leader (*Figure 4*), causing the rapid and temporary flow of charge from the cloud to the ground, thus causing a "flash" of lightning.

`
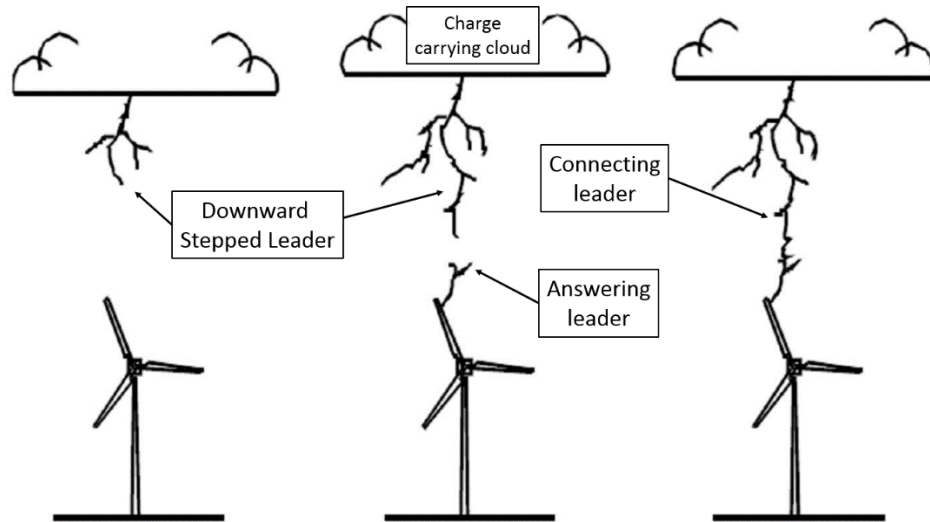
Figure 4 - Propagation of downward and connecting leaders (Lo et. al., 2008)

Lightning leaders are of two types – upward initiated and downward initiated leaders. In a downward initiated leader, the lightning stroke starts at the charged cloud surface and travels towards the grounded structure or ground place on the earth's surface. The upward initiated leader starts as a discharge from the earth's surface (or a grounded structure) and travels towards the charged cloud surface. These lightning strokes can be further classified as negative and positive flashes, where a negative flash carries negative charge from either the cloud or ground, and the positive flash is when the same phenomenon takes with positive charge. Roughly 90% of cloud-ground interactions are negatively discharges (Wessels et. al., 2002).

1.3 Lightning on Wind Turbines

Wind turbines tend to attract lightning for numerous reasons. Large hub height, sharp edges, pointy tips and constant blade rotation (Wen et al., 2016) makes the wind turbine a favorable target for lightning strikes. However, increased weight saving and size requirements warrant the need to use composite materials like Glass Fiber Reinforced Polymer (GFRP) and Carbon Fiber Reinforced Polymer (CFRP) as the turbine blade material, which significantly increases the risk of lightning strike damage, due to low electrical conductivity compared to metals. Composites used in turbine blades inherently have low dielectric strengths (Electric field at which a non-conducting material gets converted to a conductor) despite the favorable mechanical properties, making them susceptible to lightning strikes, if not protected with an effective LPS (Yokoyama et al., 2014).

As previously shown, since there is an increase in number of wind turbines being installed, and due to rapid increases in size of turbine designs, there is a subsequent higher risk of lightning strikes to turbine blades. Due to high-strength lightweight composites

being used for larger blade designs, the cost of repair or replacement of such blades are also much higher. (Lo, 2008) has recorded an increase in the number of lightning related damage to turbine blades in recent years. In addition, according to insurance claim reports, lightning strikes are one of the most reported causes of damage to wind turbines (*Figure 5*).
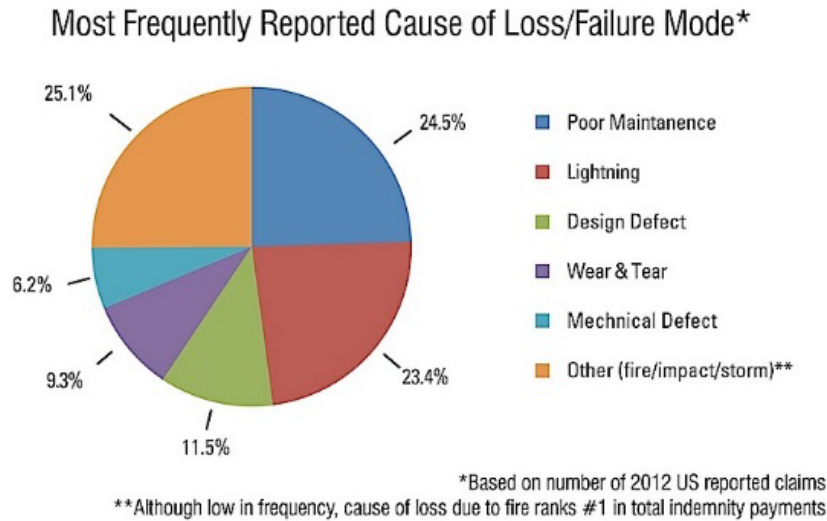
Figure 5 - Damage causes in Wind turbines as reported by insurance reports (Wang et. al., 2016)

1.3.1 Effect of turbine height on lightning strikes

While there has been considerable research to increase the power capacity of wind turbines, the easiest and most productive change in design has been found to be an increase in tower height and blade length. In essence, the ability to place the turbine rotor at an increased distance from the ground results in more power production, even at lower wind speeds.

Wind speeds increases with height from ground and as such, turbines are designed on taller towers to harness more power from turbines of the same rating. Researchers have stated that a 10 kW generator, if placed at a height of 100 m instead of 60 m from the ground, can produce 25% more power. However, this increase in power generation capabilities is accompanied by an increase in risk of lightning strikes on the blade tips during a thunderstorm (Lo et. al., 2008).

Any increase to the height of the structure will result in a direct increase in lightning strike probabilities on said structure. With increase in height, there are increased levels of systems and controls in place within the turbine, and a lightning strike on such a blade has the ability to disrupt these systems which keep the turbine operating smoothly.

`

In addition, wind turbines are commonly placed in elevated regions where higher speeds are found. Such places are also prone to frequent thunder storms. Wind turbine designs use 80m long blades currently (hub – tip), with a total turbine height of over 220 m from the ground (Lo et. al., 2008). Design of wind turbines in such locations and design specifications should include a comprehensive Lightning Protection System which ensures a high lightning capture efficiency.
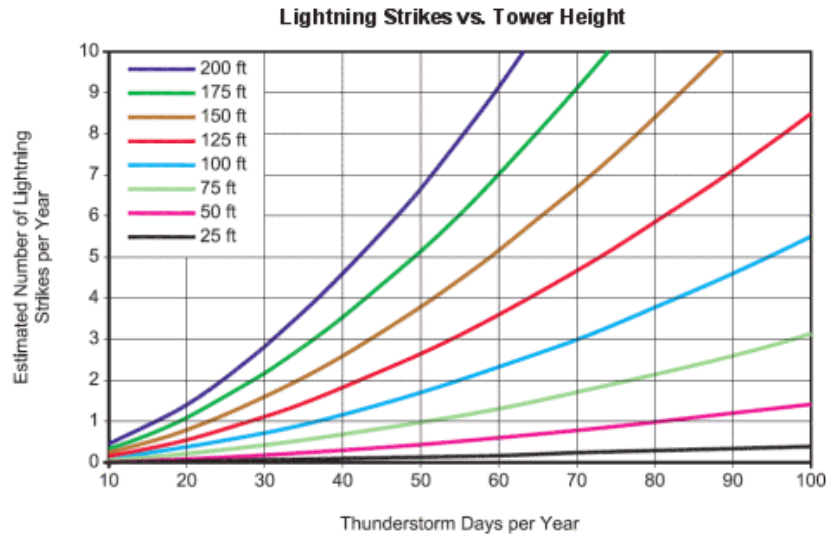
Figure 6 - Effect of tower height on lightning strikes per year
(Wang et. al., 2016)

Tower height of a lightning prone structure determines the probability of a lightning striking on it. ***Figure 6*** shows a graph of the trend of estimated lightning strikes per year for structures of increasing tower height. It is a rough representation of how the number of lightning strikes expected to strike a turbine increases with tower height.

1.3.2 Lightning induced damage on turbines

Studies regarding lightning strikes in Japan claim that 75% of all damage to wind turbines above 10,000 KW power rating are blade related, and 88% of lightning strikes occur on the blade tip region – which is commonly considered the last 3 m from the blade tip (Yokoyama, 2014; Garolera, 2016).

Dielectric strength of a material is defined as the electric field at which an insulating material breaks down into a conductor. Lightning strikes are considerably attracted to blade surfaces, because their sharp edges result in local electric field. Researchers also point out that lightning strikes falling on an unprotected blade have three routes for propagation: 1) Through the outer blade surface 2) Between composite laminates of the blade and 3) Within the inner blade cavity. Temperatures during lightning propagation can exceed 30,000 K

(Lo et. al., 2008), and the corresponding expansion of air accompanying this temperature rise is the root cause of the generation of a loud sound or "Thunder" when passing through open air.

A lightning strike has two major damaging effects on a wind turbine – the primary effect – also called "direct effects" are caused by the huge current loads passing through the turbine surface, causing thermal and dielectric breakdown with mechanical degradation. Secondary effects from the lightning strikes are caused due to electromagnetic effects acting on the auxiliary and control systems used to keep the turbine in smooth operation (Karegar, 2012; Lorentzou, 2004).

Materials commonly used for blade manufacturing are designed to withstand mechanical forces induced during turbine operation – however, it is not particularly designed for effective lightning mitigation. In some cases, the electric arc falling on the blade surface can travel to the inner cavity, causing substantial damage. The arc (consisting of extremely high temperature), rapidly heats up the air inside the cavity, resulting in its expansion with increase in pressure and subsequent explosion of the blade. This is one of the most damaging direct effects of lightning on the blade and as such, special measures should be taken to make sure the lightning arc would never enter the blade cavity.

The breakdown of air or any other non-conducting material happens in a similar manner, when there is an increase in electric field beyond the dielectric breakdown strength of the particular material. This occurs when the lightning strike attaches to the composite surface on a turbine blade. The heat generated is extremely high and rapid, causing a wide range of possible damages to the blade material, including delamination or complete rupture as shown in *Figure 7*.
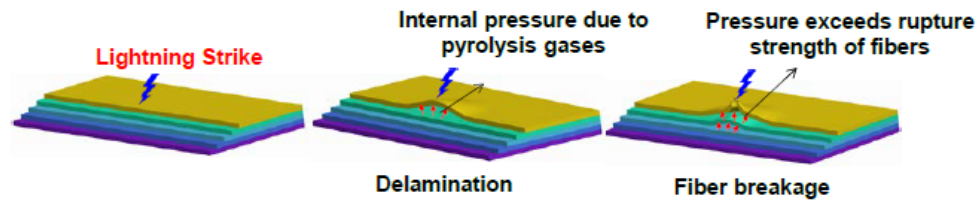
Figure 7 - Delamination and Laminate rupture caused due to rapid joule heating from Lightning attachment (Wang et. al., 2016)

Apart from lightning current conducting through the material thickness, sometimes it travels across the material surface until it reaches a ground surface. This phenomenon is called flashover and it occurs is cases where there are surface impurities, like dust and conductivity differences (*Figure 8*). The electric field required for surface flashover (flashover field strength) of a composite is less than the dielectric breakdown strength, and thus could occur at a lower electric field.
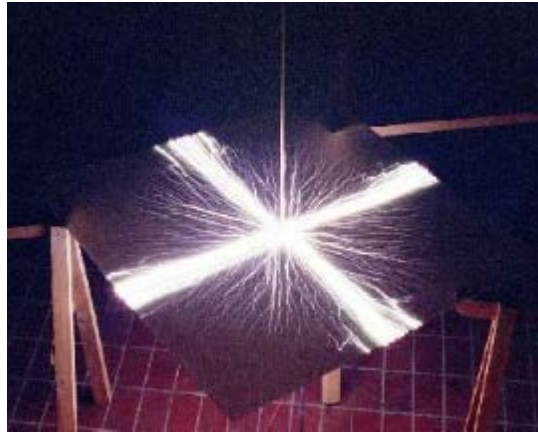
Figure 8 - Surface flashover on glass composite laminate
(Wang et. al., 2016)

Even in the presence of adequate LPS systems, surface impurities like salt content could alter turbine blade properties and cause subsequent lightning attachments. Wet surfaces on the blade sometimes results in conductive films, causing lightning damage to the underlying composites (Lo et. al., 2008). Research has been done on the Nikaho wind park, showing that a majority of the lightning strikes occurring on wind turbines take place on those turbines facing the coast (Yokoyama et al., 2014). This is expected to be the case due to excessive exposure to moisture and corrosive salts.

Another major cause of lightning damage in the presence of receptors is surface flashovers. They occur when the lightning attaches to a non-conducting part of the blade but does not penetrate the blade cross-section. Instead, the blade conducts the current on the composite surface, and ultimately it reaches a conductor on the blade – often a receptor. Although not as destructive as when the current penetrates the composite layer, this phenomenon still results in surface damages on the blade. This can occur due to winds blowing in the direction of the blade surface or due to rotation of the turbine blade (Wen et. al., 2016).

1.4 Lightning on Wind Turbines

During a lightning strike on a wind turbine, a charge gets transferred from the cloud surface through the formation of a lightning leader, to the turbine surface, which then travels through the structure to find a preferable route to ground. A lightning protection system consists of additional structures accompanying the wind turbine structure, which provides an easy and less resistant path to ground which avoids the sensitive composite components.

`

Conductive receptors are most commonly used as a Lightning Protections System, where discrete high conductivity metal discs are placed in highly lightning prone surfaces on the blade. These receptors are connected to a down-conductor within the blade, and the electric current is carried to the ground. One disadvantage of these lightning receptor systems is that the placement of receptors on discrete points on the blade is not very effective at lightning interception (Lorentzou et al., 2004). Some commonly used receptors systems as shown in *Figure 9*, includes discrete receptors at blade tips and a mesh covering the entire blade surface. While the disadvantages of using the receptors have been mentioned, using a mesh to cover the blade surface is extremely effective in protecting against lightning damage, however the advantage of using lightweight composites is lost due to weight of the heavy metal mesh.
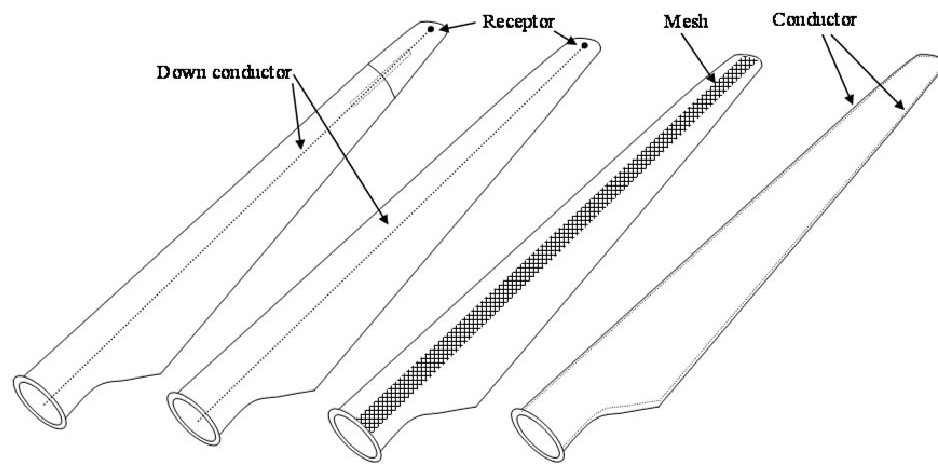
Figure 9 - Currently used turbine LPS systems (Peesapati et. al., 2011)

High peak currents from lightning can sometimes cause mild melting of the receptor material. They can even be blown out of the blade, due to either very high temperature increase of the receptor or due to the build-up of internal pressure within the blade cavity (Yokoyama et.al., 2014). Metal conductors should be designed carefully, since a smaller cross-section might not be sufficient to carry the huge current loads generated by lightning, and therefore the LPS system might get damaged or worse yet, the blade could get damaged. As such, a majority of the existing research tends to focus on blade damage and corresponding thermal analysis during a lightning strike.

Due to increase in blade lengths, the use of CFRP in wind turbine has gone up in recent times, because of their high strength to weight ratio, which is an extremely desirable property for wind turbine blade material. Since CFRP are electrically conductive in nature, it is suggested that they be bonded to the LPS system for effective protection against lightning. However, an issue to be considered while using CFRP as blade materials is the formation of eddy currents within the composite structures during high electric fields experiences when the blade reaches vertical position (tallest point). These eddy currents might create internal stresses within the CFRP laminates which can eventually result in a

`

crack (Rachidi et. al., 2008). One of the methods shown by (Rachidi, 2008) to reduce this effect is to use multiple down-conductors within the blade. The study showed that magnetic field generated within the blade were significantly reduced when two lightning down-conductors were used instead of one.

In addition to reducing damage due to direct lightning attachment, the proposed conductive patterns in our research could potentially have a much more favorable effect in reducing the magnetic field and corresponding eddy currents within the blade, as a conductive network of receptors is being designed.

`

CHAPTER 2 . LITERATURE REVIEW

Research related to lightning strike damage in wind turbines was dormant till 1994, where there was no considerable evidence to lightning striking a wind turbine – and subsequent damages (Lo et. al., 2008). However, in the last decade there has been a significant number of studies to observe and improve the effectiveness of turbine lightning receptors to capture the high currents safely.

There is abundant research to study composite materials and the effect of lightning strikes on it – however, studies about the effect of changing shape and size of the receptors on lightning attachment have been limited. Research about conductive patterns on turbine blades have been performed only to study the absorption of radiation falling on the wind turbine structures (from radars and telecommunication services) with such patterns, and not specifically for reduction in lightning induced damage. The pattern configuration including material thickness and mesh spacing in such studies have been optimized for radiation studies, and not for effective lightning protection (Kim et. al., 2012).

Discrete lightning receptors are extensively used as the LPS system for wind turbine blades currently. However, as mentioned earlier, research shows that lightning arcs attach to composite surfaces or enter the blade cavity even in the presence of receptors.

Figure 10 - Lightning attachment in Blade with receptor;
Modified from (Yokoyama et al., 2014)

Figure 10 shows an example of lightning attachment on a wind turbine test blade, and the corresponding damage to a blade tip with a receptor. Receptors greater than 3 mm thick and 1 cm in diameter are unlikely to be completely melted by even a direct strike. Studies of lightning rods at Langmuir Lab (Moore et. al., 2000) show that a direct hit on a

metal conductor produces a relatively small "divot" rarely exceeding 3 mm in diameter (**Figure 11**, courtesy R. Sonnenfeld). These effects are sometimes circumvented by the use of metal meshes to provide effective protection against electric arcing.

Figure 11 - Slight melting seen on lightning rods struck by a direct hit of lightning (Figure courtesy of R. Sonnenfeld)

Studies related to receptor design have broken into two categories. The more common studies are finite element studies of static electric field of structures in the presence of a simulated lightning leader or other electric field. These studies make an UNPROVEN assumption that lightning will attach at the location of highest simulated static field. The other type of study are field studies which show where lightning actually attaches on wind turbines. As part of literature review for the current research, the results of the field studies is presented first in this report.

Placement of lightning receptors is one of the crucial aspects of effectively protecting the blade structure. It has been observed that 90% of lightning attachments occur at the top 4 m of the turbine blade. A team of researchers (Garolera et. al., 2016) recently observed lightning damage on wind farms located in Texas, Illinois and Kansas over a period of 5 years. This research provides field data regarding the extent of lightning damage, and frequency over the lifetime of a wind turbine. The mentioned locations were selected because of the high average lightning flashes per year observed.

The researchers recorded all cases of lightning induced damage requiring major repairs in 508 wind turbines over the period of 5 years. These damages did not include

`

minor repairs or cosmetic damages. It also ignored damages occurring directly on the receptor system, but concentrated only on issues affecting the composite structure of the blade like delamination, punctures etc. All blades in consideration were equipped with some form of appropriate LPS system, but were commissioned before IEC standards were implemented.

From the 304 lightning cases that were recorded, it was observed that 60% of the lightning damage occur at the top 1 m of the blade, and 90% occurs at the top 4 m. The last 10% of blade damage was found to occur 10 m from the blade tip (*Figure 12*). This was found to be true for blades with both glass-based and carbon fiber based reinforcements.
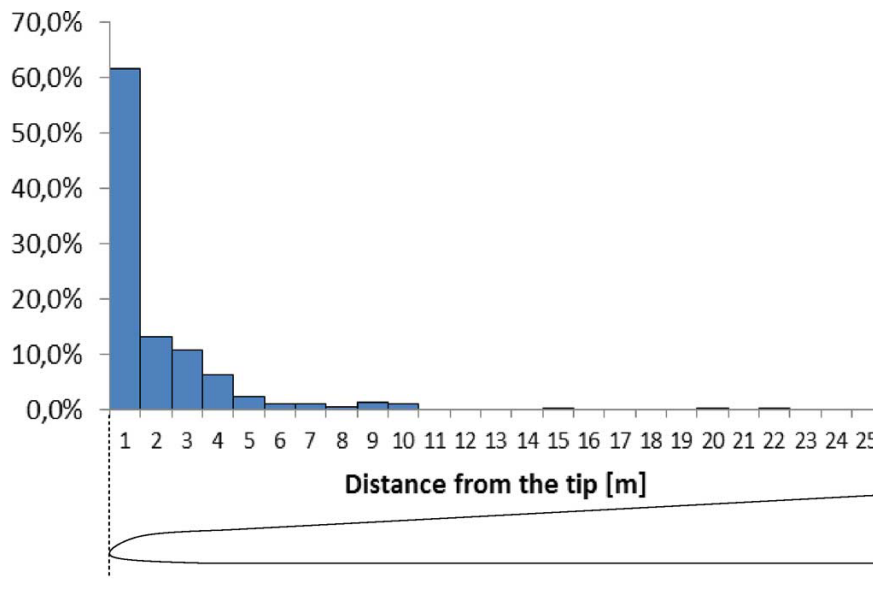
Figure 12 - Distribution of lightning damage on a turbine blade w.r.t. distance from tip (Garolera et. al., 2016)

It is also noted from the study that 59% of the lightning damage recorded had attached to the blade tip. Trailing and leading edges, along with spar caps are also points of interest, with 17% and 23% lightning damage respectively (*Figure 13*).

Thus, we can confirm that the blade tip is a crucial point of design consideration in terms of lightning protection. The reason for a large number of lightning damage caused might be due to the presence of more edges, a pointy edge or the tallest point on the turbine. Regardless, it can be agreed that blade tips (and immediately adjacent regions) should have lightning receptors with higher lightning interception efficiency.

`
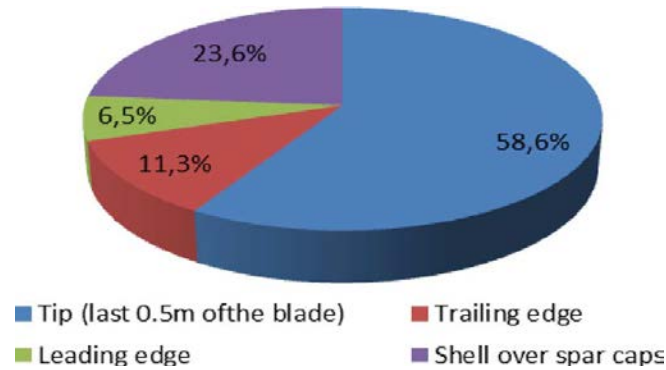
Figure 13 - Distribution of lightning damage on a turbine blade w.r.t. location (Garolera et. al., 2016)

2.1 Lightning on Wind Turbines

The implementation of LPS in turbine blades have posed a serious challenge for blade manufacturers. In the last 10 years, there have been some research into better methods of lightning protection, with manufacturers employing trial and error methods to solve the problem before that. The IEC 61400-24 standard, commonly used for setting design specifications for aircraft lightning protection systems have been updated to include LPS specifications for wind turbines. The standard highlights the importance of High Voltage and High Current testing to validate working of the LPS system. A range of voltage and current values has been described in the newly updated standard (Sorensen et. al., 2008).

Currently, the rolling sphere method is used to predict regions which fall outside the lightning protection zones, where an imaginary sphere is assumed to be tangent to the conductive surfaces on a structure. The regions in the vicinity which falls within the sphere is said to be protected from lightning. The radius of the rolling sphere depends on the peak current of the lightning leader (Refer *Eq. 1* in section 2.2), and the regions which fall outside these imaginary spheres are considered to be open to lightning strikes. This method inherently used in general lightning protection scenarios, is used to determine lightning prone regions on the turbine blade as well, which correctly identifies the blade tip as a potential lightning attraction point, but does not provide an effective method of lightning mitigation. It also does not provide adequate information about lightning protection of the turbine blade, which has a standard receptor. ***Figure 14*** shows the application of the Rolling sphere method on the entire wind turbine assembly to point out the turbine components highly prone to lightning strikes.

By observing ***Figure 14***, we can confirm that the blade tip area is highly prone to lightning strikes, and is not protected by the structure itself. Apart from generally identifying the high probability of lightning strikes on the top part of the blade, it does not provide analytical measures to determine the point of attachment on the blade. From field results, it has been seen that a majority of lightning strikes occur on the blade tip, even though according to the rolling sphere method, lightning can strike on any part of the exposed blade region on the top. This is one limitation of the IEC standard, which heavily

`

suggests the use of High Voltage and High Current testing, along with analysis and comparison with previously designed blades with effective LPS, to confirm the receptor efficiency while designing it (Sorensen et. al., 2008).
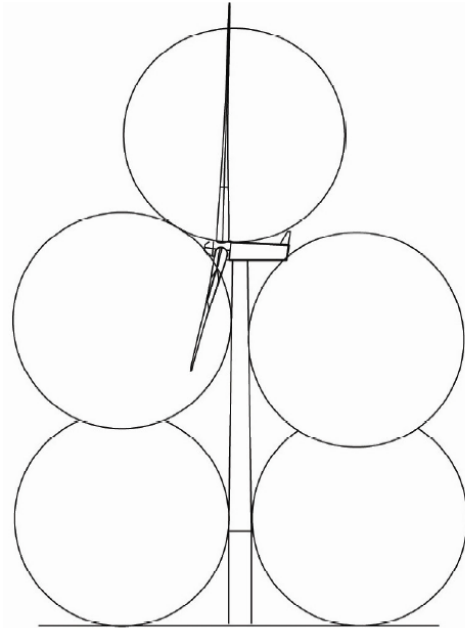
***Figure 14 - Application of rolling sphere method to turbine assembly
(Sorensen et. al., 2008)***

A lightning Protection System (LPS) installed in a wind turbine should be able to intercept an incoming leader preferentially over the surrounding blade surfaces, and to conduct the high currents towards ground without considerable damage. The ability of the conductor to intercept a leader towards it is termed Interception Efficiency, and the receptor's capacity to transport the current towards ground is coined as "Sizing efficiency". The product of these two terms is considered the overall Lightning Protection System efficiency. The sizing efficiency is dependent upon the material properties and cross-sectional area of the down-conductor, whereas, interception efficiency is dependent upon the shape, size and placement of the receptors (Wang, et. al., 2017).

Lightning protection levels are designated for different components by the respective standards, ranging from Category I to Category IV, depending on the peak current to be protected against – Level I being the highest protection level. For wind turbine blade tips, generally a Category 1 level protection is required for successful design. This would require a tolerance to extremely high currents (200 kA) and a well-designed receptor system to capture the lightning effectively. It could be argued that these standards describe lightning protection in terms of mainly sizing efficiency and does not provide enough specifications for interception efficiency. This is because the physics and engineering of

`

current conduction are well understood, while the physics of leader interception are complex and are NOT well understood.

Like author we try to apply rolling sphere to a typical wind turbine. The four lower spheres are all tangent to conductors. The uppermost sphere is tangent to the nacelle. The rolling sphere method does not assume that non-conductors (like turbine blades) count as lightning protection at all. It also does not cover the case of conductors embedded in non-conductors (like receptors).

High voltage tests are commonly used for determining the position of possible lightning attachment points and locating the placement of turbine receptors, whereas High current tests are generally done to determine the types and intensity of damage caused to the composite (or LPS system) due to the high currents passing through them during a lightning strike. In our study, we are concerned about the effectiveness of the proposed receptor system to capture lightning strikes, and not particularly the damage being imparted. Therefore, the experimental analysis of our research will include a High-Voltage test on receptors using a Marx generator.

Even though current parameters and waveforms vary for different lightning strikes, the maximum recorded peak current emitted by a lightning leader waveform is 200 kA. However, this is considered a rare occurrence and the average peak current value on a global scale is considered to be 30 kA. As such, this value is being considered for generation of lightning leader models in our research (Lo et. al., 2008).

Lightning waveforms can be simulated in labs, using the standard specified by SAE ARP5412 (SAE, 1999). *Figure 15* shows the industry standard current waveform used to design LPS systems. There are four strokes involved in one complete lightning strike: 1) Initial stroke 2) Intermediate stroke 3) Continuing stroke and 4) Restrike stroke. The initial stroke (also the first return stroke) consists of the highest peak current and lasts for a comparatively short time (50-500 μs), while the continuing stroke consists of a relatively smaller peak current but lasts much longer (0.25 to 1 s). Both these strokes contribute to the damage on composite materials in the form of joule heating. Multiple restrike strokes can occur during a lightning strike, however their peak currents are generally lower than the first return stroke. Therefore an LPS system designed for the initial stroke should be able to withstand subsequent restrikes (Component D).

Since replication of the entire SAE ARP5412 waveform is seldom feasible, parts of the waveform are created in a simulated high current analysis, and restrikes are often ignored when recreating the current waveforms in experimental setups.

As mentioned earlier, there are different levels of lightning protection specified by IEC for use in aircraft and wind turbine applications. These protection guidelines mainly have to do with the current carrying capabilities which is directly related to increasing the sizing efficiency. As covered earlier, the total efficiency of an LPS system is the product of sizing and interception efficiency (Wessels et. al., 2002). As such, detailed description of the Lightning protection guidelines does not apply to our study, since the aim here is to

`

only increase the interception efficiency by changing shapes and sizes of receptors, and introducing patterned conductors which exhibits higher electric fields, which in turn would potentially provide a higher likelihood of intercepting lightning strikes.

COMPONENT A (First Return Stroke)
       Peak Amplitude   :   200kA (± 10%)
       Action Integral   :   2 x 10⁶A²s (± 20%) (in 500μs)
       Time Duration   :   ≤ 500μs

COMPONENT B (Intermediate Current)
       Max. Charge Transfer   :   10 Coulombs (± 10%)
       Average Amplitude   :   2kA (± 20%)
       Time Duration   :   ≤ 5ms

COMPONENT C (Continuing Current)
       Amplitude   :   200 - 800A
       Charge Transfer   :   200 Coulombs (± 20%)
       Time Duration   :   0.25 to 1 s

COMPONENT D (Subsequent Return Stroke)
       Peak Amplitude   :   100kA (± 10%)
       Action Integral   :   0.25 x 10⁶A²s (± 20%) (in 500μs)
       Time Duration   :   ≤ 500μs

Figure 15 - Lightning current standard waveform as specified by
SAE ARP5412 (SAE, 1999)

2.2 Correlation between Lightning and Electric Field

Electric fields around receptors have shown to have an effect on probability of lightning attachment (Wen et al., 2016). In a recent study, an electric field model was set up using Comsol Multiphysics software and compared with calculated values. A similar study (Karegar et al., 2012) investigated the effects of voltage distribution from the lightning source to the entire length of the blade. The latter study was performed for

`

different configurations and placements of the receptor being currently used in the industry. Results showed that number and placement of receptors has a significant effect on the voltage distribution, and it was assumed also on the corresponding probability of lightning strike attachments. Similar models will be used for our research to determine the electric field variation and voltage distribution in different parts of the blade and the adjoining receptor, providing clarity on the possible shape, size and material needed for the novel LPS designs.

Higher electric field is believed to be an indication of a higher likelihood of the initiation of a lightning strike towards (or from) that point. Hernandez et. al., conducted research to study the causes of failures in wind turbines with receptors. He simulated the electric field generated on and around a wind turbine blade before a lightning strike. He used ANSYS APDL V12.1 to model the electric field simulation. Due to the use of multiple mesh refining techniques, a highly accurate model was created, which retained its accuracy even after small changes in geometry. The simulation as well as corresponding experiment showed that the metal parts within the blade assembly exhibited a higher electric field distribution, as expected.
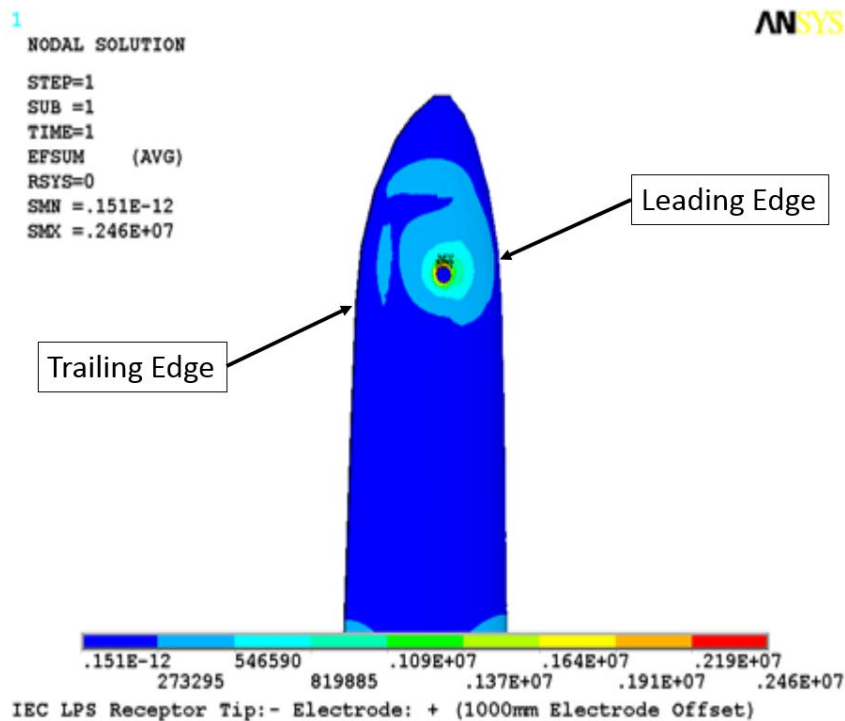
Figure 16 - Electric Field contour plot around receptor on Wind Turbine (Modified from Hernández et. al., 2010))

A 1-MV DC rectangular electrode was modelled, and the metal parts of the lightning receptors were linked to ground terminals. The simulation was conducted for GFRP and CFRP blade surfaces, using the respective density and relative permittivity

`

values of these materials. Since the receptors were the point of interest in this study, and since metals showed a concentration of electric field, composite materials used in this model were assumed to be isotropic in nature. This assumption is claimed to be acceptable after comparing with experimental results.

As expected, the metal receptors as well as the area surrounding the receptors showed a concentration of electric field, suggesting that there is an increased likelihood of lightning streamers initiating in this area. *Figure 16* shows the Electric Field contour plot generated by the model.

The results points out that in the presence of a lightning receptor, the surface immediately surrounding the receptor exhibits a high Electric Field distribution. This might be favorable for attracting lightning towards the receptor, but the high E-field on the blade surface surrounding the receptor may induce material breakdown and subsequent delamination. The maximum electric field magnitude recorded in this simulation is 2.5 MV/m, whereas breakdown in most materials requires at least 10 times this field. The reason for non-uniform distribution of electric field around the receptor as seen in *Figure 16* could be the placement of lightning leader/electrode in the simulation, or due to the presence of internal conductors, that have been modelled into the FEM simulation.

Figure 17 shows a graph highlighting the variation of Electric Field along four different paths on the turbine blade – namely the 1) Leading Edge, 2) Trailing Edge, 3) Pressure Side and 4) Suction Side.
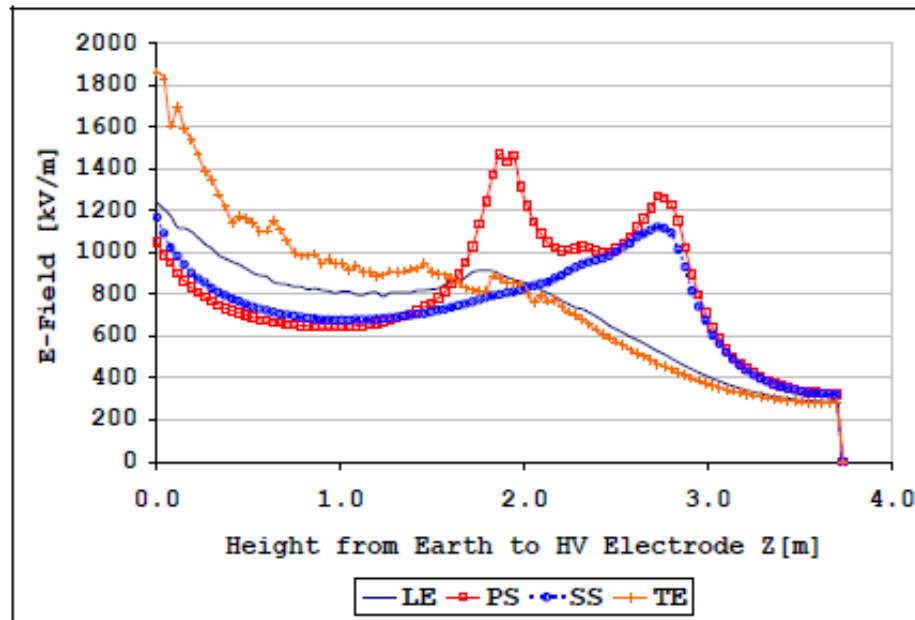
Figure 17 - Electric Field variation along 4 paths with distance from ground to electrode (Hernández et. al., 2010)

`

The results show that the paths in the vicinity of the metal receptors show an increase in Electric Field compared to the Trailing and Leading Edge. From the graph, it can also be observed that receptors places within the blade (and on one side in this case) have an effect on the electric field interactions along the surrounding geometry. The presence of a receptor on one side is seen to affect E-Field interactions along all 4 paths shown in this study.

A similar model was created to study the electric field around a tip-shaped receptor (on the blade tip). The results showed a decrease in the maximum Electric Field in this arrangement, with a highest value of 2.2 MV/m around the blade tip surface. Plots similar to *Figure 16* and *Figure 17* are presented in the research publication, showing that the electric field distribution around the tip shaped receptor is less than the round receptor, according to both the contour plot and the four paths chosen for observation.

Experimental validation for the models were done in a high voltage laboratory. The blade replica (along with receptors) was connected to ground, and placed at a distance of 4.5m from a rectangular electrode. An impulse voltage of 1 MV was applied to the electrode with both positive and negative polarity to observe the effects of downward and upward initiated lightning strikes. These experimental runs were recorded using a UV multi-spectral imaging tool, which uses optical imaging to identify areas of high electrical stress with an operating frequency of 50 Hz.

Figure 18 shows an example of the image obtained from experimental analysis. It validated the finding from FEM analysis, to show that an increase in Electric Field and subsequent streamer formation is found in areas near the receptor location. An interesting finding from this research is that streamers can emerge from either the receptor surface or from composite surfaces with a high electric field, surrounding the receptor. To reduce electro-magnetic effects, experimental validation was done for high voltage impulse testing inside a shielded cabinet.

Figure 18 - UV spectral image of blade with round receptor on one side
(Left – negative polarity; Right – Positive polarity) (Hernández et. al., 2010)

`

The highest point of Electric Field in each FEM models was identified using information from mesh elements. This point is assumed to be the highest probable lightning attachment point. A line joining this point and the HV electrode was made, which is claimed to be the most probable path for breakdown during a lightning strike. Results from experimental study also validated the electrical breakdown path obtained from simulation with close precision (Hernandez et. al., 2010). Results of electrostatic FEM analysis obtained in this study is similar to results from the current research. A concentration of electric field is seen around the receptor boundaries, to which the lightning streamer is prone to be attracted.

One of the major assumptions in this study is that the turbine is stationary, and as such, a steady state electrical analysis has been done. In practical scenarios, the effects of rotation and other dynamic effects might affect the functionality of receptors used.

Researchers from Warsaw University of Technology (Sul et. al., 2015) have also studied methods to determine optimal lightning protection systems and their effectiveness. There are few parameters that are overlooked when it comes to designing a lightning receptor system. The phenomenon of "Mutual screening" among conductive receptors on wind turbines and the effect of their geometries are not considered. Study of electric field distribution in the vicinity of blade tips and receptors during the last lightning step is crucial for predicting the possible attachment point. Areas around the receptor (or grounded surface) with low electric fields can be assigned as lightning protection zones. As such, we can make an assessment of the regions where probability of lightning attachment or initiation is low.

The model used in their study makes use of a 2x2 km square plane with the lightning leader emitting from the center of the upper plane, representing the charged cloud surface. The leader is represented by a straight line, and the spatial charge distribution is considered to be linear. The lightning leader consists of a non-uniform, but linearly increasing spatial charge distribution, with a higher charge towards the lower part of the leader. For simplifying the model, only the vertical components of Electric Field were considered. The assumed striking distance is 20m, corresponding to a maximum peak current of 3 kA for this study.

Figure 19 shows the geometries modelled to study the electrical field surrounding Lightning Protection zones. Three rectangular blocks have been modelled, to represent building, and for simplification, all the building walls are assumed to be grounded. The study was done for 40 points on the different surfaces of the building and for 9 different positions of the lightning leader emission.

From all 9 models, and data from the 40 points, certain regions of lightning protective zones were observed. These regions contained few points that did not exhibit high Electric Field for any of the 9 positions of lightning leader. This result assumes that these regions would not initiate or attract a lightning strike – no matter the position of the lightning leader, and can thus be assigned as a lightning protected zone. The author claims

`

this to be an apt method for testing the effectiveness of lightning receptors, and to determine if the structure in question is sufficiently protected from lightning.
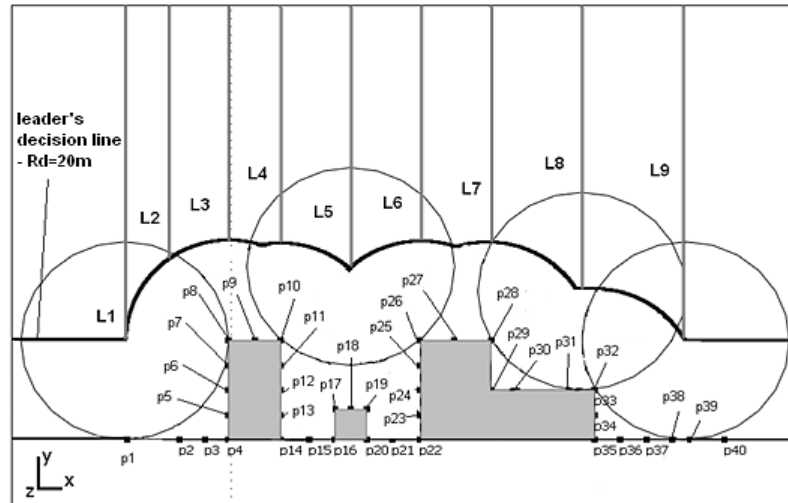
Figure 19 - Positions of lightning leaders and observation points.
(Sul et. al., 2015)
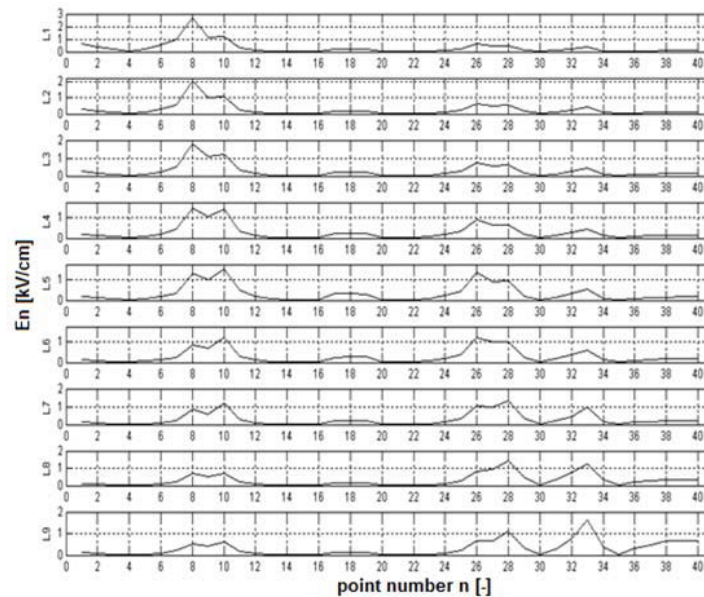
Figure 20 - Electric Field at different points for 9 leader positions
(Sul et. al., 2015))

The researcher goes on to claim that the calculation of electric field distribution around receptor structures prone to lightning is the correct method to determine the areas

`

prone to lightning and those that are protected from it. This is the modern method of designing lightning protection systems. In this system, parameters such as mutual shielding and geometry of lightning receptor are taken into consideration (Sul et. al., 2015).

An intricate model of a wind turbine with receptors was made by (Wang, 2016) using Comsol Multiphysics, to simulate the effects of receptor size and shape on the probability of lightning strikes on a turbine blade. These models are validated using experimental data obtained from tests on a turbine blade (Arinaga et. al., 2006). For ease of modelling, the author has assumed a static turbine model, and have correspondingly used static electric field analysis in Comsol. As opposed to a majority of prior research done in Electric field effects of lightning in Comsol modelling, the author has successfully used a non-uniform spatial charge distribution within the lightning leader model, which much more accurately represents actual lightning physics (Wang et. al., 2016).

The author, like other researchers in the field of lightning interception, assumes that larger electric fields provide higher attraction to lightning, and as such would be the most probable lightning attachment point. Therefore a receptor which exhibits a higher Electric field would potentially have a higher lightning interception efficiency.

In previous research to study the effect of electric field on lightning, simplistic models have been used for ease of modelling. However, in this study, an accurate model of the 5-MW NREL reference turbine was created using PRO-E, since it was observed that changes in geometry have a significant impact on electric field. As mentioned before, the dynamic effects of the turbine are ignored, but should be included for investigation in future studies. Distance between the lightning leader and turbine tip is calculated and modelled using the relation specified in rolling sphere method from the IEC61400-24 standard:

$$R = 0.6 \, (I_{peak})^{1.46} \qquad\qquad\qquad (Eq. \ 1)$$

where, R denotes the striking distance (in metres) and I_{peak} denotes the peak current during lightning propagation.

A 4x4x4 km cube was modelled, with a Boolean cutout of the NREL turbine in the center was modelled to represent the turbine surfaces and the ambient air. The cloud surface is represented by one of the cube surfaces on the top layer. A cutout was used such that ground surfaces can easily be assigned without the need to assign any material properties to either the ground or surrounding blade surfaces (*Figure 21*).

A cylindrical lightning leader channel was also modelled, which travels from the cloud surface till the turbine blade tip height. A striking distance between the lightning leader and turbine tip is maintained as calculated from *Eq. 1*. As mentioned earlier, one of the highlights in Wang's study is the use of non-uniform charge distribution within the lightning leader to represent lightning physics and corresponding electric field more accurately.
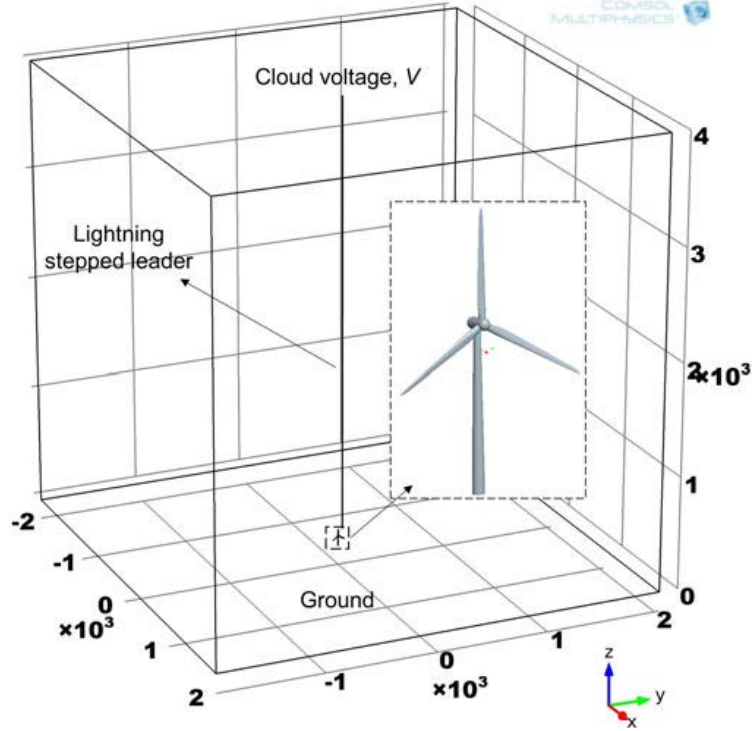
Figure 21 - 4x4x4 km wide Comsol model with turbine cut-out and lightning leader (Wang et. al., 2016)

There have been many proposed numerical models to represent the relationship between charge distribution and peak current. Models proposed by Golde, Eriksson, Cooray and the "Dellera and Garbagnati" models were reviewed by (Cooray, 2007) after which a more accurate leader charge distribution model was developed and presented (Cooray et. al., 2007).

Charge density within the lightning leader is in reality affected by field enhancements from grounded surfaces. As a result, when the lightning leader approaches ground, a concentration of charge density is observed. The charge density relation within the lightning leader channel, as derived by Cooray is as follows (Cooray et. al., 2007):

$$\rho(\xi) = a_o \left(1 - \frac{\xi}{H - Zo}\right) G(Zo) Ipeak + \frac{Ip(a + b\xi)}{1 + c\xi + d\xi^2} H(Zo) \qquad (Eq.\ 2)$$

$$G(Zo) = 1 - \left(\frac{Zo}{H}\right), \qquad (Eq.\ 3)$$

$$H(Zo) = 0.3\alpha + 0.7\beta, \qquad (Eq.\ 4)$$

$$\alpha = e^{-(Zo - 10)/75}, \qquad (Eq.\ 5)$$

$$\beta = 1 - \left(\frac{Zo}{H}\right), \qquad (Eq.\ 6)$$

27

`

where,

Z_o = Leader tip height above ground surface (m)

H = Height of cloud surface above ground (m)

$\rho(\xi)$ = Charge per unit length (C/m)

ξ = Length along lightning leader ($\xi = 0$ is at leader tip) (m)

I_{peak} = Peak current of return stroke (kA)

$a_o = 1.476 \cdot 10^{-5}$

$a = 4.857 \cdot 10^{-5}$

$b = 3.9097 \cdot 10^{-6}$

$c = 0.522$

$d = 3.73 \cdot 10^{-3}$

All receptor surfaces are assigned as ground terminals including the actual ground surfaces at the bottom of the model (surface on which turbine tower rests). All surrounding non-conducting surfaces are assigned with an open boundary condition (by default), which aptly represents the physics of a non-conducting surface. The 4 lateral surfaces of the cube representing ambient air is also assigned with this boundary condition. A 40 MV potential boundary condition is applied to the top surface representing the charged cloud surface.

The electric field due to the propagation of an assumed cylindrical lightning channel is given by:

$$\nabla \times E = 0 \qquad \qquad \text{(Eq. 7)}$$

$$\nabla \cdot E = \rho_v / \varepsilon_o \qquad \qquad \text{(Eq. 8)}$$

$$E = -\nabla \varphi \qquad \qquad \text{(Eq. 9)}$$

where,

E represents a tensor denoting electric field, and ρ_v is the charge source, given by:

$$\rho_v = \rho(\xi) / \pi r^2 \qquad \qquad \text{(Eq. 10)}$$

where, as represented in equation (2), $\rho(\xi)$ is the charge density of a lighting leader channel of radius r = 1.5m. φ represents electric potential and ε_o is the permittivity value of air. Relatively simple meshing parameters were used for this model, with a maximum edge length of 100 m and a minimum of 0.5m. A single tetrahedral mesh was used for the entire model, using Comsol V4.1.

Supporting the standard practice of testing the top 3m of a blade for lightning protection, the results show that the electric field from the blade root up to 3m from the tip showed very similar results for all receptor types. This shows that the effect of receptors to attract lightning takes effect only in the upper 3m of the blade tip (for a conventional receptor arrangement). In addition to the standard round and tip-shaped receptors, the author also models a double receptor arrangement which does not have any experimental counterpart for validation. The Electric field results in the top 3 m of the blade tip varies according to the receptor type and size. *Figure 22* shows the contrast between the electric field on a blade without any receptors and a blade with different receptor arrangements. The author plots the electric field along the trailing and leading edge to show the difference.
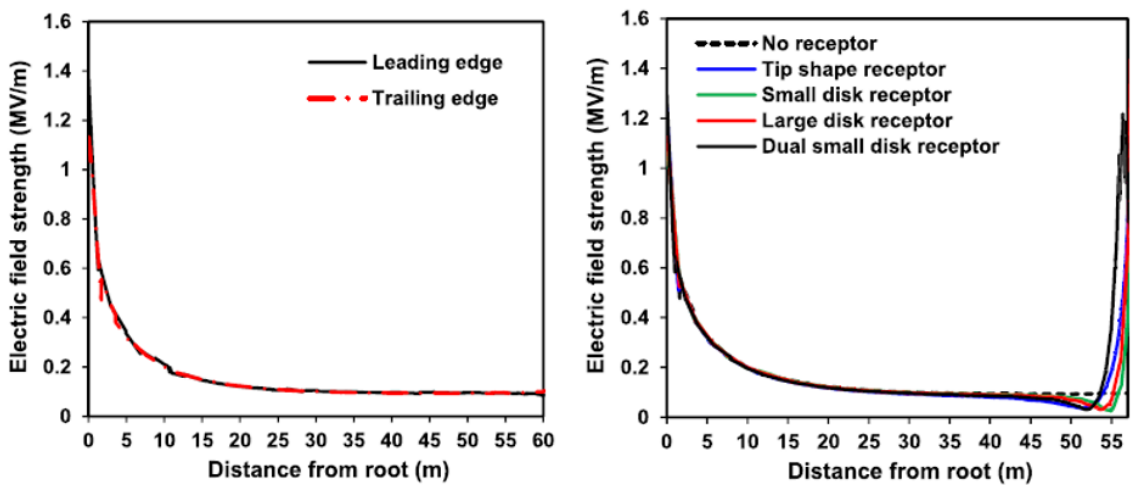
Figure 22 - Left: Blade without receptor; Right: Blade with receptors (Trailing Edge) (Wang et. al., 2017)

The study shows the maximum electric field along the leading and trailing edges as well as on the entire blade surface. While plotting electric field on the blade edges provide an idea about the effects of receptors, the maximum electric field, and subsequently better receptor is obtained from the surface contour plot as shown in *Figure 23*.

Figure 23 shows the maximum electric field obtained on the blade surfaces, which would act as the potential attachment point for lightning strikes. The claim from this research is that the receptor system with the highest electric field would potentially have a stronger attraction for lightning, being the better receptor for this blade. It should be noted that the experimental validation are qualitative in nature, as the physical model used is from different research and is not the same as the modelled blade.

`
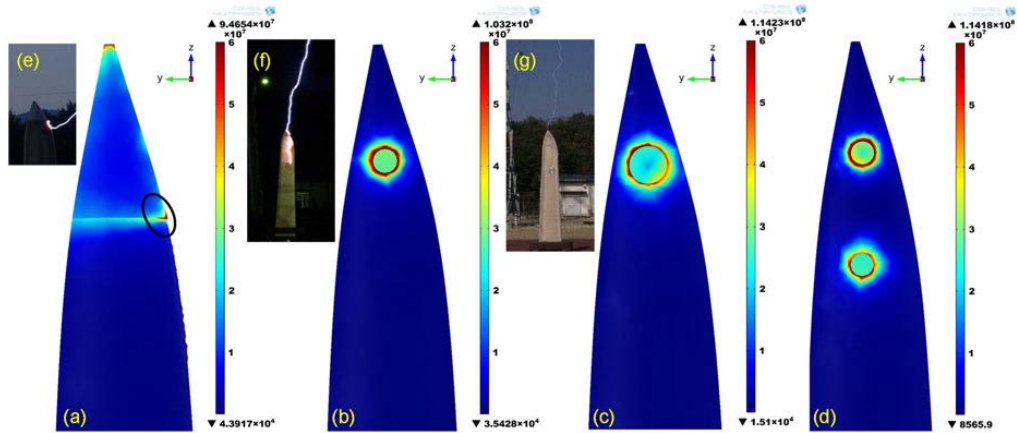
*Figure 23 - Contour plots of Electric Field around receptor systems
(Wang et. al., 2017))*

The study showed that among the receptors being considered, the disc shaped receptor exhibited maximum electric field, in which the larger receptor system showed the highest magnitude. According to this simulation, the blade with larger receptor is prone to be a better lightning receptor. The author further acknowledges that the results are dependent upon lightning leader model and meshing parameters used. One of the suggestions from this author as a continuation of this research is to optimize the receptor shapes, sizes and patterns to explore new options for effective lightning interception (Wang, et. al., 2017). This research and the suggestions provided forms some of the basis of our current study.

One of the limitations of previous research regarding electric field on blade composites is that they consider only the domain close to point of lightning attachment. Wang's model in contrast, represents the lightning leader from the cloud surface to the ground (spanning 4 km in length), and as such is more accurate, as it includes the effect of electric field in the upper parts of the lightning leader as well as the non-uniform charge distribution within the leader. Not taking into account the upper domain parts could result in generating a lower electric field from FEM simulations.

Validating with experimental data, the author shows that this model (and the subsequent assumptions taken) sufficiently represent actual physics of lightning acting on the turbine blade.

As mentioned, to experimentally test the effect of receptor size and shape on lightning attachment, researchers conducted high voltage impulse tests on a 3m blade tips with different receptors (Arinaga. et. al., 2006). Results from this study was used for qualitative validation of Comsol models developed by (Wang, 2016) in his research. Blades with single round receptors (both small and large), a tip shaped receptor, and one without any receptor were made and tested.

`

A 12 MV potential was applied across an electrode kept 3 – 4 m from the blade tip. One of the results from the experiment shows that even in the presence of a round receptor, the lightning leader does not necessarily attach to the receptor directly as shown in *Figure 24*.

Figure 24 - Left: Small; Center: Tip-shaped; Right: Large
(Arinaga et. al., 2006)

It can be observed that the leader enters the blade tip and travels towards the receptor through the blade, potentially causing damage along the way. Even though the receptor is successful in arresting lightning, the path followed by the high current to reach the receptor is not ideal. An important observation as stated by the author is that when the disk shaped receptor is used, the lightning leader was found to enter the blade through the tip connected to an internal down-conductor. This result shows that round receptor discs are not ideal for effective lightning protection.

When the tip is completely covered with a copper layer, lightning current in most cases attach on the conducting surface, propagating the current without any damage to the structure. However, a concentration of electric field is observed at the edges between conductive and non-conductive material. It was observed that at times, the lightning strike attaches on these edges, causing severe damage including fire on the composite surface. This agrees with the Comsol simulation results from Wang's model to show that a covered

`

tip receptor might not be the most favorable solution for lightning protection, even though it has a high protection efficiency (Yokoyama et. al., 2013).

2.3 High voltage testing

High voltage tests are conducted on wind turbines to determine receptor characteristics such as optimal location, and path of material breakdown. Studying if lightning goes through the blade surface in the presence of a receptor is also one of the outcomes of a high voltage test. Currents passing through the material during these tests are not of importance, since in real lightning, the current involved is significantly higher, causing much more material damage. High current tests are performed specifically to observe the material damage. Effects of high voltage testing are commonly investigated using high speed cameras and imaging systems.

Figure 25 shows the test setup used by a large scale high voltage laboratory to run lightning attachment tests on industry scale blade tips.
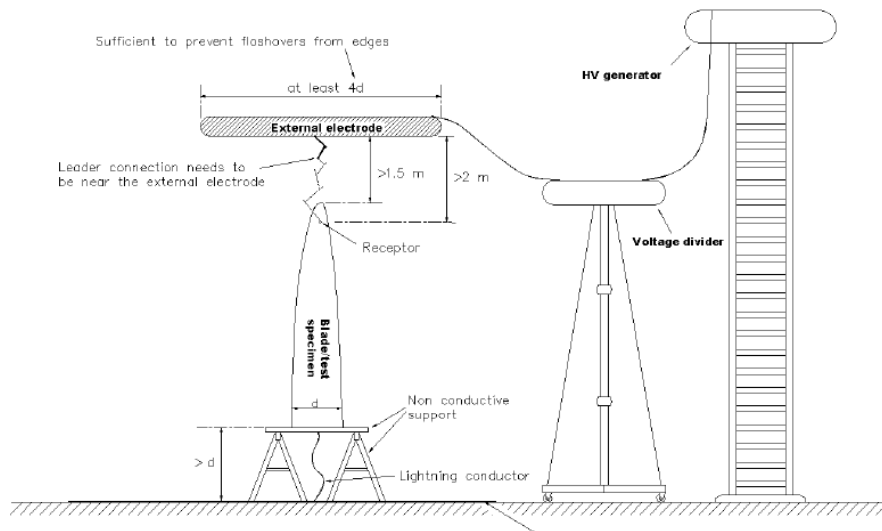
Figure 25 - Leader attachment test setup (Sorensen et. al., 2008)

The HV generator induces a very high potential across an electrode kept in close proximity to the blade receptor. At a high enough voltage difference, ionization of air will occur with a subsequent lightning leader emitting from the electrode. This is one of the setups commonly used in conducting a high-voltage lightning attachment analysis (Sorensen et. al., 2008). According to the author, the ideal attachment test setup to evaluate new LPS designs and local protection regions is shown in *Figure 26*. This setup is used for an initial study of LPS design, and should be followed with more reliable test setups as shown in *Figure 25*.

32

SECTION A-A view
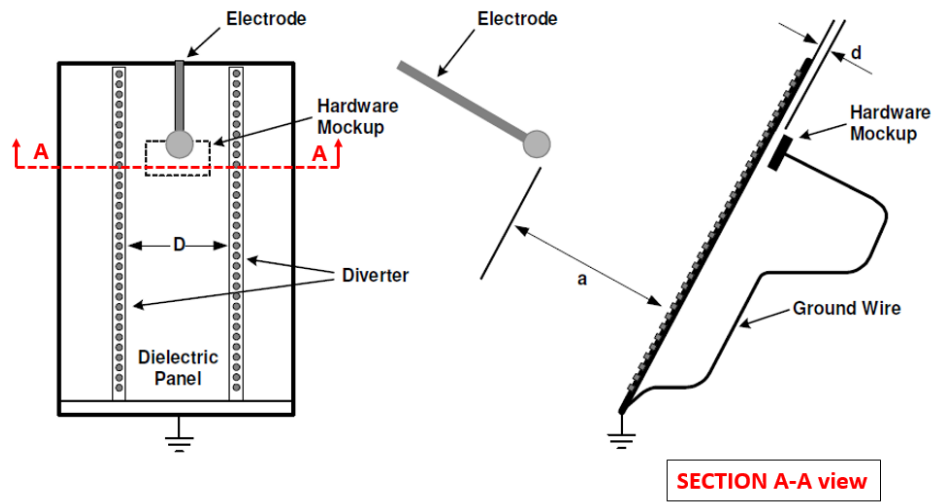
Figure 26 - Test setup for initial high voltage experiments
(Modified from Sorensen et. al., 2008)

Figure 26 illustrates the parts involved in Test Setup for high voltage testing of a lightning diverter. A similar setup to what is shown in ***Figure 26*** is planned for the current research, using a pin type electrode to discharge lightning leaders towards a grounded surface representing the blade with conducting patterns as receptors.

(a) Lightning impulse

(b) Switching impulse
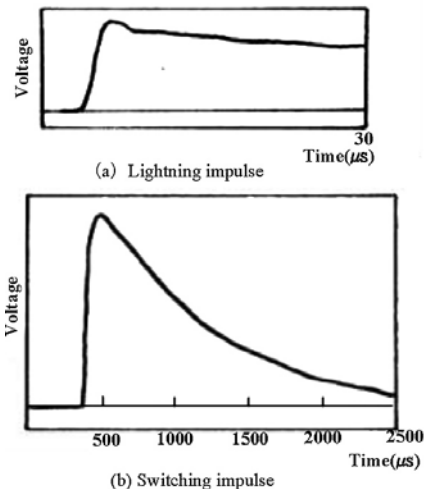
Figure 27 - Lightning impulse and switching impulse waveforms generated
from HV generator (Yokoyoma et. al., 2013)

High voltage testing of Lightning protections systems or materials are done normally at specific facilities designed for such tests. The Shiobara testing yard is part of

33

the Central Research Institute of Electrical Power Industry, and is a high voltage test facility that is used for turbine systems (Yokoyama et. al., 2013). This facility is capable of producing up to 12 MV of peak impulse voltage (*Figure 27*).

A study was done to observe the effects of surface impurities on lightning attachments on a blade without receptors. Pollutants were added to the pure blade by treatment with salt water and clay. A high voltage test was performed for blades treated with different amounts of impurities. For the purpose of the current research, the method of high voltage testing and data collection they have used are what is relevant and not necessarily the results obtained from this experiment.

Table 1 - Number of high voltage discharges to polluted and non-polluted blades (Yokoyoma et. al., 2013)

	Discharge Manner	**Number of Times**
Un-Polluted	Electrode-to-ground	28
	Creeping	8
Pollute	Discharge Manner	14

Table 1 shows one of the results, where the number of high voltage strikes were counted for the polluted and non-polluted blades and compared with the distance between electrode and blade tip set at 4 meters. In this study, the number of strikes going directly to ground have also been observed. The term creeping refers to surface flashovers occurring on the blade surface, where the current travels on the non-conducting surface towards the ground or the receptor.

The experiments were performed for the same blade using impulse voltage waveforms for both positive and negative voltage sources. It was found that positive discharges caused more damage than negative, because the positive answering leader emitted from the ground structure when a negative potential is applied across the electrode is much easier to occur than emission of a negative answering leader. It can be inferred from this study, that observing the number of strikes occurring on a blade and subsequent lightning protection components is an accepted method of data collection for high voltage testing.

Much lower peak voltages are also used for similar high voltage tests. A study was done on conductive layers, concentrating on the percentage doping of conductive elements for the coating, and its effects on effective lightning mitigation. As opposed to 12 MV considered for the Yokoyama's research, the voltage considered for this study (Lewke et. al., 2007) was in the range of 120 kV to 1 MV. Breakdown of the conductive layers was found to occur from a voltage of 300 kV up to 700 V depending upon the layer thickness and doping percentage, as shown in *Figure 28*. The high voltage electrode in this case was kept 175 cm from the ground surface. The Figure shows breakdown voltages of surface

`

layers of different thicknesses doped with different percentage levels of conductive additives.

It can be seen that even at a voltage as low as 300 kV, breakdown of material is possible, and therefore material breakdown can be considered to be dependent on material properties and thickness. However, for the current study, only lightning attachment is observed, and not the effects that occur after attachment. Further details regarding the study like material composition and other parameters such parameters are irrelevant to the current study, and as such are not discussed.
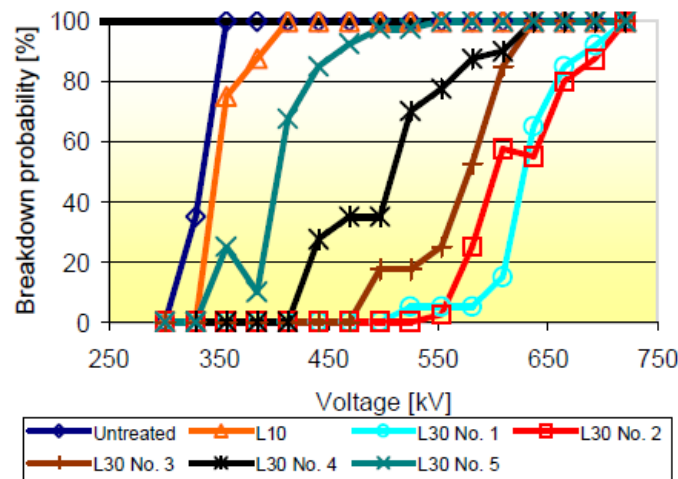
Figure 28 - Breakdown of conductive layers with different doping percentage and layer thickness (Lewke et. al., 2007)

Many of these high voltage test facilities make use of a Marx generator to generate the high voltage outputs. The generator makes use of a relatively low voltage source and acts as a charge storage unit, converting the low voltage input into high voltage by accumulation of charge. Marx generators in full scale laboratory setups are generally large devices however, smaller Marx generators are also made, and often act as triggers for the larger generators.

The Marx generator stores electric energy within a set of capacitors and discharges it in a very short time as a comparatively high voltage output to the initial input voltage. A Marx generator consists of a set of resistors and capacitors connected as show in *Figure 29*. Resistors in this circuit charges the capacitors using a low input voltage.

When the voltage across each stage switch reaches a particular threshold, a spark is formed across the stage switch, shorting it and thereby causing an increase of voltage across the rest of the switches. This repeats across all the rest of the switches one after the other, ultimately forming a different circuit (due to shoring of the switch gaps) during voltage

discharge, as shown in **Figure 30**. This is the discharging circuit diagram of a Marx generator when all the stage switches are shorted due to voltage buildup.
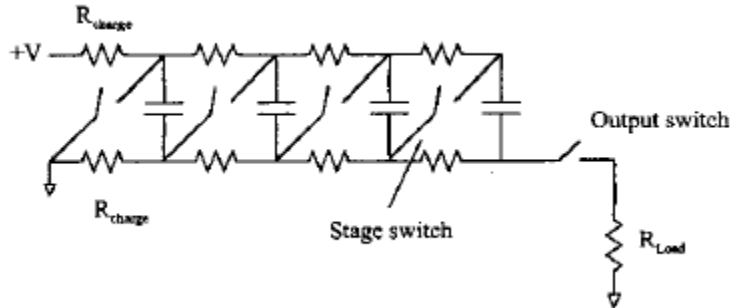
Figure 29 - Marx Generator circuit during charging stage
(Carey et. al., 2002))
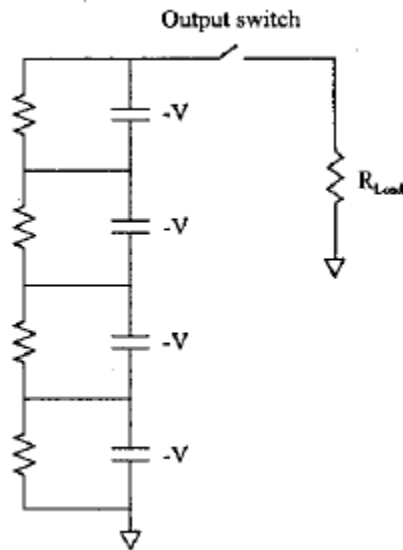
Figure 30 - Marx Generator circuit during discharging stage
(Carey et. al., 2002)

This temporary change in the circuit discharge a high voltage as output. The magnitude of the voltage depends on the number of stages (Resistor – capacitor – switch arrangement) present in the Marx generator. For an input voltage of V, and N number of stages, the theoretical output from the Marx generator should be V·N (Carey et. al., 2002).

As mentioned earlier, there are various scales of Marx generators being built – ranging from large scale to Compact. The compact generators produce peak currents from

100 kV to 1 MV for high voltage testing. Construction of a compact Marx generator is planned to carry out high voltage tests for our current research.

2.4 Novel Lightning Protection methods

There is a lack of research currently, in exploring new shapes and patterns for incorporation into Lightning Protection Systems. There is much research and that shows that electric field surrounding a conductive (or grounded) structure depends on the size, shape and number of receptors included in the design. However, very less research has been published in exploring new shapes and conductive patterns on the blade surface as a new form of Lightning protection.

Conductive layers are being developed as LPS systems; however, covering the entire blade surface with a conductive coating will either significantly increase the blade weight (in case of metal components) or increase the blade cost.

An innovative lightning protection sheet has been recently developed and patented that uses patterns of conductive layers in an extruded thickness to provide lightning protection to space vehicles (Hebert et al., 2014). A significant highlight that is developed in this design is the inclusion of "hill features", where the height of the conductive pattern is considerably higher than the thickness in some areas. Although a continuously conductive layer is being used in this study, the presence of hill features makes a significant difference in design compared to other LPS systems being used.

The shape of the lighting receptors affects their efficiency in attracting lightning. An interesting observation from high current test research on blades is that charges of 300 Coulombs can rupture the blade with receptors due to internal over-pressure effects; however, charges of 1000 C have been seen to be resisted by large round lightning receptors (Hebert et al., 2014), showing that shape and size of the receptor has a significant role in increasing probability of lightning strike attachment.

In addition, due to rotation and/or the effect of wind on the lightning attachment, the point of contact shifts from the initial point, possibly to one of the insulating surfaces, causing composite surface damage (Yokoyama et al., 2014). A recent study of 304 wind turbines subject to lightning strike damage suggests that lightning protection effectiveness has less to do with number or configuration of systems in place, but relates to how well the conductive members are insulated and the lightning is transported within the blade (Garolera et al., 2016).

The proposed LPS design can potentially alleviate some of these issues, since there is increased lightning protection coverage, and the point of attachment will follow a conductive path on the coating, preserving the composite surface around it. However, increased attention in future studies has to be given to the adhesive used, to make sure it does not lose its insulating and adhesive properties during the influence of high current/voltage.

CHAPTER 3 . NUMERICAL MODELING OF ELECTRIC FIELD ON TURBINE BLADES

Many of the previous research done to study electric field around turbine blades made use of much simplified geometries to represent the turbine structures for ease of FEM modelling. In addition, only the domain in the vicinity of the blade surfaces were taken into consideration. (Wang, 2017), in his research, made use of an intricate turbine geometry, using actual turbine dimensions published by NREL for its 5 MW turbine design, to perform an electric field analysis in FEM. In addition, a much larger domain was considered, which extended from the ground surface to the cloud surface, consisting of a 4x4x4 km^3 domain.

This model was considered a suitable reference to create accurate models for the current study. One of the objective of the current research is to generate new pattern designs which would potentially offer higher electric field (and correspondingly better lightning protection). Therefore, an existing model which studied electric field around standard receptors was chosen, and recreated – such that validation can be thoroughly done, and the resulting new patterns can be assumed to have fairly accurate results.

3.1 3D Turbine model creation

A 3D model of the wind turbine was made according to specifications published by NREL (Jonkman et. al., 2009) and taking reference of a previous project done with the same turbine model. Reference models of the turbine were obtained from (Wang, 2017) for use in current study. *Figure 31* shows the blade, tower and complete assembly used for recreating the turbine using CAD (Computer Aided Drawing). The reference models were originally created using PRO-E, and for ease of performing surface operations, it was imported into CATIA V5 R20, where the final models were generated for performing the current study.

Even though an accurate model of the NREL 5 MW turbine was available, it was recreated using dimensions from the reference and the NREL publication. This was due to incompatibility issues when importing the available CAD model into COMSOL Multiphysics software used to perform the FEM analysis. *Figure 32* shows a few examples of such geometry issues, which caused problems while importing the geometry, or during meshing of the model.

When importing CAD models into Comsol, there is a certain level of geometry optimization that occurs, and as such, the model is automatically simplified by omitting lines or surfaces. Also, meshing within Comsol is automated to a certain extent. Any unnecessary points or lines on the CAD geometry will sometimes be taken as a point of concentration for meshing, and as such, finer mesh sizes will be used on such areas, or in some cases, meshing will not be possible. Such cases should be avoided when designing the CAD model for analysis, and so, the reference models were "cleaned" by recreating it

using the "CATIA V5 Generative Shape design" module to perform most of the surface manipulations.
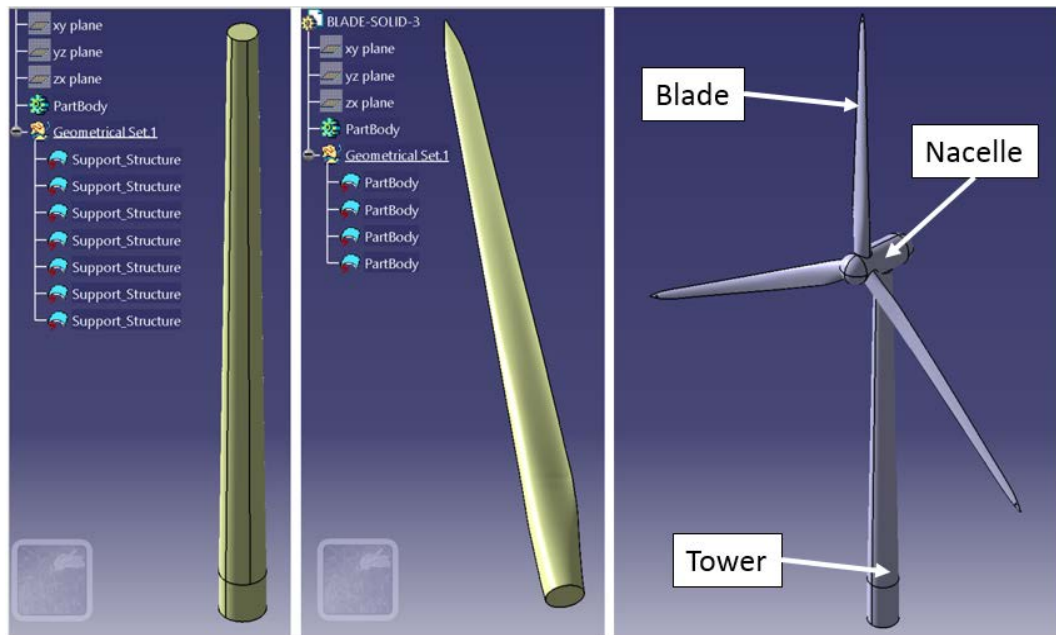
Figure 31 - Reference models of NREL 5MW turbine tower (Left), blade (center), and complete assembly (Right) imported in CATIA V5 R20)
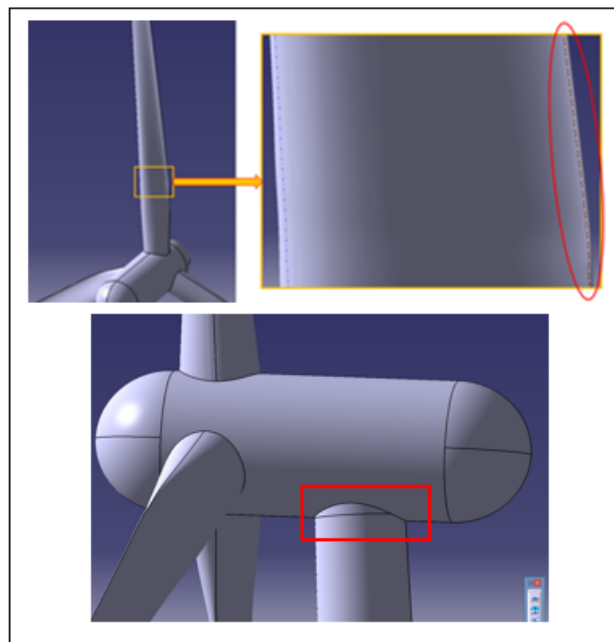
Figure 32 - Geometry issues in reference model; (a) Top – Blade edge geometry (b) Bottom – Turbine tower geometry

`

The blade geometry was recreated from the reference model. As seen in *Figure 32*(a), the trailing edge in the reference model CAD geometry does not fall precisely on the edge of the blade, and as such, while importing into COMSOL, the software had difficulties simplifying the geometry, and as such, the resulting geometry was found to have surfaces which intersected each other, producing the corresponding errors. Therefore, remodeling of the turbine components was necessary to get rid of redundant edges and to sufficiently "clean" the blade geometry for import into COMSOL.

The turbine tower was created using data published by NREL regarding tower dimensions (Jonkman et. al., 2009). A multi-section solid was created using 22 sections as shown in *Figure 33*. Comparing the structure obtained from this operation to the reference tower model shown in *Figure 31*, we can observe that few unnecessary edges have been removed, while keeping the geometry same. The completed tower model was super-imposed on the reference model and verified for accuracy in geometry. The two models were found to be identical in shape.
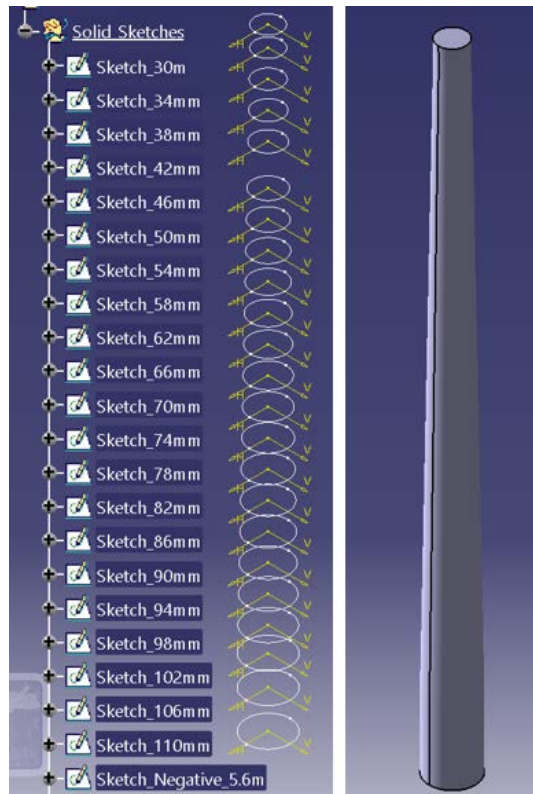
Figure 33 - Multi-section turbine tower model using 22 sections

A similar approach was taken to model the blade surfaces. However, since a reference blade model was already available, it was used instead of NREL data for ease of modelling. Cross-sections of the reference blade were taken at intervals of 1 m from the blade root (*Figure 34*). It was found that some of these cross-sections had self-intersecting

`

edges, and such edges would cause errors during conversion of the different sections into a single geometry by creating a multi cross-sectional solid. Self-intersecting cross-sections were ignored, and all the remaining blade cross-sections were cleaned to have end points exactly at the tip of the trailing edge. This was done to eliminate the geometry issue mentioned in *Figure 32*(a).

Two distinct multi-section surfaces (One for upper layer, and one for lower layer) were created from the cleaned cross-sections and later converted into Solid, using surface options available in CATIA.

Once the blade and support structure were modelled, a complete turbine assembly was generated as shown in *Figure 34*. The turbine specifications (Jonkman et. al., 2009) mentions that there is a 5° tilt of the nacelle with respect to vertical plane, and as such, an axis was created along the center line of the nacelle, and the 3 turbine blades are patterned around this axis to get the correct geometry. The final turbine assembly is also loaded along with reference geometry for verification. As in the case of the tower structure, it is observed that the geometries of the current model and reference models are the same. Therefore, a simplified and cleaner CAD model is created for use in FEM analysis.
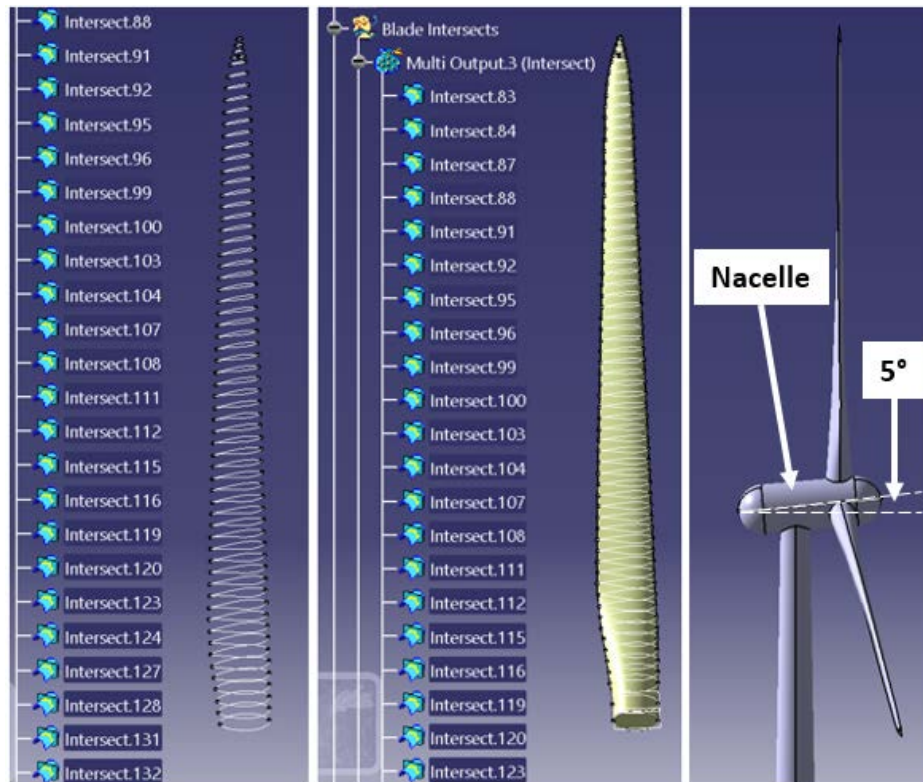
Figure 34 - Left: Reference blade cross-sections at intervals of 1 m
Center: Multi-section surface using cleaned cross-sections
Right: Complete NREL 5 MW turbine assembly

41

`
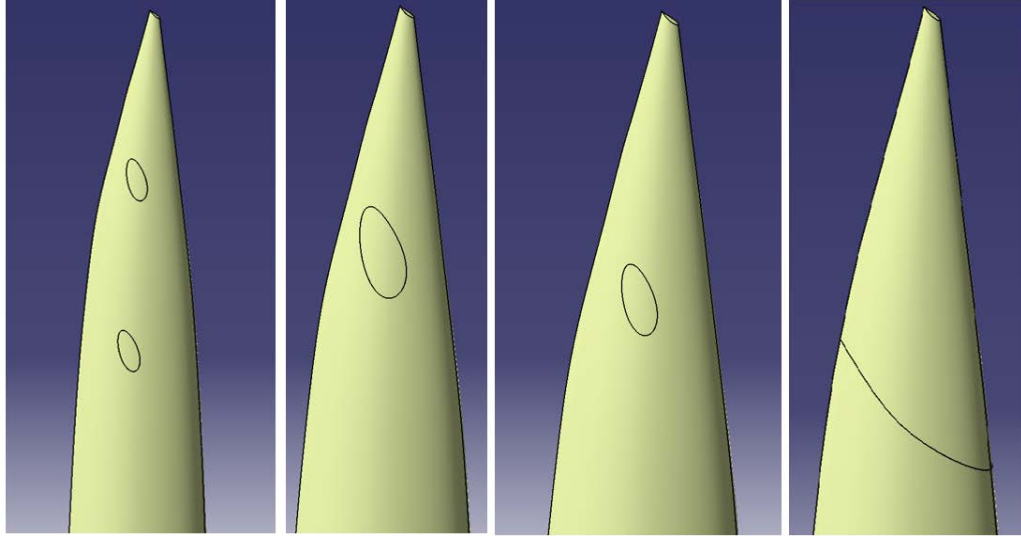
***Figure 35 - Four types of receptors modelled on NREL 5MW Turbine for FEM
validation study (IGES files)***

The final models were saved as IGES files, due to ease of handling and post-processing. As IGES files get saved using just the outer surfaces of the solid models created, it can be further modified and simplified using surface operations. The NREL 5 MW turbine model was used to study the effect of different receptor types and sizes on electric field due to lightning (Wang et. al., 2016). As mentioned in Chapter 2, the researchers studied electric field around 4 different receptors on the same blade. In order to validate the current model, the same receptors were modelled on the turbine to recreate the study done by (Wang, 2017). ***Figure 35*** shows the blade tips of different receptor systems modelled on the turbine blade for conducting model validation.

3.2 Comsol Multiphysics FEM analysis

Comsol Multiphysics V4.2b was used to conduct FEM analysis for electric field calculations in this study. The Electrostatics module was used to conduct a steady state analysis and the turbine models were imported using an absolute import tolerance of 1.0E-05. A 4x4x4 km cube was created, keeping the turbine standing in the center of the bottom face of the cube. The top face of the cube acts as the charge carrying cloud surface, and the bottom face represents ground. A cylindrical lightning leader of 1.5 m radius is modelled, which starts from the cloud surface, and extends up to the height of the turbine from the ground. The turbine model is 151.5 m tall, and the corresponding length of the lightning leader is 3848.5 m (4000 – 151.5 m).

The above mentioned model features were also used in previous research done by (Wang, 2016). In addition to these features, the current model required the addition of a cylindrical domain immediately surrounding the turbine geometry (***Figure 38***) for error-free meshing. The smallest edge length in the turbine geometry is close to 0.5 m, and the

`

largest edge length is 4000m. This drastic difference in the scale of geometries used, and the intricate geometry of the turbine surface requires the use of multi-scale meshing operations.
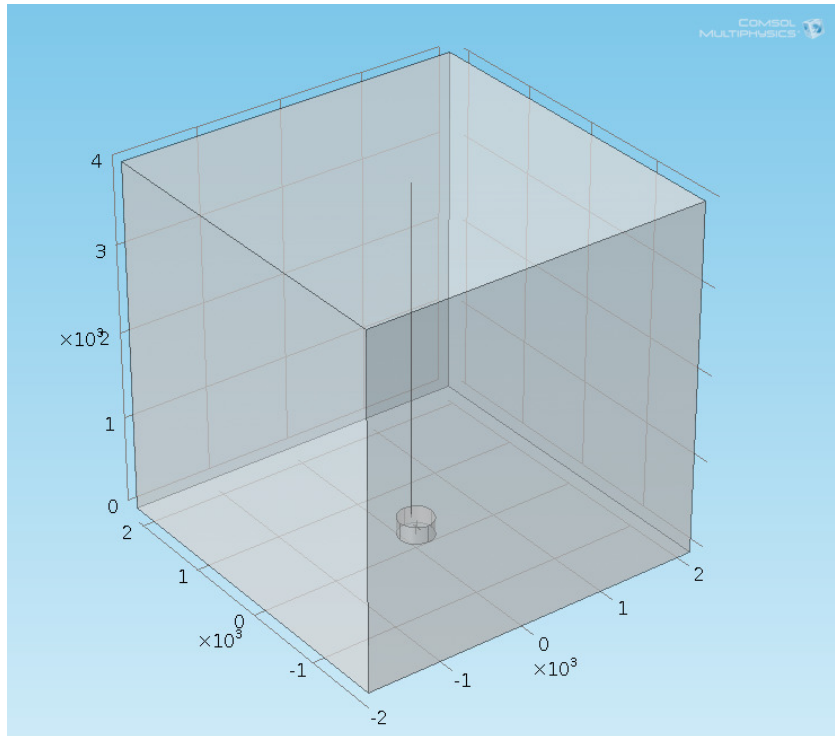
Figure 36 - Comsol model for FEM analysis of Electric Field (Current model)

The reference model was created using an earlier version of Comsol (V4.1), which allowed the use of a single mesh settings for the entire 4x4x4 km domain, including the turbine surface features. This was probably possible due to approximations of geometry and mesh done by Comsol, which also affected the results of the simulation. This will be discussed in detail in section 3.3.

The recent versions of Comsol (4.3b and above) however, does not accept such multi-scale geometries without additional operations to simplify meshing. As such, the addition cylindrical domain was included around the turbine, to assign different mesh parameters in different domains, to facilitate finer meshes closer to the turbine surface, and coarser mesh elements for other parts of the large domain.

A free tetrahedral mesh was used throughout all the domains for high accuracy. However, as mentioned, domains were created and meshed separately in order to facilitate meshing of geometries with a large difference in dimension. In accordance with Wang's models, a turbine cutout is used for ease of assigning ground boundary conditions without specifying turbine material. The model consists of 3 domains – 1) a cylinder with

`

the turbine cutout, 2) a cylindrical lightning leader, and 3) the surrounding domain of the 4x4x4 cube. The mesh parameters used for all 3 domains are shown in **Table 2**.
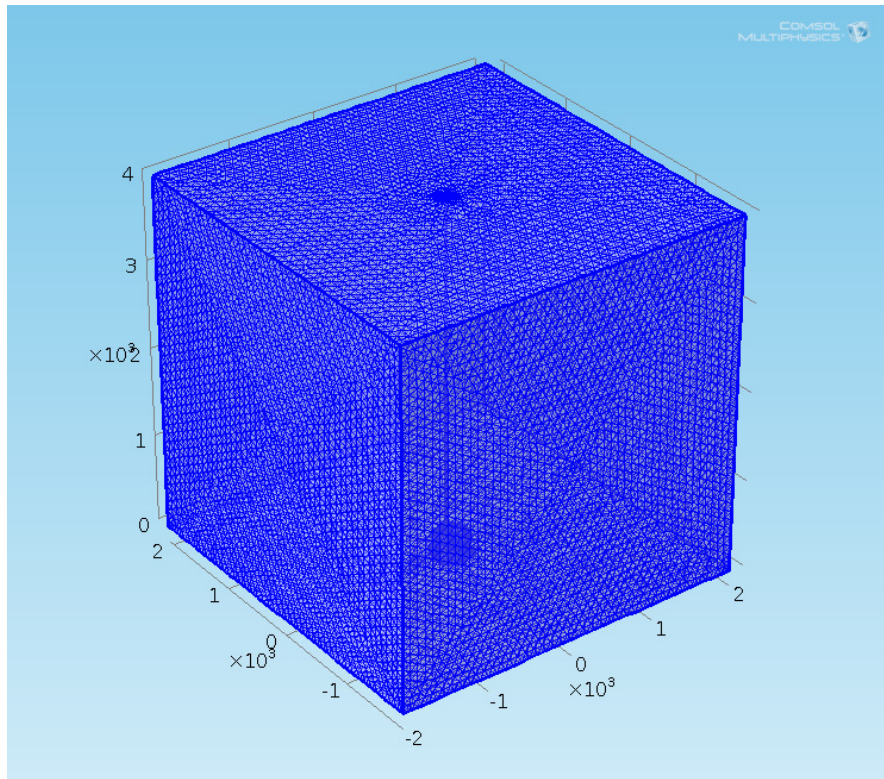
Figure 37 - Multi-scale mesh of 4x4x4 km³ domain

Table 2 - Mesh settings used for different domains in current Comsol model

Mesh Parameters	Domain 1	Domain 2	Domain 3
Max. Element Size (m)	10	50	100
Min. Element Size (m)	0.1	0.1	0.1
Max. Element growth rate	1.5	1.5	1.5
Resolution of curvature	0.5	0.5	0.5
Resolution of narrow edges	0.4	0.4	0.4

Figure 38 shows the inner cylindrical domain containing the turbine cutout. It can be seen how the mesh gets refined close to the turbine and lightning leader surfaces. This

44

`

feature of the model helps to provide accurate results in areas of importance (those close to the turbine surface), while reducing computation time by increasing mesh element size in areas, which are not vital for the study.
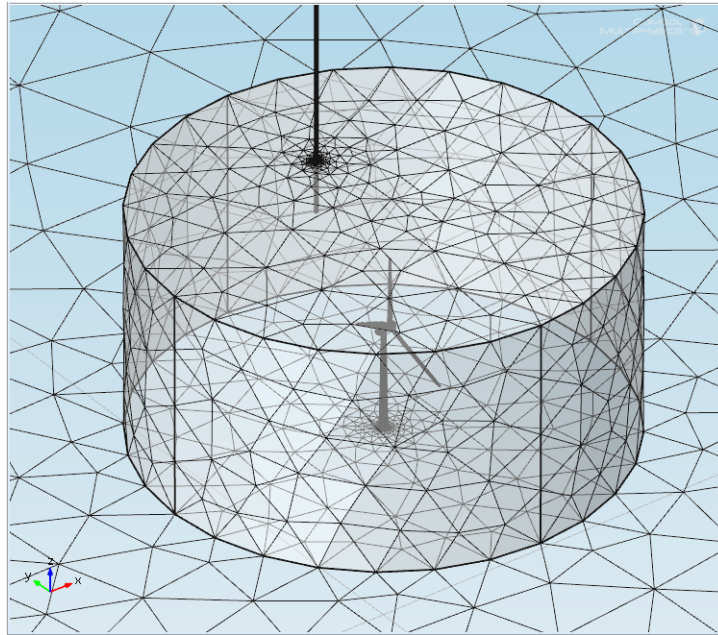
Figure 38 - Cylinder containing Turbine cutout
(Part of lightning leader is also seen)

While maximum and minimum element size mesh parameters are self-explanatory, the maximum element growth defines how the mesh elements grow in size. For example, a value of 2 says that the mesh elements can grow in size by up to twice its size for two adjacent elements. A higher value of curvature resolution generates a finer mesh for elements on a curved geometry, and similarly, a higher value for "Resolution of narrow edges" generates a finer mesh in narrow regions in the Comsol geometry.

Due to finer mesh parameters used to generate the innermost cylindrical domain, the mesh elements close to the turbine surface are extremely fine as shown in **Figure 39**. The meshes created for current study is much finer compared to the reference model, and as such, higher accuracy is expected for results obtained from current analysis.

A potential of 4E+06 V was assigned to the top face of the cube domain shown in **Figure 37**, and ground condition was applied to the turbine tower, nacelle, and receptor surfaces. The surrounding blade surfaces were assigned with the default open boundary condition, to simulate the effect of a non-conducting composite surface, as done in the reference models.

`
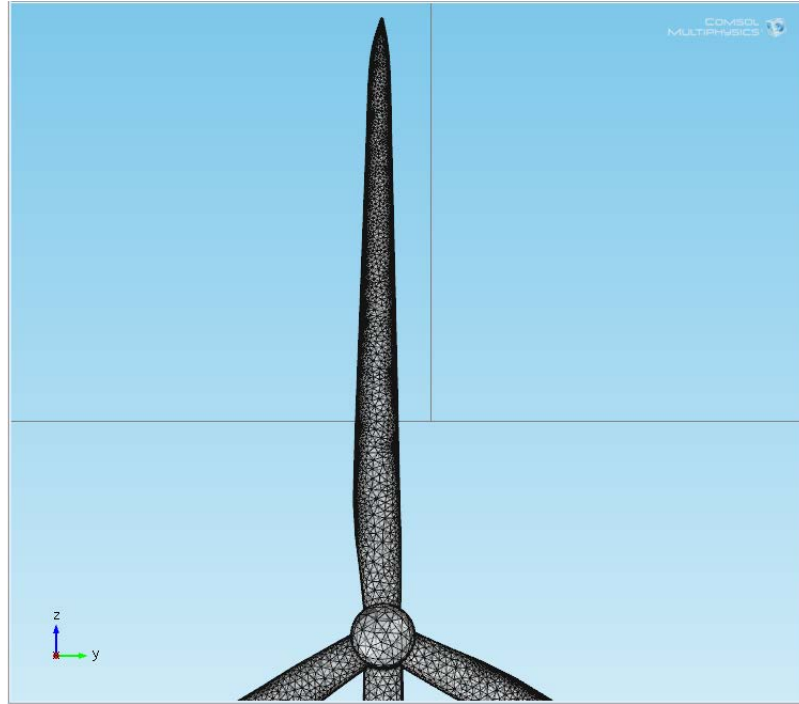
Figure 39 - Fine mesh on turbine cutout surface for high accuracy

As mentioned in Chapter 2, one of the major inclusions in (Wang's, 2016) research was the addition of non-uniform charge distribution within the lightning leader to simulate Cooray's model (Cooray et. al., 2007). The parameters required for the relation between charge density $\rho(\xi)$ and peak current as shown in *Eq. (2)* was created in Comsol, and the corresponding charge source ρ_v (from *Eq. (10)*) was assigned as the volumetric space charge density of the lightning leader. Charge density was assigned as a parametrized relation because of its dependence with height from ground (for a non-uniform charge distribution).

In-built material properties for air were assigned to all domains of the model. Since the turbine cutout contained only outer surfaces, material properties were not required here. The solid domains surrounding the turbine surfaces including the lightning leader were assigned with the properties of air, as provided within the Comsol software.

3.3 Model Validation

Particular emphasis was given to the model accuracy, and as such, considerable attention was given to the model validation study. A detailed study was done to compare highest electric field values, and graphs of electric field along trailing and leading edges with those of reference models. In addition, the most probable cause of difference in values between the models is also suggested.

46

`

To validate physics used, and the correct use of Cooray's model to simulate electric field around the lightning leader using parametrized analysis in Comsol, another study done by the same author (Wang, 2016) was referenced. A turbine 250 m tall was modelled using the same geometry features as explained in section 3.1 for a peak current of 200 kA. The corresponding lightning leader used was of length 3,750 m and the leader cross-section was assumed to be 5 m in radius. The rest of the parameters were the same as those used for the current study. The model used 4455950 number of mesh domain elements and the analysis took 24 minutes including meshing for each analysis run, when done on a 24 GB RAM 3.20 GHz workstation with a 6 GB graphics card.

Figure 40 shows a comparison between the electric field results obtained from reference model to that of the current model, made for validation of physics used. The shape of electric field distribution around lightning leader is observed to be almost identical among the two models. The contour plots closely match, and the difference in peak electric field between the reference model and current model is only 12%. Inclusion of non-uniform charge distribution causes a concentration of electric field around the leader when it gets close to the ground, as can be observed from *Figure 40*. For a uniform charge distribution, the electric field distribution would be same at all heights of the leader, which is not the case in reality.
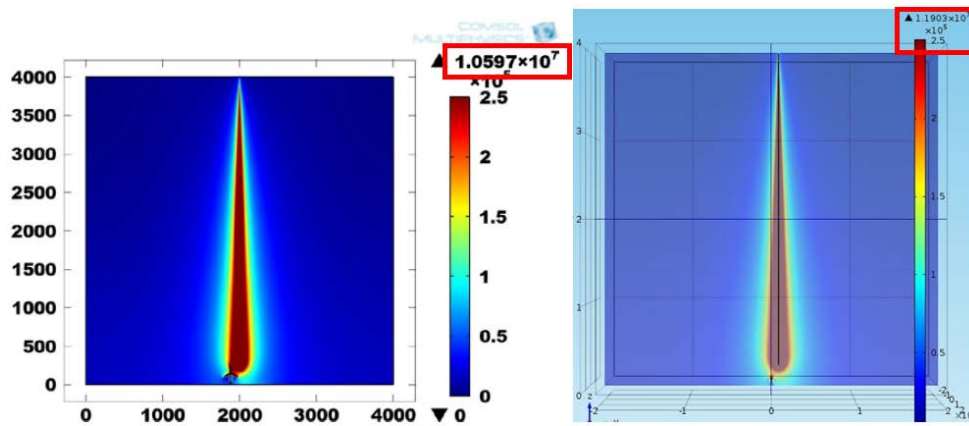
Figure 40 - Electric Field around lightning leader in:
Left - Reference model (Wang et. al., 2016);
Right - Current model for physics validation

After successful validation of lightning leader physics, the same was incorporated into models of different receptors on the 150 m long NREL 5MW blade, for validating the current model with results from Wang's later studies (Wang et. al., 2017).

`
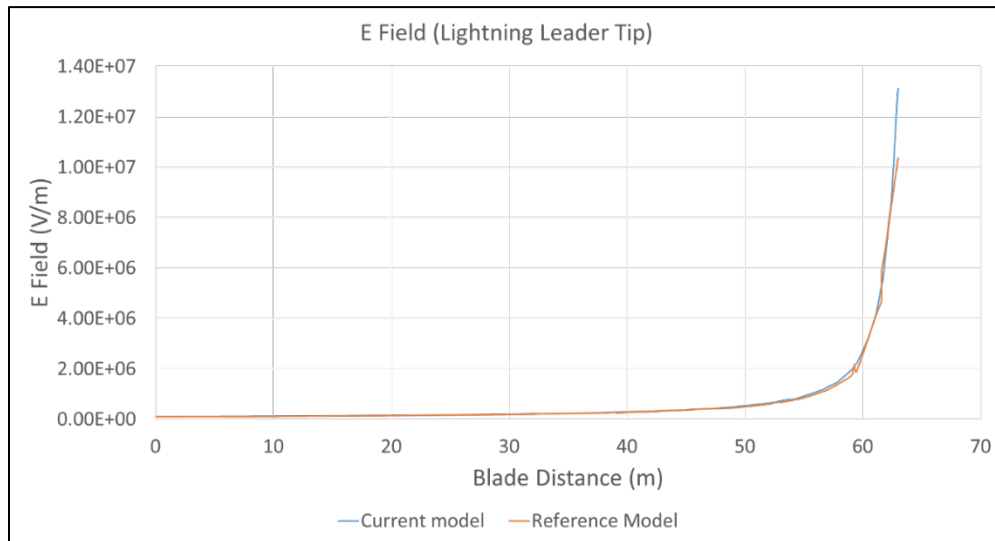
Figure 41 - Validation of Electric Field along lightning leader length
(Wang et. al., 2017)

Figure 41 shows the comparison of electric field along the lightning leader length between the current and reference models. It can be seen that the results closely match values obtained from the reference model. The variation in peak electric field is expected to be due to different meshing parameters used in the current model. Since a finer mesh is used and there is no other change in boundary conditions, physics or geometry, the results should theoretically be more accurate than the reference models.

3.3.1 Round receptor of 0.3 m radius

Three parameters were used for validation of all models with reference data – 1) Surface contour plot of electric field on blade, including receptor 2) Electric field along Leading edge and 3) Electric field along Trailing edge.

Figure 42 shows the comparison of contour plots for electric field around a round receptor with a diameter of 0.3 m. The plot on the left indicates results from the reference model, and plot on the right shows results from current model. The contour plots show close similarities between the two models, and difference in peak electric field is found to be 7.9%.

The corresponding comparison of electric field along the trailing and leading edges are shown in ***Figure 43*** and ***Figure 44*** respectively. As in the case of peak electric field, values obtained from the leading and trailing edge closely resembles those obtained from the reference model. As expected, the electric field is comparatively low from the blade root to around 55 m in length, after which there is a peak in electric field intensity, caused due to the presence of the receptor.

`
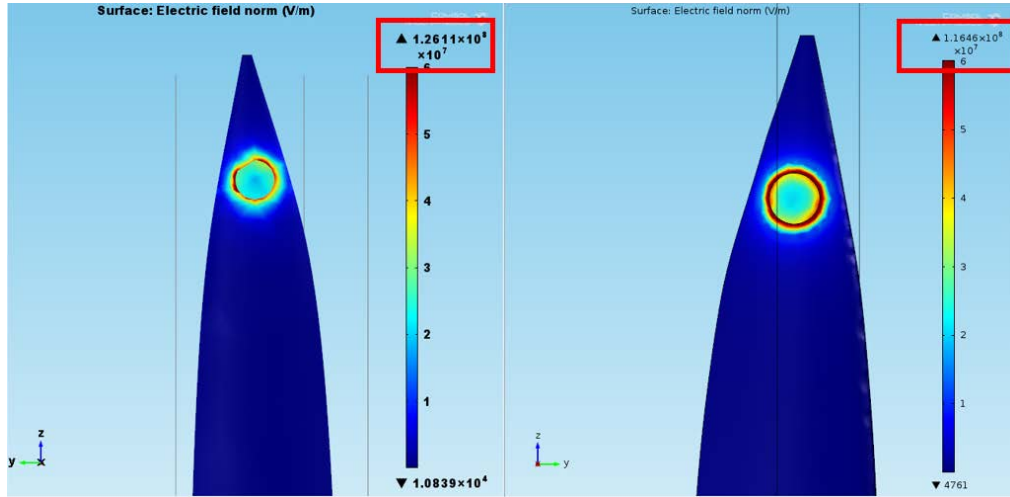
***Figure 42 - Comparison of peak Electric field in: Left - Reference model
(Wang et. al, 2017); Right - Current model (0.3 m round receptor)***
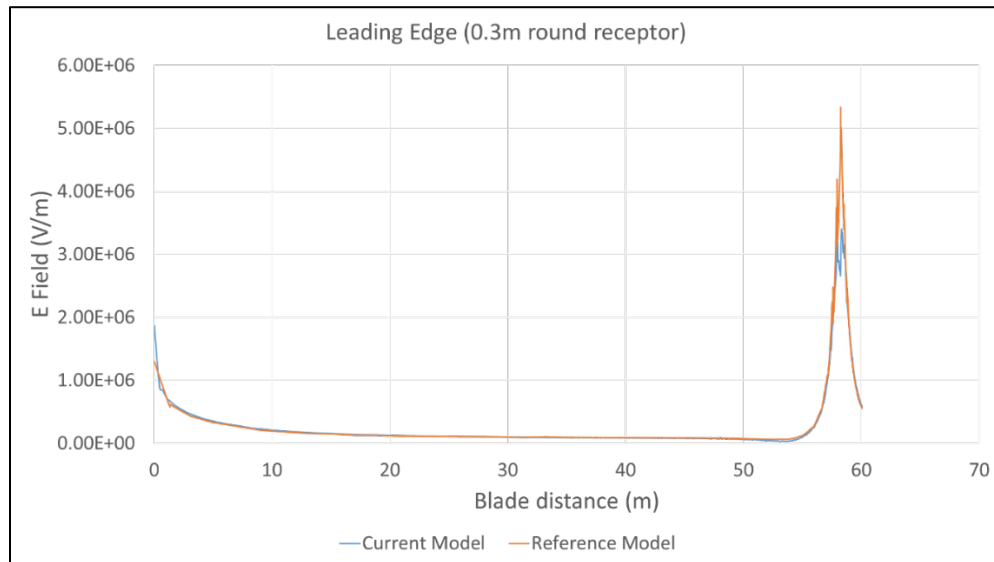
***Figure 43 - Comparison of electric field along trailing edge of reference model and
current model for blade with 0.3 m round receptor***

The peak electric field on the leading edge is found to be lower than that of reference model as shown in **Figure 44**. Any difference in these values is attributed to the different mesh parameters used and discrepancies in geometry, as electric field study is extremely sensitive to sharp edges and shapes. The mesh parameters used for the reference model is given in **Table 3**.

`

Table 3 - Mesh parameters used in reference models

Mesh Parameters	All Domains
Max. Element Size (m)	100
Min. Element Size (m)	0.5
Max. Element growth rate	1.3
Resolutions of curvature	0.5
Resolution of narrow edges	0.9

Since the blade tip is relatively narrow in dimensions, it is an area of concentrated electric field intensity. Any small differences in geometry or meshing is expected to cause a significant difference in results. However, considering the differences between the two models, we can still observe that there is very close resemblance among them, and the differences in peak electric fields are acceptable for the current study.
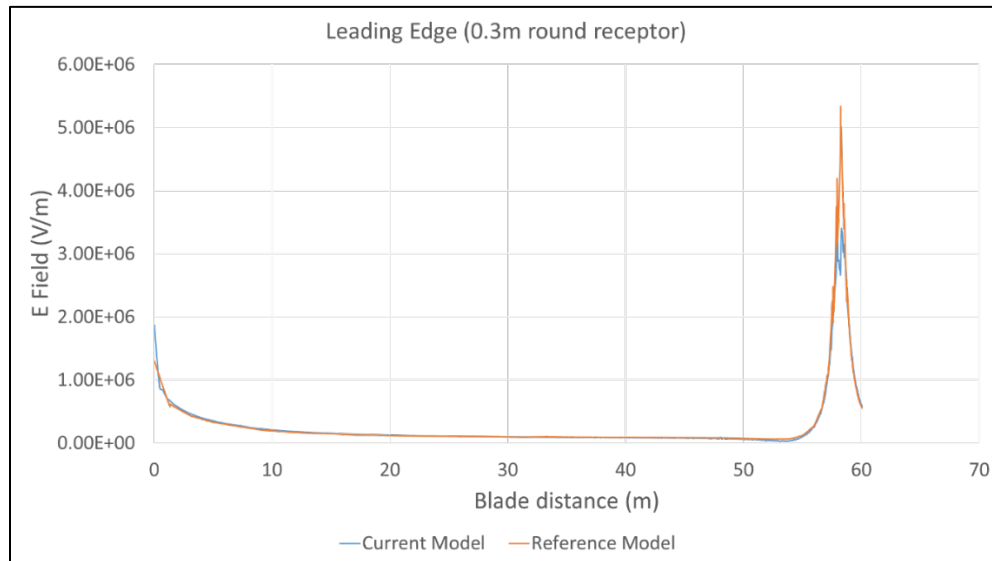
Figure 44 - Comparison of electric field along leading edge of reference model and current model for blade with 0.3 m round receptor

To verify that differences in results are due to imperfections in geometry and mesh settings, a mesh quality contour plot was studies. This is an analysis option available in Comsol, to observe mesh consistency of the model, and it also gives an idea about how accurate the corresponding results could be. As the value of mesh quality approaches 1, the

`

model is more accurate. In *Figure 45,* the difference of mesh quality between the current and reference models can be easily observed.
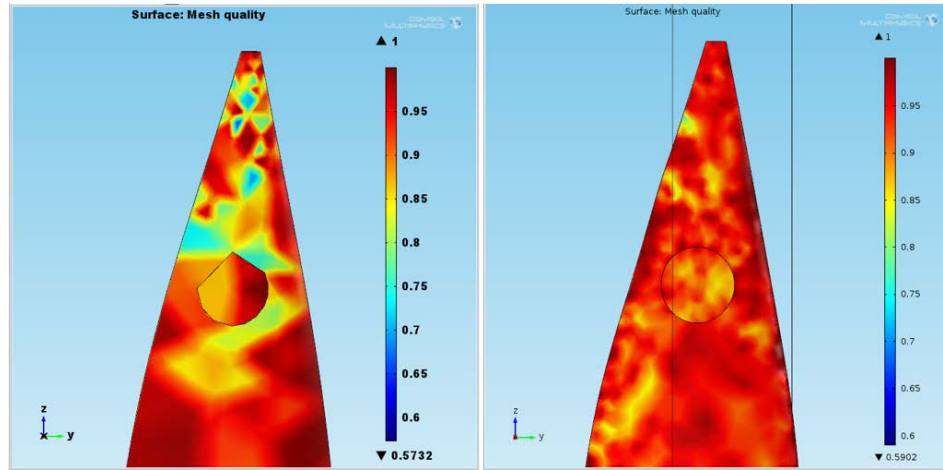
Figure 45 - Comparison of mesh quality among reference model (Left) and current model; (Right) for blade with 0.3 m round receptor

There is considerable inconsistency in the mesh used in reference model, compared to the current model. Patches of blue and light blue areas can be seen at regions, indicating mesh qualities of 0.6 to 0.75, whereas the current model has a consistent mesh quality of 0.9 and above throughout the model surface. In addition, there are geometry discrepancies on the receptors shape as can be observed in *Figure 45*. The receptor, which is intended to be rounded, is represented as a partially distorted shape during meshing, and as mentioned earlier, the shape of the surface in consideration significantly affects the results obtained, as can be observed in the next model as well.

3.3.2 Round receptor of 0.2 m radius

A similar comparison is done between the current and reference models for a turbine blade with round receptor of 0.2 m radius. In contrast with the 0.3 m receptor model, there is a difference of 51% between the peak currents of both models. This is also attributed to the distortions in geometry that was observed in the reference model. Being a smaller surface feature, the 0.2 m receptor is assumed to undergo more variations in geometry during import and thereby have more mesh discrepancies in Comsol. *Figure 46* shows a comparison between the two models. The distortions in receptor shape can be seen to affect the electric field results. This is the main reason assumed to affect the peak electric field being compared, thus the larger difference in peak values.

The corresponding electric field 1-D plots along the trailing and leading edge for the turbine blade with receptor of 0.2 m radius is shown in *Figure 47* and *Figure 48* respectively. As in the case of the previous receptor arrangement, the electric field results

`

closely follow the reference data. The peak electric field also occurs at the same distance from blade root. However, there is a difference in the peak electric field seen in these plots as well, which is attributed to the variations in geometry, as discussed.
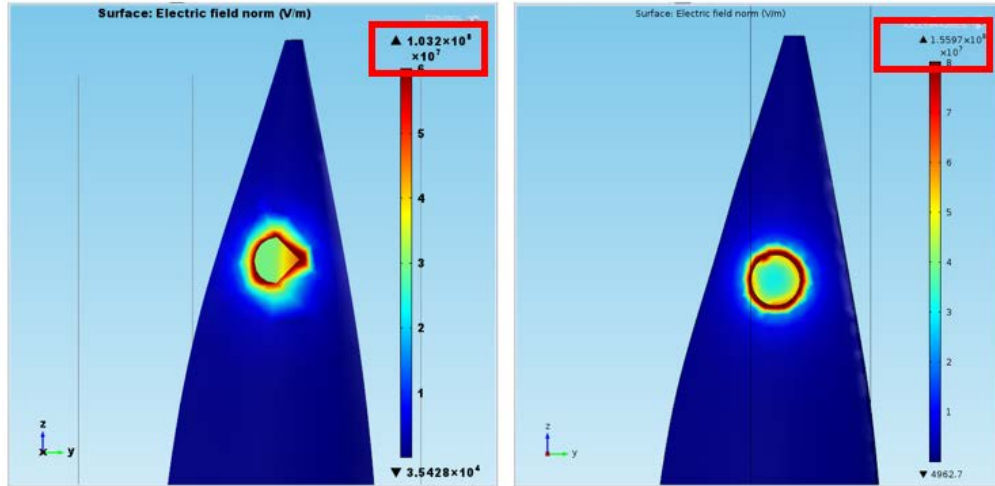
Figure 46 - Comparison of peak Electric field in:
Left - Reference model along with discrepancy in import geometry (Wang et. al, 2017);
Right - Current model (0.2 m round receptor)

Figure 47 - Comparison of electric field along leading edge of reference and current model (0.2 m round receptor)

The mesh quality contour plot for the 0.2 m receptor arrangement as seen in **Figure 49** shows lower mesh quality (around 0.5) at regions near the blade tip. In addition,

regions critical for electric field analysis, like receptor edges are seen to have distorted geometries and corresponding lower quality meshes for the reference model. In contrast, the current model is seen to have consistent mesh quality in the range of 0.9, showing that higher accuracy is expected from the latter model.

Figure 48 - Comparison of electric field along trailing edge of reference and current model (0.2 m round receptor)
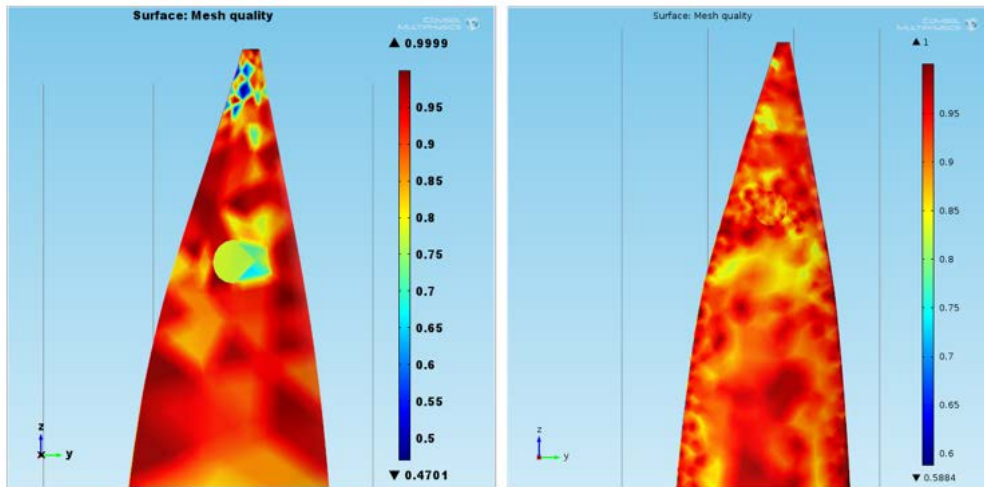
Figure 49 - Comparison of mesh quality in: Left - Reference model (Want et. al., 2017); Right - Current model (0.2 m round receptor)

`

In a similar manner, validation has been done for turbine blades with a double receptor arrangement (0.2 m radius), a tip shaped receptor and a blade with no receptor, and corresponding electric field contour plots, trailing and leading edge graphs as well as mesh quality plots have been provided in Appendix. Peak electric field from contour plots for the double receptors, tip-shaped receptor and the blade with no receptor has been found to be within 34%, 29% and 18% in comparison with the respective reference models. Mesh quality plots for the reference models show similar discrepancies which results in a difference in peak electric field values. The electric field along the trailing edge and leading edge is consistently seen to follow the same trend as that of reference model.

3.3.3 Tip – shaped conductor

Apart from what has been mentioned in the previous section, for validation of the blade model with a tip-shaped conductor, few additional issues were found in the reference model, which contributed to the difference in peak electric field and corresponding contour plot. *Figure 50* shows the comparison between electric field contour plots of reference and current model. As mentioned, the peak electric field for current model is within 29% of the reference. The top portion of the blade as shown in *Figure 50* is a conductive surface, which is connected to the ground conductor. A concentration of electric field is seen at the edges between conductor and non-conductor, acting as a point of attraction to lightning strikes.
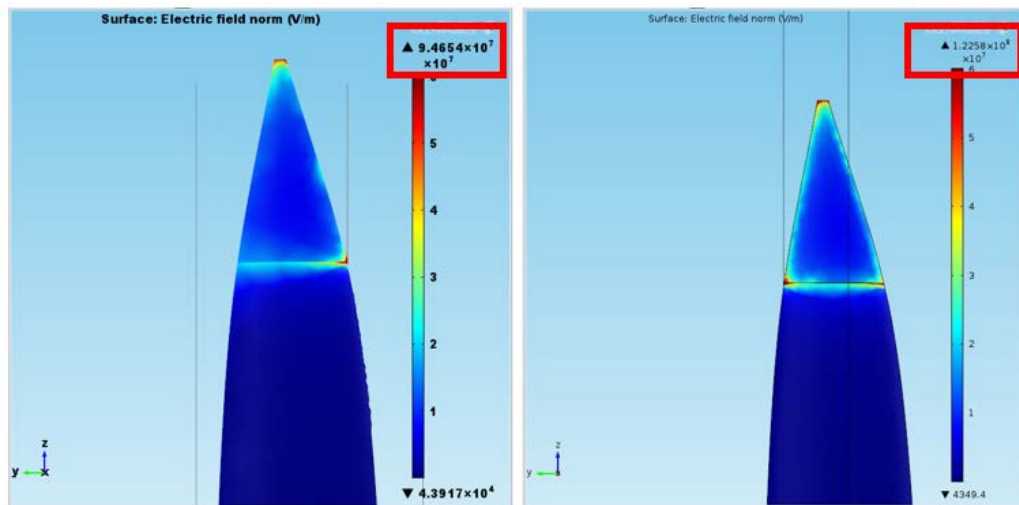
Figure 50 - Comparison of peak Electric field in: Left - Reference model
(Wang et. al, 2017); Right - Current model (Tip-shaped conductor)

One major difference to be noticed between the reference and current models is that for the reference model, a higher concentration of electric field between conducting and non-conducting layers occurs on one side of the turbine (Trailing edge), and it is relatively low on the other side (Leading Edge). This difference has occurred due to inconsistencies

`

in imported geometry within the reference model, which is seen in *Figure 51*. The rest of the results as seen in the contour plots are consistent among the two models. This difference in results is also attributed to faults in model import geometry and corresponding meshing done in the reference model.
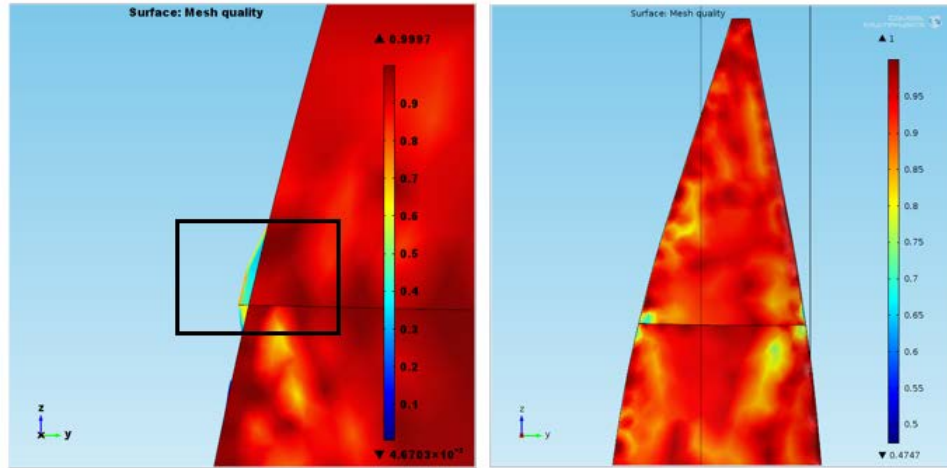
Figure 51 - Comparison of mesh quality among reference model (Left) and current model (Right) for blade with tip-shaped conductor

Figure 51 shows the difference in mesh quality between the two models, however, as pointed out in the image on the left hand side, there is a bulge in the geometry for the reference model, which is not part of the original blade model. During import and corresponding meshing of the reference model, a slight change in geometry has occurred, which causes the addition of this unintentional feature. Since, electric field is extremely sensitive to surface shape, this defect causes a concentration of electric field at this point.

The corresponding electric field along the leading edge has been compared in *Figure 52*. The reference model shows highest peak at the blade tip, and a relatively lower field at a distance of 57.3 from the blade root. This is the position of the edge connecting the conducting and non-conducting surface, where there is a concentration of electric field as mentioned. The corresponding plot for the current model shows peak currents at the same locations, but the value of the peak field is same for both the blade tip and the intersecting edge.

Since results for trailing edge from the reference model was presented as two separate graphs, the same was done for the current validation. Trailing edge data was represented using two graphs: One showing electric field along 0-57.3 m distance from the blade root, and another showing the same for the length 57.3 m to 60 m. The prior graph showed a perfect overlap of data from the two models as shown in *Figure 53*. However, due to the geometry inconsistency as mentioned earlier, there is a huge peak in electric field at a distance of 57.3 m for the reference model, showing a peak at 8.8E+07 V/m on the trailing edge, compared to a peak of 5.5E+07 V/m on the leading edge.

`

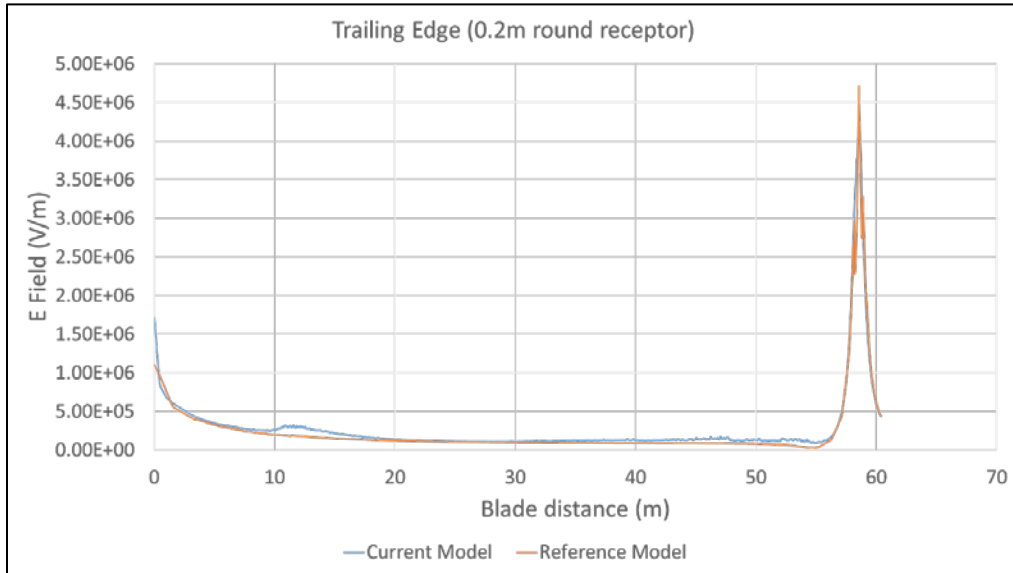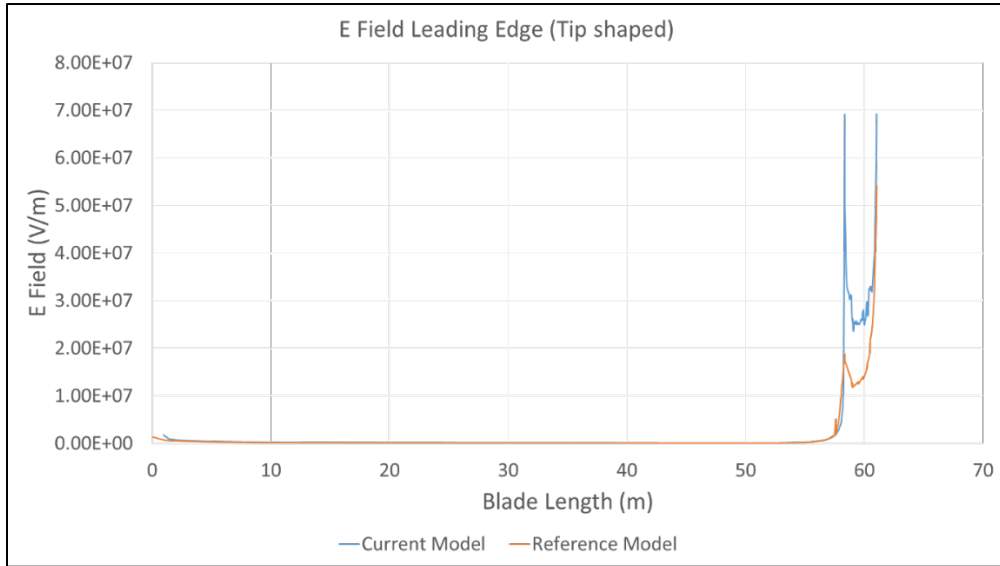*Figure 52 - Comparison of electric field along leading edge of reference and current model (Tip-shaped receptor)*
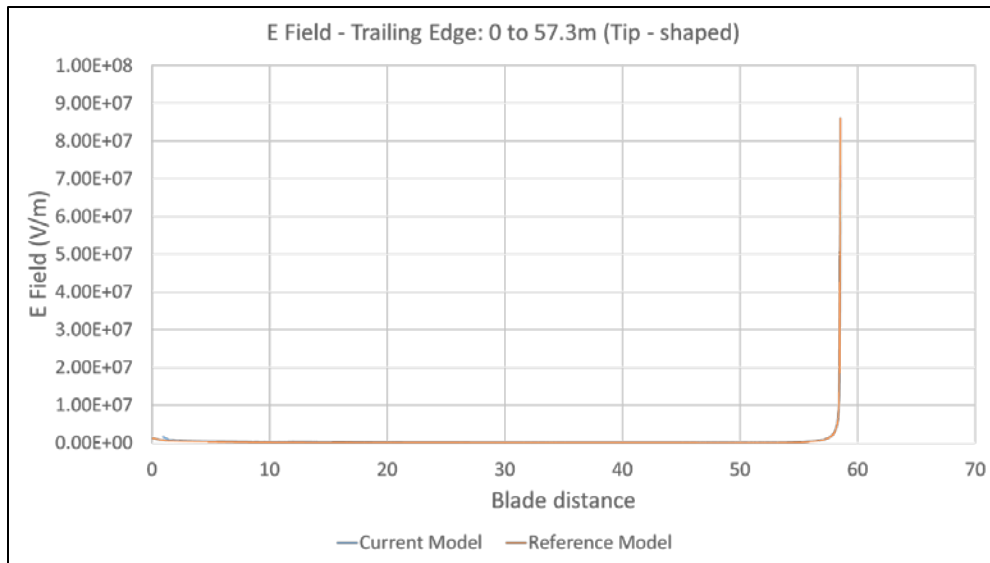
Figure 53 - Comparison of electric field up to 57.3 m along trailing edge of reference and current model (Tip-shaped receptor)

The trailing edge data from 57.3 m to 60 m however, shows some differences in electric field. **Figure 54** shows the corresponding electric field plots for the two models. The dotted lines represent the actual data obtained, and the solids lines in graph are 6th order polynomial trend lines for the same. Since this graph is used to show data from a comparatively small edge from the trailing edge, the number of mesh elements

56

corresponding to the edge are very low. This low mesh resolution results in data that is relatively not smooth as represented by the dotted lines.
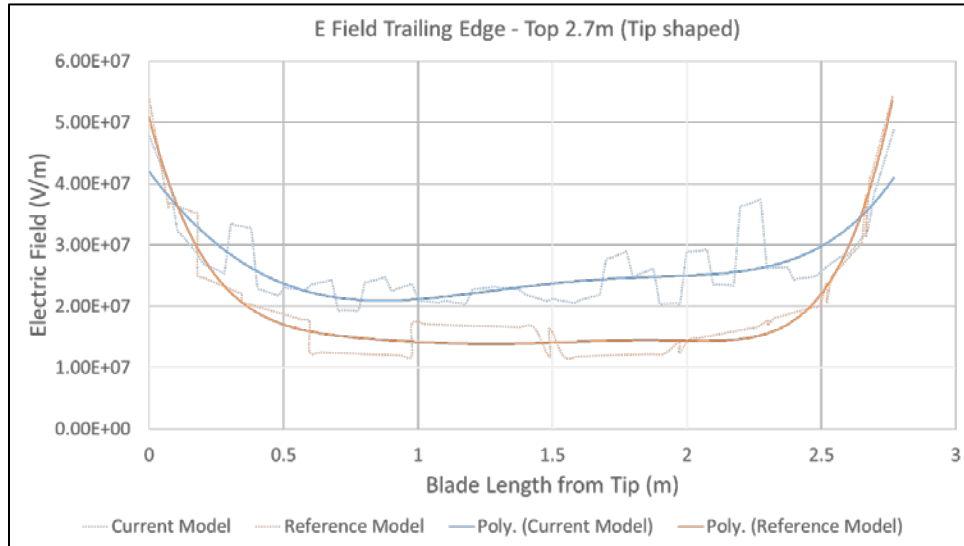
Figure 54 - Comparison of electric field from 57.3 m to 60 m along trailing edge of reference and current model (Tip-shaped receptor)

Even though there is a difference between the values of electric field generated on the trailing edge, a common trend is seen among the two models.

Taking the validation results for all 4 receptor models (and 1 blade model without receptor) into consideration, it can be established that the current models for calculating electric field around a wind turbine blade due to lightning leaders has been thoroughly validated using prior research done in the area. Any variation in results from the reference study has been looked into, and possible reasons for said difference has been explored and pointed out.

Any further changes to the receptor shape and/or size to affect the electric field around the blade would potentially produce results, which are reasonably accurate within the scope of this study, as long as other parameters of the model are not changed.

CHAPTER 4 . NUMERICAL MODELING OF ELECTRIC FIELD ON TURBINE BLADES

One of the most commonly used approaches to determine the effects of lightning on wind turbine lightning protection systems is visual observation and recording the frequency of lightning occurrence as seen in some experimental studies described in Section 2. The same approach is used for the current experimental study, where a number of test runs are done to determine the behavior of electric sparks in the presence of a conductive pattern.

A high voltage electrode is introduced near a grounded conductive pattern at specific heights and the position of spark attachment on the conductive board is recorded. One hundred such strikes are simulated for same position of the spark emitter with respect to the conductive board to reduce the error obtained from data. The same experiment is repeated for different positions of the spark emitter, and the points of spark attachment are recorded. At a particular position, the regions of the conductive pattern which attracts more sparks can be used as reference to model new LPS designs on turbine blades. This was the objective of experimental analysis.

An FEM simulation was also done to replicate the experimental setup. The Comsol model used physics and modelling techniques used in the previous chapter to recreate parts of the experimental setup to analyze the electric field produced around the patterns for each position of the spark emitter. This was done to find a correlation between electric field obtained from FEM simulation, and the corresponding spark attachment points obtained from experimental observation.

4.1 Experimental Setup

The aim of conducting an experimental study for this research was to observe the effects of a high voltage spark on a conductive pattern. Although the most suitable setup would have included a spark emitter which exactly mimics the lightning peak voltage in the range of 40 MV as described in section 2, a much scaled down setup in terms of maximum voltage was constructed due to constraints in available resources. The maximum voltage achieved in this setup was approximately 100 kV.

Although a direct comparison cannot be made with lightning behavior, this setup provides an insight into how sparks behave in the presence of the proposed conducting patterns. In addition, this experimental study acts as the basis for future tests that can be done on similar patterns in a full scale lab setup capable of achieving higher voltage levels.

`

The current setup consists of 4 components as shown in *Figure 55*:

1. 30 kV voltage supply

2. 8-stage Marx Generator

3. Conductive patterns on PCB

4. X-Y positioning table
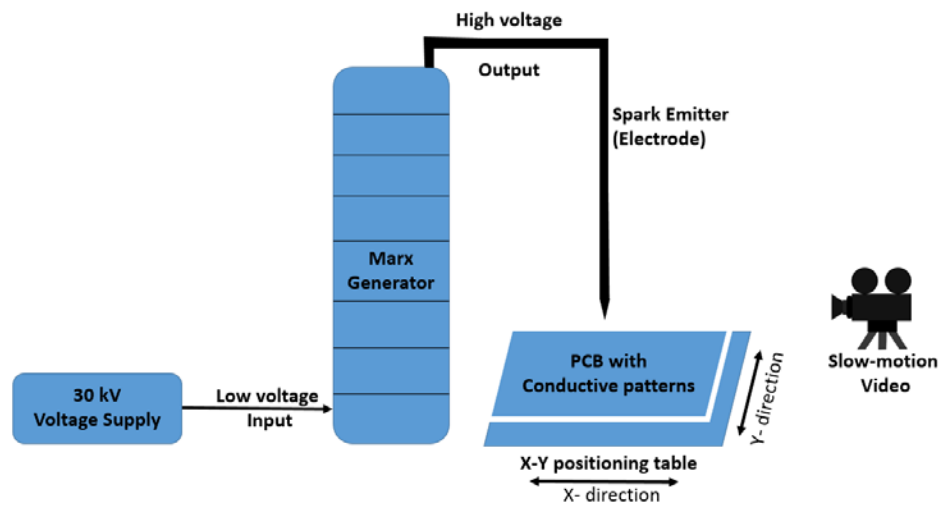
Figure 55 - Schematic of Experimental setup
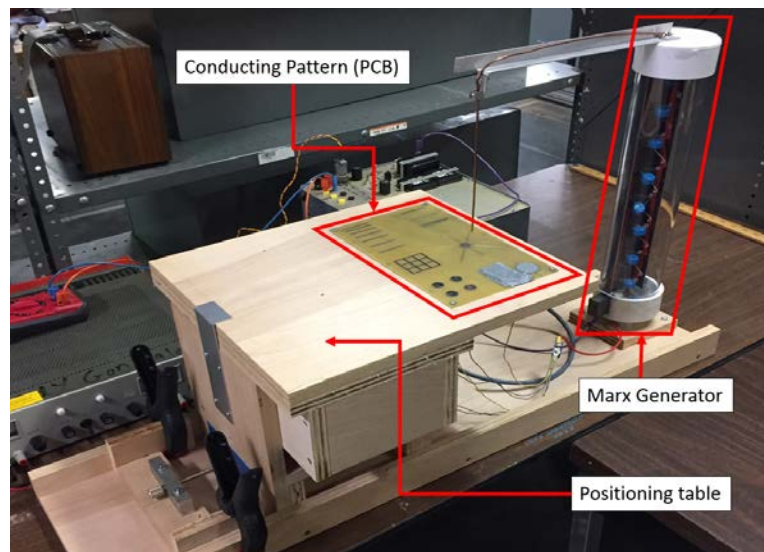
Figure 56 - High voltage test setup

`

A constant voltage of 30 kV and was introduced to the Marx generator from a DC supply. This supply acts as the low voltage input for the Marx generator which then, converts this input into a high voltage intermittent output through 8 stages as explained earlier. The output voltage is connected to a copper electrode which acts as the spark emitter, and the tip of this electrode is placed in particular positions with respect to the PCB board. The Board is attached to a positioning table, which has relatively controlled movement in the X-Y direction. Each experimental run is captured using a slow-speed camera for data collection. The physical setup corresponding to the schematic can be seen in *Figure 56*.

4.1.1 30 kV Power Supply

A DC power source was used to provide the input voltage to the Marx generator. The 30 kV supply was custom built by Dr. Charles Moore and his research group from New Mexico Tech in 1988, and sourced for the current research by Dr. Richard Sonnenfeld. The original application for this power source was to study frictional charging in helicopters. The 30 kV output from this power source acts as the low voltage input into the Marx generator, which subsequently gets multiplied through different stages as explained earlier. The power supply provides up to +/- 30 kV DC at up to 0.33 mA output current. The voltage was programmable, and the instrument was manufactured by Gamma High Voltage Research – a company based in Ormond Beach, Florida and founded in 1981. *Figure 57* shows an image of the 30 kV power supply used for the current study.

Figure 57 - 30 kV DC Power supply

4.1.2 Marx Generator

As mentioned earlier, the Marx generator acts as a temporary current storage device, in which an input voltage gets multiplied through a number of stages as shown in *Figure 30*. The stages in the current setup are arranged vertically as can be seen in

Figure 58. The highest potential within the generator is attained at the top most stage, and this high potential lead is connected to the copper spark emitter shown in ***Figure 58***. The ground lead from the Marx generator is connected to the bottom side of the PCB (ground connection), which has pad connectors in electrical contact with all conductive patterns on the PCB board, through via connections. Once the high potential is obtained on the spark emitter, breakdown of air between the PCB and spark emitter occurs and a corresponding spark is generated, which attaches to different points on the conductive patterns.
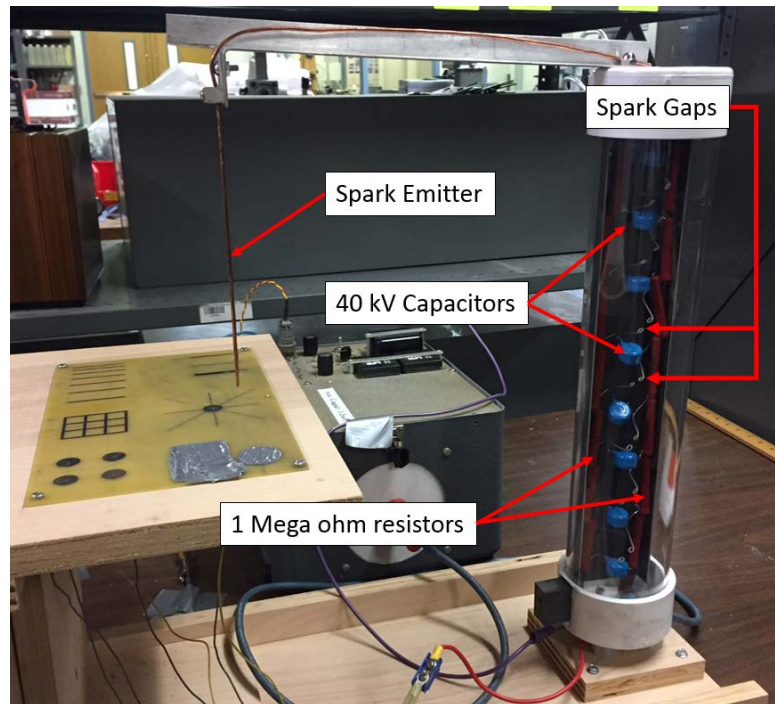
Figure 58 - Small scale Marx generator setup

Eight stages are used in the current Marx generator setup, using fourteen 1 Mega-ohm resistors and nine 0.001 μF 40 kV capacitors. The spark gaps are made of stainless steel wires, which can be adjusted to change the spark gap distance. The position and height of the copper spark emitter in the setup can be changed manually. Standard conducting materials like Copper and Aluminum are used for all connections within the Marx generator circuit.

PVC casings were used as the supporting structure for the generator setup, including the vertical board on which the resistors and capacitors were mounted through drilled holes. All connections were made with reference to the circuit diagram shown in ***Figure 29***. The corresponding R_{Load} shown in Figure is the air between the spark emitter and conductive patterns, acting as the resistance to be overcome for a spark to form. The Output switch is however, not adjacent to the R_{Load} as seen in the circuit diagram, but is controlled by a switch to turn the voltage source on and off.

The PVC board used to mount the Marx generator circuit components was not ideal for this setup as seen during test runs. Due to the buildup of potential on the capacitor leads, sometimes breakdown of the plastic between these leads occurred at lower stages in the Marx generator, causing a short circuit current to flow on the plastic surface towards ground before the charge reached the subsequent stages. This breakdown of plastic meant that a permanent conductive pathway had been created between the two leads of a capacitor within the circuit, thus restricting the flow of current to that particular stage. This occurred twice during experimental runs and the damaged plastic between the leads had to be cut out using a Dremel tool, to get rid of the unintentional conductive pathway between capacitor leads.

4.1.3 Conductive patterns on PCB

Printed Circuit Boards were selected to represent the conductive patterns for experimental testing due to ease and accuracy of design and similarities in material properties with respect to turbine blades. The conductive material in consideration for this study was copper and the FR-4 polymer used as base material for the PCB is made of woven fiberglass strands bonded with an epoxy resin. This is similar to the composite polymer used in blade material. Since material damage characteristics are not of concern in this study, the cross-section of conductive patterns and FR-4 polymer thickness are not important, since they affect only the current carrying capabilities (and corresponding material damage), and not necessarily the lightning attachment points, as being observed in this study.

The pattern designs were made using the PCB Artist software provided by Advanced Circuits – a PCB manufacturing company. Two patterns were designed for the current study, and manufactured using standard specifications provided by the company. A 6 in x 10 in board was used for both PCB designs. The first board design consisted of several patterns for testing. *Figure 59* shows the different patterns in the first PCB design used for this study. The patterns designed in this PCB was intended to test different characteristics of conductive patterns including distance between different conductors, thickness of conductive bars, size of circular conductors and the influence of a conductive mesh on lightning strikes.

However, all the intended tests were not conducted on the patterns. During test runs of the setup using Pattern 1, the Marx generator setup faced issues in plastic breakdown due to high voltage as discussed earlier in section 4.1.2. The plastic materials used in the current setup would not be able to handle such high voltage levels over long test periods. As such, only one parameter was focused on for the rest of the research. Since distance between conductive patterns was a major point of interest for design, only the pattern region intended for that study was used. *Figure 60* shows a closer image of the pattern in consideration, along with the dimensions and thicknesses used. The red regions shown in Figure represents a copper layer on top of the FR-4 board, with a standard weight of 1 oz./ft^2. As seen in image, the distance between conductive bars is lowest at the right most bars, and is highest between the bars on the left, with a constant gap increase of 100 mil between the different bars. The blue lines indicate copper connections made on the bottom

layer, and connected to the top layer through via connections, represented by yellow circles.
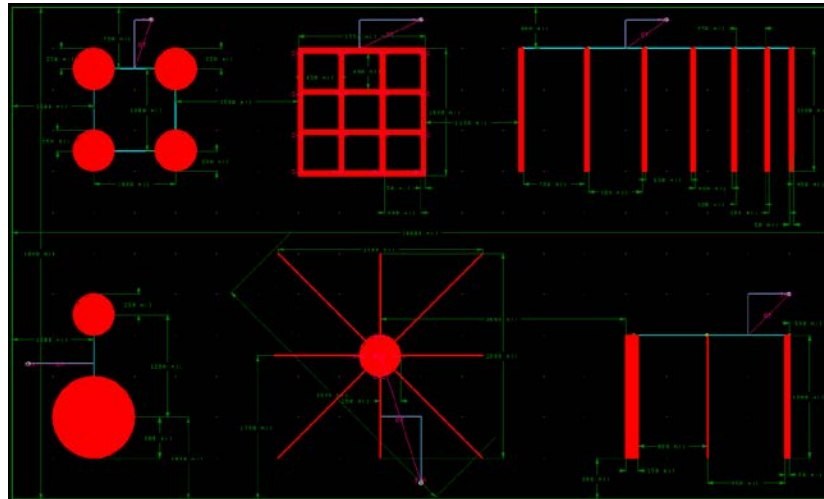
Figure 59 - PCB Layout for pattern 1
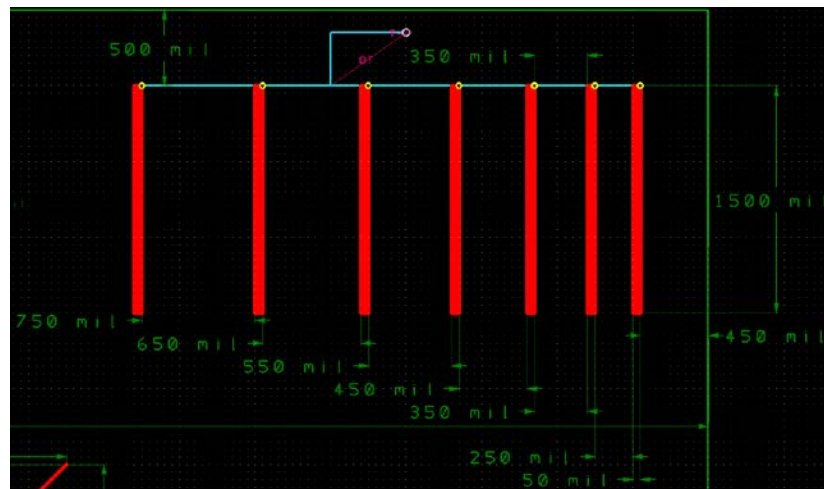
Figure 60 - Rectangular bar arrangement in pattern 1 (PCB Artist)

The corresponding manufactured PCB for the patterned design is shown in *Figure 61*. A silkscreen and solder masks are normally used as protective layers on PCBs, but since for our study, we require uncovered copper surfaces, these layers were not added by the manufacturing company.

`
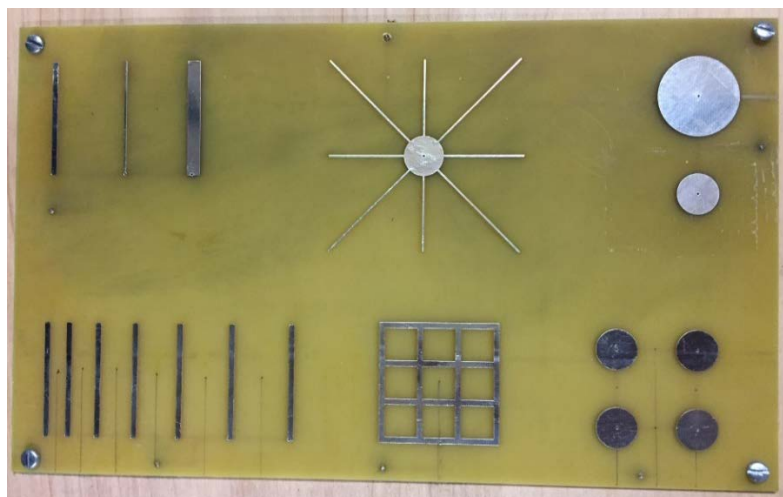
Figure 61 - Manufactured Pattern 1 (Sourced from Advanced Circuits)

For the pattern in consideration, there were seven 50 mil wide bars of 1500 mil length with different gap lengths as mentioned earlier. The spark tests were conducted for 13 positions of the spark emitter with respect to the PCB. *Figure 62* shows a schematic of the pattern, and corresponding conductive bars and test positions. For ease of representation of bar position and spark emitter position, a simple naming convention was used. The conductive bars are named B1 to B7 and the spark emitter positions are number 1 to 13, and are represented by the 'x' shown in *Figure 62*. These positions correspond to the spark emitter placed directly above each conductive bar, as well as exactly in between two adjacent bars (within the accuracy constraints of the current setup). As mentioned earlier, 100 strikes are observed at each position, and the frequency of strikes on each bar is counted. In addition, other observations regarding the point of spark attachment are also noted, which will be discussed in detail in Section 5.
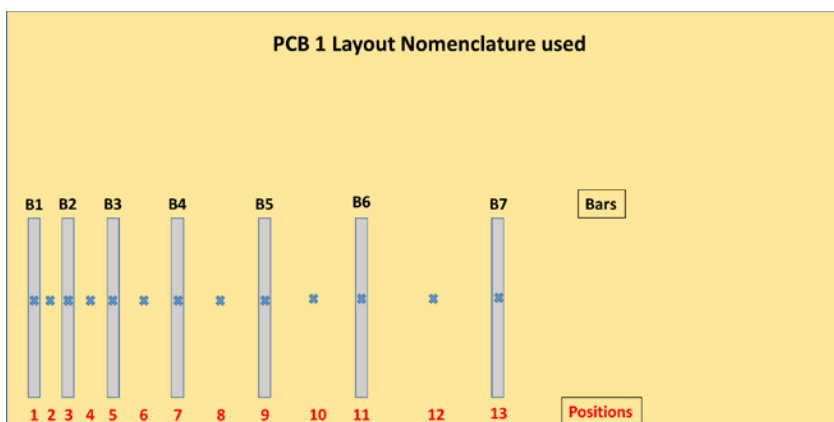
Figure 62 - Nomenclature to denote bars and positions in Pattern 1

`

Since multiple patterns were designed on the same PCB, there were limitations on the distance between two adjacent conductive bars which could be achieved. The maximum distance between bars achieved in the first pattern design was 750 mil. In order to conduct a more comprehensive study on the effect of conductor spacing, another patterned PCB was designed which focused solely on spacing between conducting bars. *Figure 63* shows the second PCB design, with spacing ranging from 450 mil to 2850 mil. As in the previous pattern design, the red regions represent top layer and the blue regions represent bottom layer of the PCB design. The bottom layer copper strip has a thicker width in this pattern to ensure proper electrical contact.
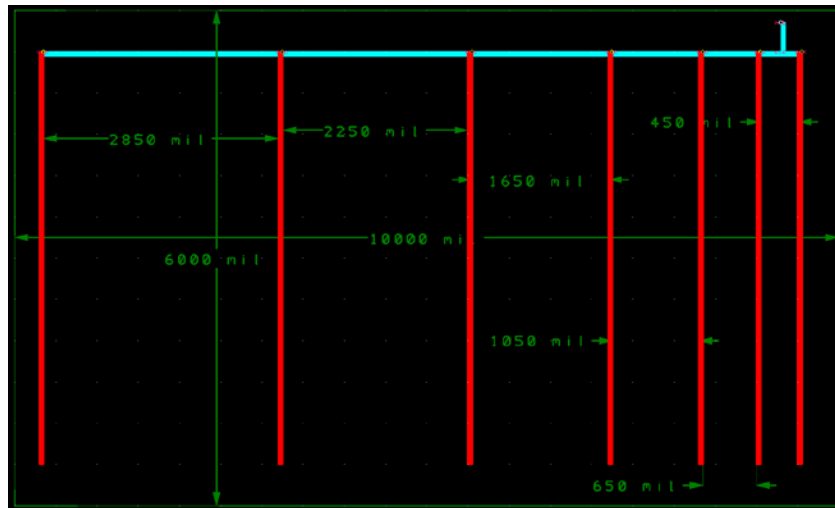
Figure 63 - PCB Layout for Pattern 2 (PCB Artist)
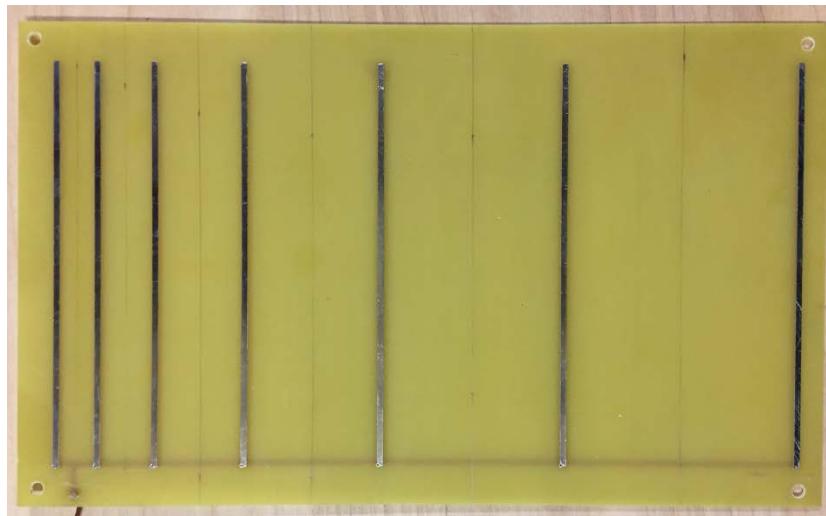
Figure 64 - Manufactured Pattern 2 (Sourced from Advanced Circuits)

`

The corresponding manufactured PCB for pattern 2 is shown in *Figure 64*. The board is screwed onto the X-Y positioning table for controlling horizontal movement. Similar to the previous patterned PCB, the naming convention used, and spark emitter positions are shown in *Figure 65*.
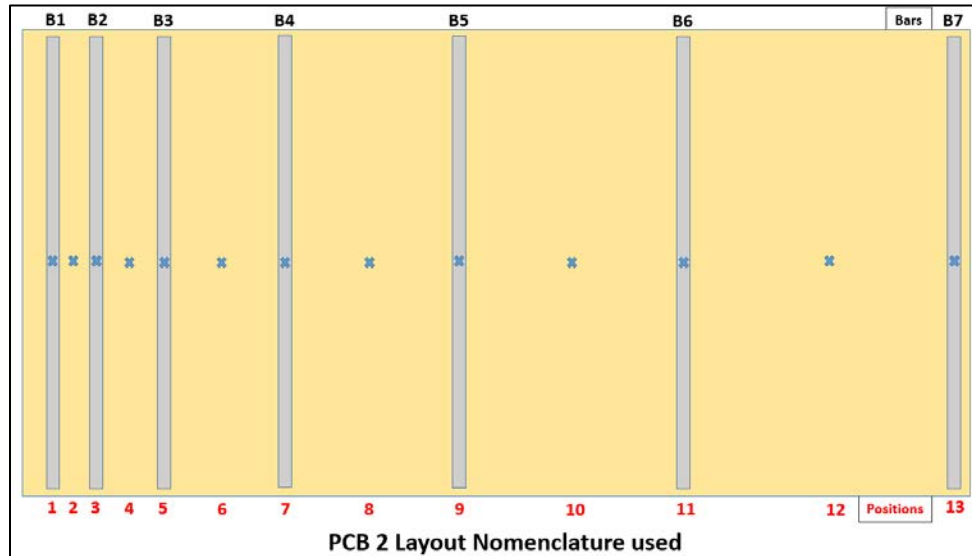
Figure 65 - Nomenclature to denote bars and positions in Pattern 2

Each of the test runs for all positions of the spark emitter is done for different heights of the spark emitter tip from the PCB board. The experiment is repeated for heights of 1-5 cm from the board surface, with increments of 1 cm. This height is changed manually and the spark emitter further tweaked to ensure that it stays vertical each time it is changed.

4.1.4 X-Y Positioning Table

The current experimental setup required controlled movement in all three axes. To facilitate this, movement in the vertical direction was made possible by changing the spark emitter height manually as discussed earlier, whereas to control the lateral motion of the PCB, a positioning table was fabricated as shown in *Figure 66*. It consists mainly of a sliding stage on a long wooden base. The movement along the direction of the length of the wooden base contributes to controlled motion in that particular direction – assumed to be X direction. The sliding stage consists of a table, on which the PCB is screwed on. This table rests on two rails which allow movement in the Y direction (90° lateral to X - direction).

Since precision tools were not used to fabricate this setup, fine movement in the Y-direction was not possible. Small gaps were found between the rails and the table surface on the stage, which caused the table to get stuck during movement in the Y-direction making fine adjustments difficult to achieve. It was found during test runs that for positions

`

of the spark emitter in between two adjacent conductive bars, the spark attachment point on the PCB was extremely dependent on the accurate position of the spark emitter. A minute change in position would result in a significant difference in results obtained, especially at lower heights of spark emitter.

To make this fine adjustment possible, a screw-type control knob was fabricated using an aluminum block fastened onto a wooden plank, which slides on the wooden base (***Figure 66***). Clamps were used to fix the control knob's position with respect to the wooden base, whenever fine adjustments were to be made on the sliding stage. This way, the X-directional motion was controlled to a higher degree of accuracy, and the PCB was arranged in a way that made only this movement critical to accuracy of results (Position of spark emitter along the length of each conductive bars - i.e. Y direction, is not as critical).
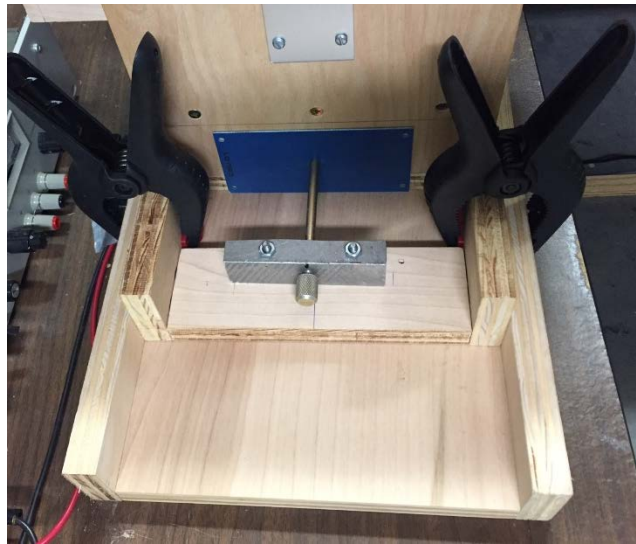
Figure 66 - Fine adjustment control knob for X – directional movement

4.2 Test Procedure

The procedure followed for both the test patterns were same, and as such will be summarized together in this section.

As shown in ***Figure 62*** and ***Figure 65***, thirteen positions of the spark emitter were considered for testing of each pattern for the experimental runs. First, the spark emitter, which is basically a copper wire of thickness 0.11 in, was attached to the end of the aluminum bridge as can be seen in ***Figure 58***. Before fastening the spark emitter into position, the distance between spark emitter tip and board surface was measured and set, according to the particular test run (1 – 5 cm). This distance was called "spark distance" for reference in our current study. Once the spark distance was adjusted, the copper wire was fastened onto the aluminum bridge, and using a combination square, the alignment of

`

the copper wire was adjusted such that it was exactly vertical in orientation. The spark distance was measured again to verify that it had not changed during re-alignment.

From *Figure 61* and *Figure 64*, the presence of few marking lines on the PCB surfaces can be observed. These lines, which fall exactly in between adjacent conductive bars were manually drawn using a pencil. For positioning of the PCB with respect to the spark emitter, the combination square was used again. The L-shaped corner of the square was placed on the pencil mark at the edge of the PCB. Looking straight into the face of the combination square, the pencil line and the spark emitter tip was aligned with the vertical edge of the combination square. This ensured that the spark emitter position was exactly at the center of two adjacent bars for such positions. A similar approach was taken in the case of positioning the spark emitter directly above the conductive bars as well.

Once the positioning was fixed, the DC voltage source was switched on, upon which an intermittent sparking occurred between the spark emitter and PCB. Sparks were emitted at constant time intervals during which charging of capacitors took place between each spark. The phenomenon was recorded using a standard Apple i-phone 6, using its slow-motion video feature, which records at a rate of 240 frames per second, as opposed to the 30 frames per second used for normal video recording. This feature was able to capture each spark, and the corresponding point of attachment could be determined. Each test run was done for approximately 45 seconds, which was completely recorded.

Once each test run was completed, the recorded video was played to count the number of strikes occurring at each conductive bar to perform a frequency distribution analysis. The first 100 strikes were counted and distributed along the seven corresponding bars, and the rest of the strikes were ignored. Once the data was recorded, the position of PCB was changed such that the spark emitter is placed above the next position. Fine adjustments during positioning were done using the control knob shown in *Figure 66*. This process was repeated for all 13 positions.

The spark distance was then readjusted manually, and the process of aligning it vertically was repeated. The subsequent steps followed to record data are the same as mentioned before. Data was collected for spark distances from 1-5 cm as mentioned earlier, and the results were analyzed. Results from this study along with observations and inferences are provided in Chapter 5.

Leads from the Marx generator were also connected to an oscilloscope through a high resistance voltage divider, in order to measure the actual peak voltage developed across the Marx generator. However, it was found that electromagnetic pulses generated by the Marx generator during operation heavily interfered with the signals recorded by the oscilloscope, thus restricting the possibility of recording voltage through this method. Thus, due to constraints in available instruments and time, voltage measurement was not done, and an assumed value of 100 kV was taken as the voltage across the spark emitter for FEM modelling purposes. This is considered a reasonable assumption since the Marx generator was designed for producing approximately the same potential. Even though theoretically the output voltage desired would be much higher, generally complete

multiplication of the voltage does not occur at each stage in the generator circuit, and as such the practical voltage output from the setup is lower than theoretical estimations.

In the current study however, importance is given to the relative difference in electric field between two adjacent bars, and as such the absolute voltage across the electrode is not as critical. A different electrode potential would change the absolute electric field values on the conductors, but the same trend for difference in electric fields between would be observed. Thus, the assumption of electrode potential within reasonable values is justified. However, for future studies related to this project, it would be beneficial to have a more accurately measured value for electrode potential.

4.3 FEM models of Lab Setup

To find a correlation between point of maximum strikes and electric field generated due to the electrode, an FEM model was created in Comsol to replicate the lab setup. A model was created corresponding to all 13 positions for a particular spark distance. However, spark distances of 1 cm, 3 cm and 5 cm were only modelled, since they represented the general trend of increasing the spark distance.

Taking concepts used for model validation as shown in chapter 3, the FEM simulations for the lab setup was generated. *Figure 67* shows an image of the complete domain modelled for the lab setup. The patterned PCB is modelled first using specified dimensions from the manufacturer. Thickness of the copper surfaces is negligible, and as such, were ignored in the model. It was instead modelled as a 2D surface on the PCB, such that they can be separately selected and assigned with a "ground" boundary condition. A large domain (compared to the PCB board dimensions) of 25 in x 25 in x 235 m was modelled around the board, and assigned with material properties of air. A cylindrical electrode of radius 0.11 in which represents the spark emitter was also modelled. A cone of height 6 mm was included in the electrode geometry to represent the tip at the lower end of the spark emitter. All the above mentioned dimensions were obtained by measuring the physical model with a caliper.

Since the electrode is a conductor applied with a voltage of 100 kV, a cylindrical cutout was made similar to the PCB within the same model, and all electrode surfaces were assigned with a 100 kV surface potential. Conductive surfaces on the PCB was assigned with ground boundary condition and the rest of the surfaces in the domain retained the default open boundary condition to represent non-conductive surfaces, as was done in the validated models. *Table 4* shows the mesh parameters used for all Comsol models of the lab setup.

To ensure that sufficient data points are available on the edges of the bar, which are points of interest for our study, an edge distribution feature was used on these bar edges, dividing each edge into 250 different mesh points. A free triangular surface mesh feature was assigned to the rest of the PCB surface, and the rest of the entire model domain was assigned with a free tetrahedral mesh setting. The comprehensive list of mesh parameters

used for the free triangular surface and free tetrahedral volume meshes are shown in in **Table 4**.
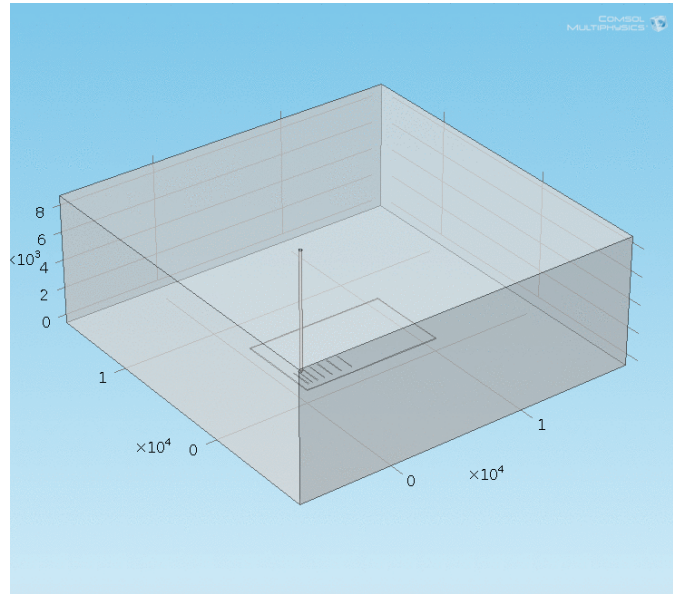
Figure 67 - Comsol model for FEM analysis of Electric Field in Experimental setup

Table 4 - Number of high voltage discharges to polluted and non-polluted blades (Yokoyoma et. al., 2013)

Mesh Parameter	Free Tetrahedral (Volume)	Free Triangular (Surface)
Max. Element Size (mil)	1000	500
Min. Element Size (mil)	1	1
Max. Element growth rate	1.5	1.2
Resolution of curvature	0.6	0.2
Resolution of narrow regions	0.5	0.3

`

A close-up image of the transition of mesh size near the conductive bars can be seen in *Figure 68*.
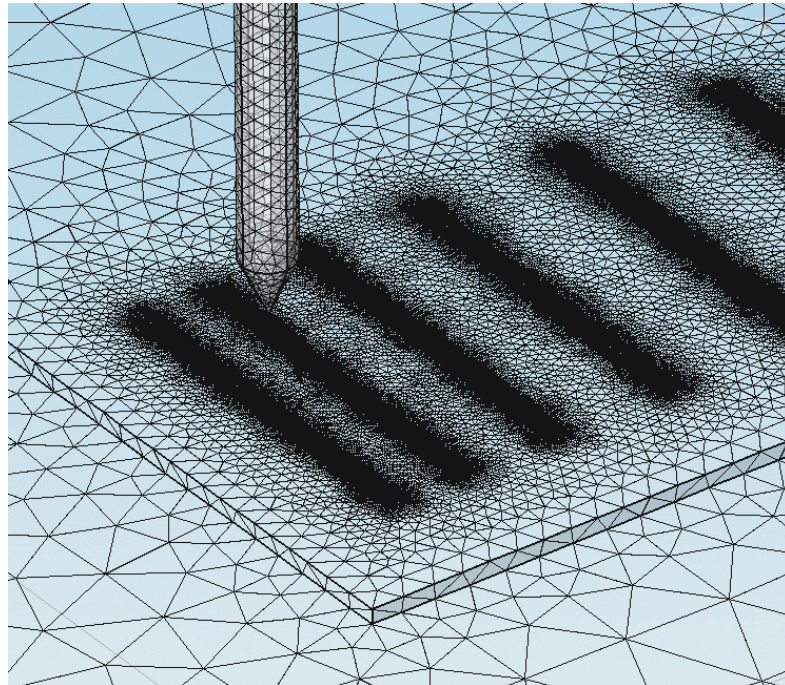
Figure 68 - Fine mesh used on conductive patterns on PCB – FEM analysis

By using the mesh features listed above, higher accuracy is expected for the model results than what would be generated from normal mesh settings. Similar mesh parameters were used for the second pattern as well, however, each bar edge in the case of the second pattern was divided into 500 sections because its length was bigger than pattern 1, as can be seen by comparing *Figure 60* and *Figure 63*. The different models were analyzed for steady state electric field as done in the validated models, and results exported into excel data, for processing. Results and corresponding inferences for all models are presented in the next section.

`

CHAPTER 5 . RESULTS FROM EXPERIMENTAL ANALYSIS

The aim of this experimental analysis was to observe the general characteristics of spark attachment in the presence of patterned conductors. In addition, the study aimed at finding a correlation between electric field and probability of lightning strikes. Patterns of conductive bars were created and subject to high voltage sparks at different positions of the spark emitter. A distribution of sparks among different conductive bars meant that they attracted the spark with equal intensity. Conversely, a concentration of spark attachments on a single conductive bar meant that the spark was attracted strongly by that particular conductive bar, compared to the adjacent bars.

Therefore, FEM models were created corresponding to all such test runs to find static electric field around the conductors for each position of the spark emitter. The difference in electric field between the conductive bars were correlated with number of sparks attached to the bar, thus giving an insight into the relationship between electric field and spark attachment.

5.1 Experimental Results and Observations

A frequency distribution analysis was done on the number of electric strikes falling on all conductive bars for each position of the spark emitter, as discussed in the previous chapter. The raw data contained number of strikes on all 7 bars for each of the 13 positions for a set of 100 sparks observed for each test run. The experiment was repeated for spark distances of 1,2,3,4 and 5 cm. Representing data for each of these experimental runs, 130 graphs were generated in total for tests conducted for both patterns.

For ease of representing all available data, a surface plot was generated for each spark distance, thereby reducing the number of plots to ten. It was observed that results obtained for spark distances of 1 cm and 2 cm are very predictable, as will be explained in the next section. As such, only the experimental data for spark distances of 3 cm, 4 cm and 5 cm have been discussed in detail.

5.1.1 Experimental Results for Pattern 1

The experimental analysis started at a spark distance of 1 cm, and as expected for such small distances, when the spark emitter is placed directly above the conductive bar, all of the sparks tend to hit the conductor directly beneath it. One interesting observation from test runs at spark distances of 1 cm and 2 cm was that when the spark emitter was kept at the center of two adjacent conductive bars, sparks were emitted towards both the bars at the same time, and they were both hit with a spark simultaneously as shown in *Figure 69*.

One of the objectives of this study was to observe which conductor would attract more number of sparks when the electrode was placed in the center of two adjacent bars.

`

As mentioned, at smaller distances it was seen that sparks were emitted towards both conductors. At larger distances however, this phenomenon was not observed and the sparks tended to strike one conductive bar at a time as seen in *Figure 70*.
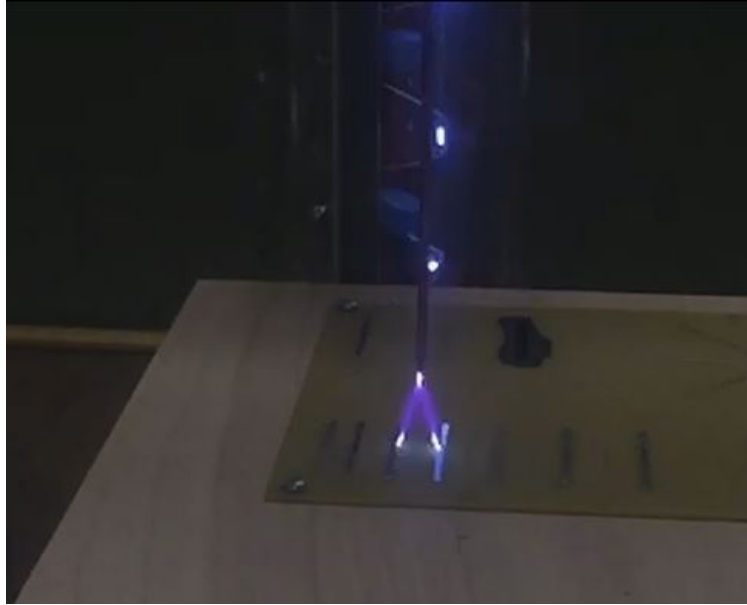
Figure 69 - Simultaneous sparks when emitter is placed in between two adjacent conductive bars
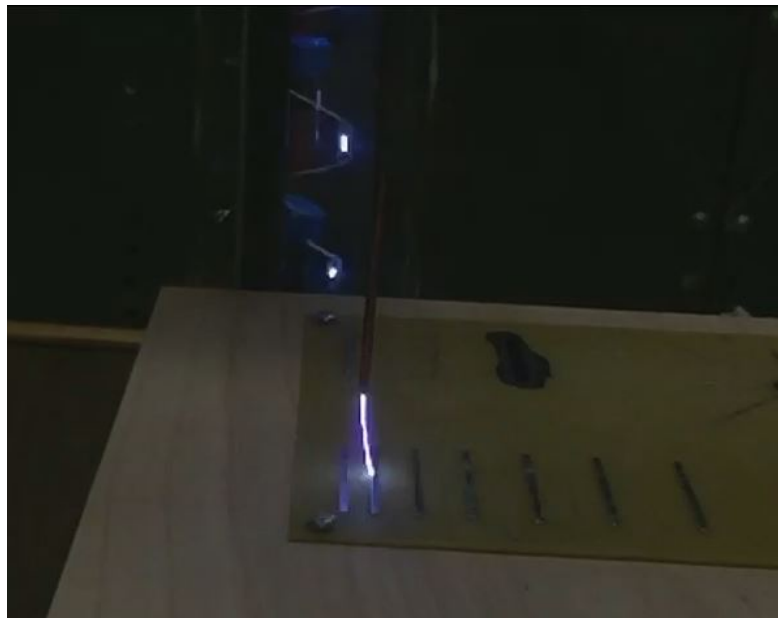
Figure 70 - Single spark attaching to a conductive bar

Figure 71 – Figure 73 shows surface plots depicting the number of strikes (out of 100 strikes), which attached to different conductive bars at each position of the spark emitter. It should be noted that each of the surface plots represent 13 test runs done on the pattern at a particular height, keeping the spark emitter at different positions. Due to difficulties in estimating the values for number of strikes in the 3D surface plot, a color scheme is also included, along with a legend to show the values corresponding to each color. For example, in *Figure 71*, most of the peaks are colored in yellow, signifying that the corresponding number of strikes (in this case, yellow = 100 strikes), attached to the corresponding bars when the spark emitter was at particular positions. In *Figure 71*, hundred strikes on the conductors occur at spark emitter positions 5, 7, 9, 11 and 13 on conductive bar numbers 3, 4, 5, 6 and 7 respectively according to the pattern nomenclature described in *Figure 62*.

It should be noted that each (differently colored) peak in the surface plots represent a single data point taken from experimental analysis, and as such, the surfaces connecting two peaks should be ignored. For example, in *Figure 71*, data is plotted for discrete spark emitter positions like 9 and 10, but these two data points are connected by a continuous surface in the surface plot. So by observing the plot, data can be extracted for non-existent spark emitter positions like (say) 9.6 also, however, that would be meaningless. Therefore, as mentioned earlier, only the peaks in the graph, representing discrete spark emitter positions are to be considered, and the surfaces connected different peaks are to be ignored while reading the graph.
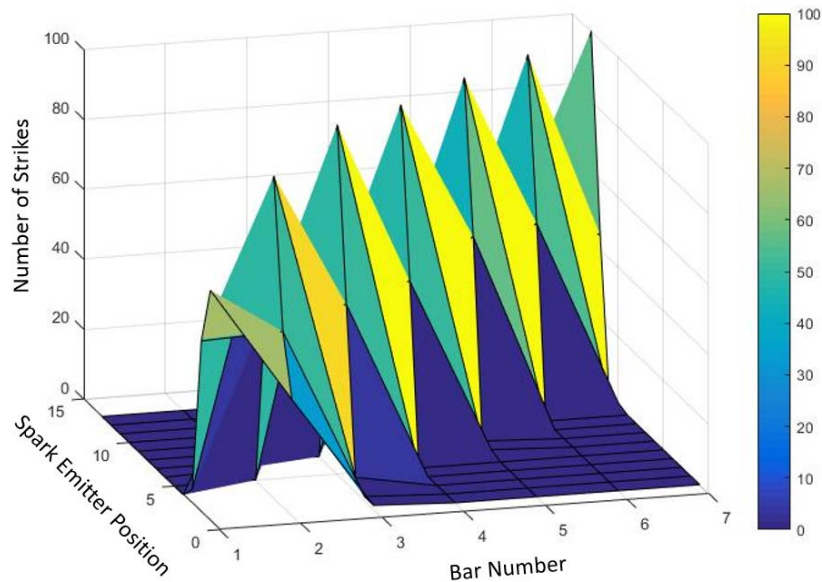
Figure 71 - Frequency distribution analysis for Pattern 1
(Spark distance = 3 cm)
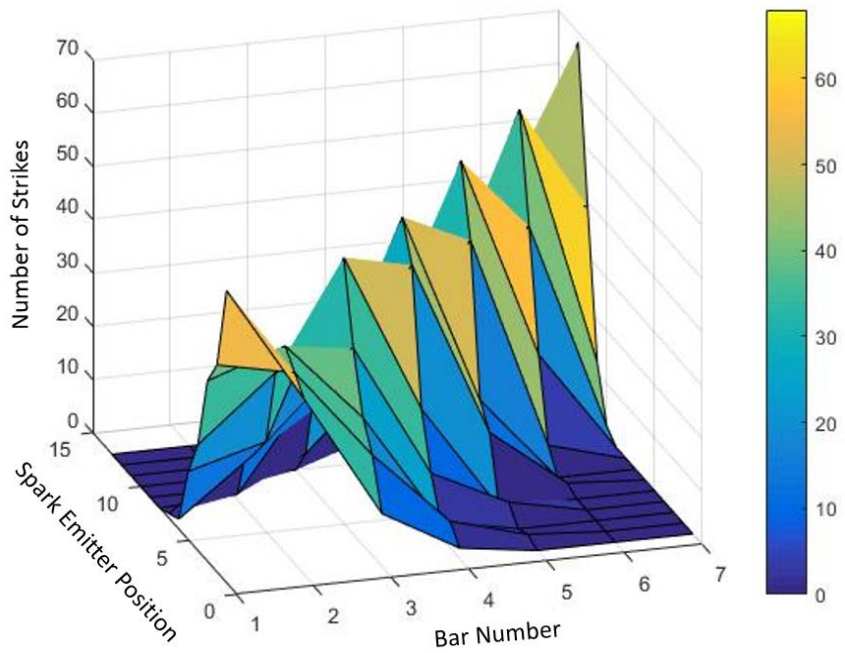
Figure 72 - Frequency distribution analysis for Pattern 1
(Spark distance = 4 cm)
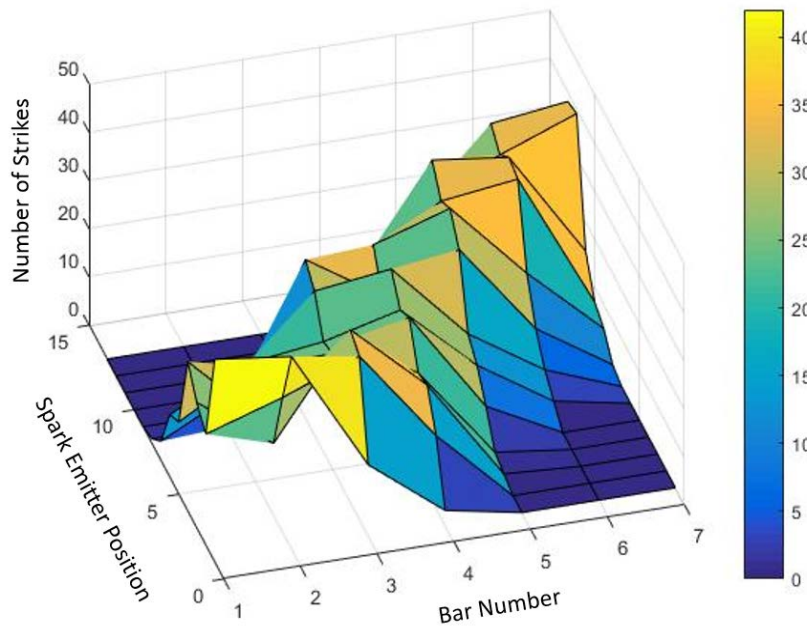
Figure 73 - Frequency distribution analysis for Pattern 1
(Spark distance = 5 cm)

`

It can be observed from the above illustrated Figures that as the spark distance increases, the spark attachments get more distributed among the different bars. At 3 cm spark distance, there is only a slight distribution of sparks that can be seen close to spark emitter position 1. The rest of the peaks are all at 100 sparks or very close to 100 (when the spark emitter is directly above the conductor), telling us that there is no distribution of sparks at that position.

When the spark distance is at 4 cm, more distribution of sparks is seen, even when the spark emitter is directly above the conductive bar. The maximum number of sparks on a single conductive bar is 60 strikes at these positions. Further, when the spark distance is increased to 5 cm, much higher distribution of sparks is seen as shown in *Figure 73*. The maximum number of strikes observed on a conductive bar is 40, and in many cases, the strikes are more evenly distributed among many conductive bars, as opposed to a concentration of sparks found in the bar right underneath the spark emitter, in the earlier two cases of spark distance.

One of the limitations of this pattern was that for each spark distance case, a particular trend was observed to be followed by the entire surface plot. For example, in *Figure 73*, when the spark distance is at 5 cm, the sparks are seen to be distributed among adjacent bars. This trend is seen for all spark emitter positions ranging from 1 to 13. This makes it difficult to estimate if distribution of sparks (or concentration of sparks) is an attribute of electric field or spark distance. A change in trend for the same spark distance – possibly from distribution of sparks to concentration of sparks on one conductive bar would have been an ideal result – thus eliminating the influence of spark distance on the results obtained. This was the motive behind designing Pattern 2 for the current study.

5.1.2 Experimental Results for Pattern 2

Similar to results obtained for the first pattern, surface plots were generated for the second pattern. Data for spark distances of 3 cm, 4 cm and 5 cm were represented using the same technique. There are some slight variations in results, compared to the first pattern. The major difference between the two patterns is that distance between two adjacent conductors is much larger in the second pattern. As such, the effect of distance between conductors was more prominent for results obtained from this pattern. *Figure 74 - Figure 76* shows the surface plots for number of strikes on the seven bars for 13 positions of the spark emitter.

Similar to the results for pattern 1, it can be seen that as the spark distance is increased, there is more distribution of sparks among the conductive bars as we compare *Figure 74 – Figure 76*. However, in contrast to the previous results, at higher spark distances like 5 cm, both distribution and concentration of sparks can be seen at different spark emitter positions.

`
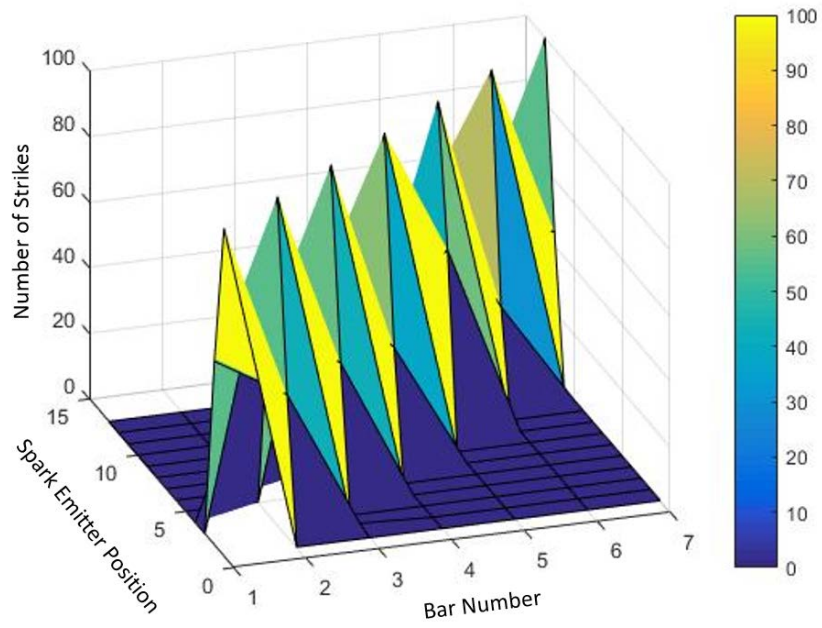
Figure 74 - Frequency distribution analysis for Pattern 2
(Spark distance = 3 cm)
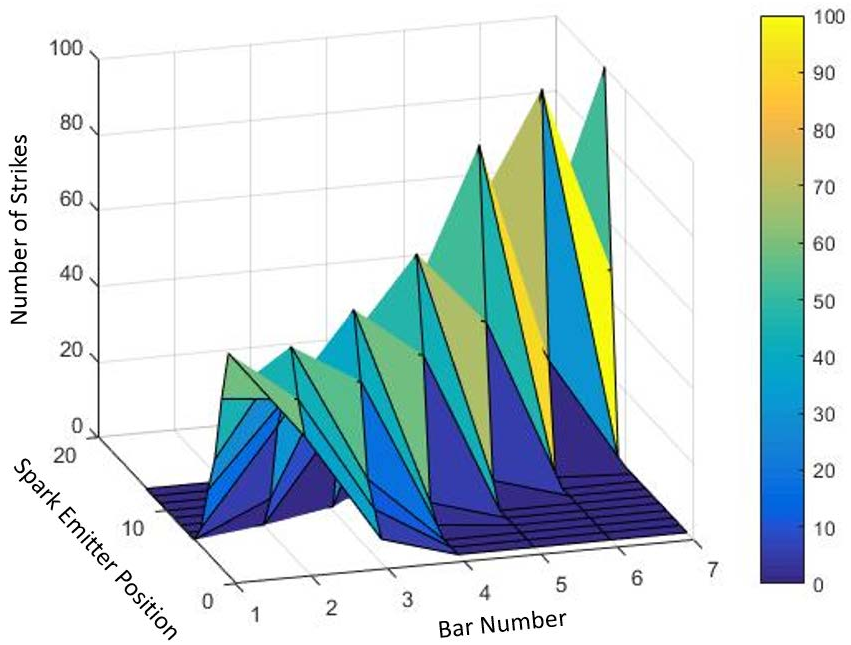
Figure 75 - Frequency distribution analysis for Pattern 2
(Spark distance = 4 cm)
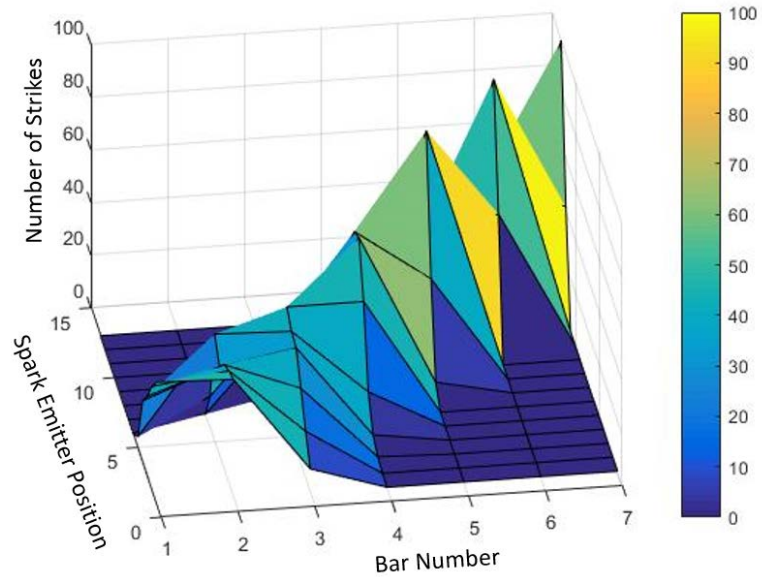
Figure 76 - Frequency distribution for Pattern 2 (Spark distance = 5 cm)

From ***Figure 76***, it can be observed that there is distribution of sparks among adjacent conductive bars at spark emitter positions 1-6 approximately. However, from positions 6 to 13, concentration of sparks is seen at specific single conductive bars. This is because of the higher distance between bars 4, 5, 6 and 7 in this pattern, compared to the distance designed in pattern 1. Therefore, specifically at spark emitter position 7, there is a transition from distributed sparks on multiple bars to concentration of sparks on a single bar. The corresponding 2D plot representing number of strikes at spark emitter position 7 at a spark distance of 5 cm is shown in ***Figure 77***.
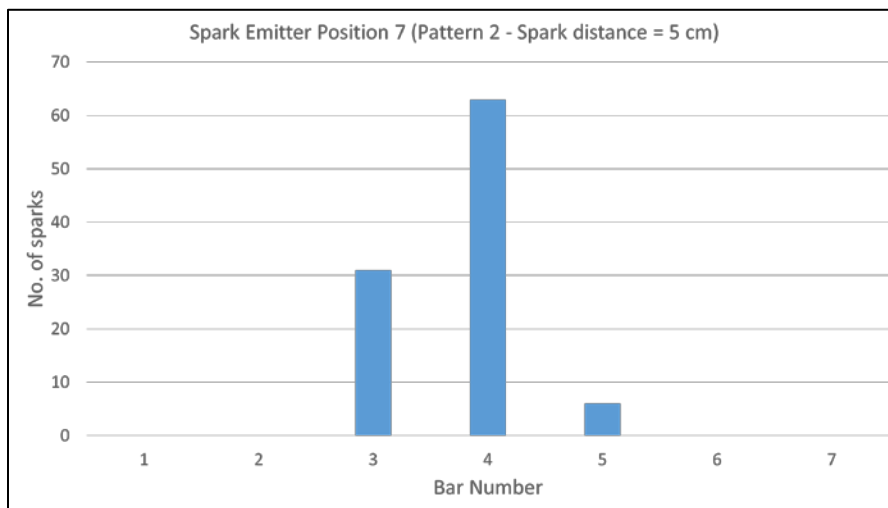
Figure 77 – 2D Frequency distribution of sparks attached when spark emitter is at position 7 (Pattern 2, Spark distance = 5 cm)

78

`

From the Figure, a concentration of sparks can observed at bar number 4 at position 7 of the spark emitter. At this position, the emitter is directly above bar 4. In subsequent positions where spark emitters are placed directly above conductive bars (positions 9, 11 and 13), almost all the sparks are seen to attach to the bars right beneath them. Conversely, when the spark emitter is placed directly over bars 1, 2 and 3 (spark emitter positions 1, 3 and 5), the sparks are much more distributed among the different conductive bars.

Therefore, as mentioned earlier, since both trends (distribution of sparks and concentration of sparks) are being seen for test runs of same spark distance, dependence of results on the spark distance was eliminated in results obtained for the spark distance for 5 cm.

An interesting observation from the experimental runs was the propagation of surface flashovers as seen in **Figure 78**. When the spark emitter was placed close to the polymer surface but comparatively farther from any of the conductive patterns, the sparks would attach to the surface of the polymer, and travel on the surface towards the nearest conductor. Since the current used here was extremely low, there was no permanent damage caused on the polymer surface due to this phenomenon. However, in the case of real lightning, this could potentially cause breakdown of the polymer material causing blade damage.

Figure 78 - Example of surface flashover seen in Pattern 1

The propagation of sparks in these scenarios is interesting to observe. It follows a path towards the nearest conductor, even by propagating on a non-conducting surface. If there was another conductive bar or wire closer to the electrode, the spark would have attached to that as was observed in other test runs. Correlating this observation to actual lightning scenario, this suggests that the presence of a network of conductors might be of

more importance than having a concentrated receptor point on the blade surface. This would ensure that no matter how the lightning gets propagated towards the blade, a well-designed conductive network would be able capture the incoming lightning strike better than a single surface, thus reducing the chances of surface flashovers.

Another important observation from the experimental study was that the sparks hit the conductive bars on the edges almost all the time, even when the spark emitter was placed directly over the bar. This is not apparent in the images or videos recorded during experimental runs due to lack of picture quality, but this is an important observation which inspired design changes to the receptors for the current study, which will be discussed further in section 5.3.

5.2 Comsol simulation results for Experimental Setup

FEM models were created for each of the test runs. Electric field was calculated on the entire surface of the PCB board using Comsol Mulitphysics. As expected, a concentration of electric field was observed on the edges of the conductive bars as can be observed in *Figure 79*. Electric field contour plots of the entire PCB surface was created for each experimental test run. In addition, to obtain quantitative data, the electric field along each of the conductive bar edges were also collected for each experimental run.

Figure 80 shows a 2D graph representing electric field along the length of conductive bars when the spark emitter is placed at position 1, for pattern 2 at a spark distance of 1 cm. B1_E1 and B1_E2 represents the two edges of bar number 1, and similarly B2_E1 and B2_E2 represents the same for bar number 2. For each position of the spark emitter, similar graphs have been made for adjacent conductive bars, to show the difference in electric field between them.

As expected the peak electric field for different spark distances were different, but as mentioned earlier, the aim of this experiment was to correlate the difference in electric field between adjacent conductive bars to spark attachment. As such, the absolute values of peak electric field was not given importance in this study.

It can be seen from *Figure 79* and *Figure 80* that the highest static electric field is produced at the top and bottom ends of the conductive bars (bar lengths 0 and 5000 mil in *Figure 80*). However, the corresponding spark attachments as observed in section 5.1 shows that all the sparks attach to the edges around the center of the bar (within 2000-3000 mil in *Figure 80*).
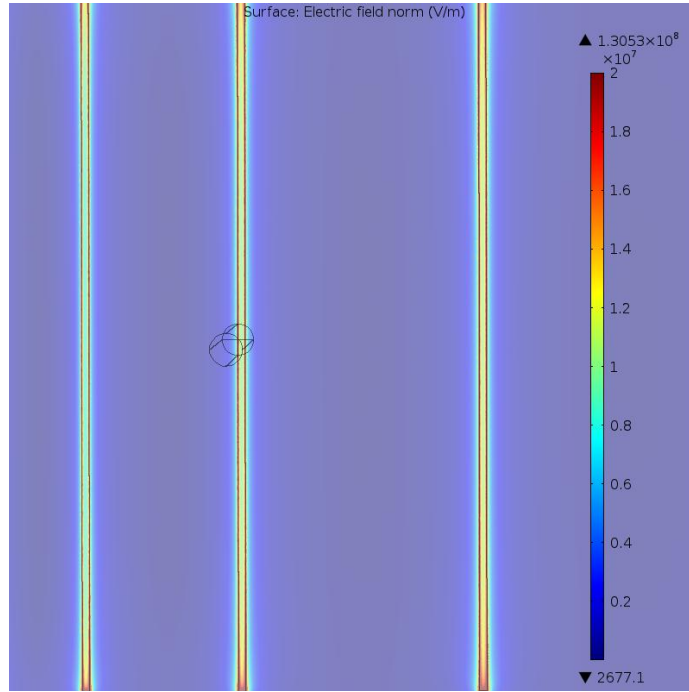
Figure 79 - Surface contour plot for Electric field at spark emitter position 7
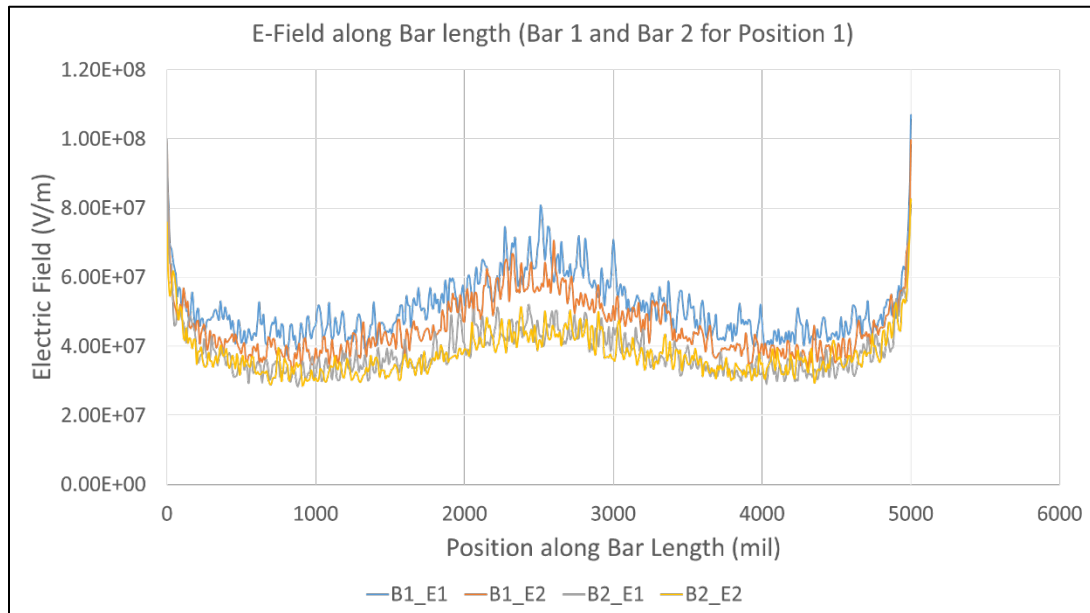*(Pattern 2 at spark distance = 5 cm)*

Figure 80 - Electric Field vs Bar length plot for spark emitter position 1
(Pattern 2 at spark distance = 1 cm)

`

This signifies that the point of highest electric field developed around the conductor need not be the most probable point of spark attachment. Even though there is significantly higher electric field at the top and bottom edges, the spark does not attach to those points. Similar results were observed for all other comparisons of electric field and experimental data.

For further observations regarding electric field, these peaks at the top and bottom were ignored and only the field values around the center of the bar were considered, since most of the electric sparks attached to these regions during experimental study. Electric field results as shown in *Figure 80* were collected for each test run, and the average electric field from bar length 2000 mil to 3000 mil was found for each bar under consideration. For example in *Figure 80*, there are two bars under consideration – Bars B1 and B2. Since most of the spark attachment occurs in the mid-section of the bar, a corresponding average electric field was calculated for both B1 and B2 separately for the section between 2000 and 3000 mils.

Therefore, two distinct values of electric field was obtained for both the bars under consideration, and then compared by dividing average electric field of the first bar with the second, to find the factor of difference between the two. This was done in cases where the spark emitter was placed in between two adjacent conductors. When the emitter was placed directly above the conductive bars, average electric field values of the two adjacent bars were compared with the center bar, and the corresponding factor of difference was calculated. *Table 5* shows the factors of difference between adjacent conductors when the spark emitter is placed in between them.

Table 5 - Factors of difference of Electric field between adjacent conductive bars when spark emitter is placed in between conductors (Pattern 1)

Pattern_1	H_1cm	H_3cm	H_4cm
P_1	1.23	1.18	1.2
P_2	1.22	1.22	1.18
P_4	0.973	0.997	0.988
P_6	0.939	0.957	0.968
P_8	0.921	0.935	0.938
P_10	0.913	0.937	0.937
P_12	0.904	0.899	0.898
P_13	0.817	0.862	0.878

`

P_1, P_2, P_4 etc. represent the spark emitter positions and H_1cm, H_3cm and H_5cm represent spark distances of 1, 3 and 5 cm respectively. When values of these factors exceed 1.0, it means that the conductive bar on the left side of the spark emitter exceeds the one on the right side by the factor value. Similarly, when the factor is less than 1.0, it means that the electric field on the left side bar is less than that on the right side bar by that particular factor. For example, in **Table 5**, for position P_6 at H_1cm spark distance, the factor of 0.939 indicates that the average electric field for Bar number 3 (bar on the left side of position P_6 according to **Figure 62**) is 0.939 times the average electric field for bar number 4 (bar on the right side of position P_6). Similarly, data has been represented for all subsequent spark emitter positions.

Table 6 - Factors of difference of Electric field between adjacent conductive bars when spark emitter is placed directly above conductor (Pattern 1)

Pattern_1	H_1cm		H_3cm		H_5cm	
	Diff_1	Diff_2	Diff_1	Diff_2	Diff_1	Diff_2
P_3	1.13	1.02	1.18	0.993	1.19	1
P_5	0.94	1.02	0.994	0.977	0.988	0.983
P_7	0.945	0.982	0.978	0.938	0.969	0.945
P_9	0.878	1.01	0.925	0.956	0.929	0.953
P_11	0.853	0.992	0.916	0.905	0.925	0.911

For cases where the emitter is placed directly above the conductive bars, average electric fields for all three bars (on the Left, Center and Right of the spark emitter) were calculated. Then similar to the previously explained method, the left hand bar is compared to the center bar – and the corresponding factor of difference is denoted by Diff_1 in **Table 6**. Similarly, the center bar is compared with the bar on the right – and the corresponding difference factor is denoted by Diff_2.

From experimental results, it was observed that as the spark distance was increased, there was more distribution of sparks among conductors, showing that as height of electrode from the surface was increased, the difference in the ability of adjacent conductors to attract the spark towards it reduced. The objective of the Comsol models was to correlate this phenomenon with a reduction in difference of electric field among the same adjacent conductive bars.

The closer the difference factors are to 1.0, the closer the average electric fields of the adjacent bars are to one another. Looking at the transition of the difference factors from H_1cm to H_5cm in Table 5.1, it can be observed that the difference in electric field reduced very slightly for each spark emitter position (since the difference factor is slightly closer to 1.0). Similarly, in Table 5.2, the values of Diff_1 and Diff_2 for each of the positions is seen to be closer to 1, as the spark distance is increased from 1 cm to 5 cm.

`

However, the difference noted for all tests in pattern 1 are extremely minute and not significant enough to extract any notable inference from the result. **Table 7** and **Table 8** shows the difference factors for the same tests conducted on pattern number 2.

Table 7 - Factors of difference of Electric field between adjacent conductive bars when spark emitter is placed in between conductors (Pattern 2)

Pattern_2	H_1cm	H_3cm	H_4cm
P_1	1.36	1.27	1.28
P_2	1.15	1.22	1.26
P_4	0.961	0.942	0.953
P_6	0.892	0.87	0.849
P_8	0.889	0.872	0.864
P_10	0.908	0.891	0.875
P_12	0.864	0.852	0.857
P_13	0.542	0.685	0.738

Table 8 - Factors of difference of Electric field between adjacent conductive bars when spark emitter is placed directly above conductor (Pattern 2)

Pattern_1	H_1cm		H_3cm		H_5cm	
	Diff_1	Diff_2	Diff_1	Diff_2	Diff_1	Diff_2
P_3	1	1.21	1.2	0.998	1.24	0.976
P_5	0.724	1.29	0.903	0.959	0.935	0.903
P_7	0.614	1.44	0.778	1.04	0.822	0.925
P_9	0.559	1.55	0.737	1.11	0.792	0.99
P_11	0.54	1.47	0.723	1.08	0.794	0.96

From the experimental results discussed in section 5.1, it was found that tests runs done at a spark distance of 5 cm was a point of interest. At spark emitter position 7, a transition from distribution of sparks to concentration of sparks was found. The corresponding difference factors between the conductive bars was found to be 0.822 and 0.925 for the conductive bars on the left and right side of the spark emitter respectively in comparison with the bar in the center. This is corresponding to the scenario when the spark emitter is placed directly above bar number 4. It is observed that even though the difference

factor between the conductive bar in the center and the one on the right side is only 0.925 (electric field close to each other), sparks tend to attach to conductive bar in the center. Moreover, for position P_9, when the spark emitter is directly over bar number 5, the electric fields around the center bar and the bar on the right side is almost the same (difference factor is 0.99), however almost all the sparks tend to attach to the conductive bar in the center.

Thus, from the results shown above, it can be inferred that a direct correlation between electric field and probability of lightning attachment is not possible and inaccurate. A concentration of electric fields was observed around the conductive bars at the two ends – bars B1 and B7, and therefore, for different spark emitter positions, highest peak electric field was not found around the conductive bar right underneath the spark emitter as expected, but around bars closer to the ends of the pattern.

Table 8 shows an example of this phenomenon illustrated, as the difference factor Diff_1 is 1.24 corresponding to position P_3 at spark distance H_5cm. This means that even though the spark emitter is directly above bar number 2 (position P_3), the conductive bar number 1 has a significantly higher electric field which is 1.24 times the electric field of bar number 2. This is due to the concentration of electric field at conductive bars at the ends of the pattern. The reasons for both the concentration of electric fields around B1 and B2, and the possible reason sparks do not necessarily attach to the point of highest electric field will be discussed further in the next section.

5.3 Inference from results

It was found that there is a concentration of electric field in bars B1 and B7 (bars at the left and right ends) of the pattern for the both pattern designs. *Figure 81* shows a pictorial representation for the propagation of electric field lines when a high voltage electrode is brought near multiple conductors like what is done in the current study. Since electric field lines are attracted to grounded conductors, they tend to get attached to the surface of the conductive bars. However, the conductive bar at the end of the pattern will attract a lot more field lines as seen in the left most bar in *Figure 81*. This is due to the absence of more conductors placed after the left most conductive bar for the electric field lines to attach to. Therefore there is a concentration of electric field found on conductors placed at the end of the pattern. Hence, the reason for a significantly higher electric field at conductive bar number 1, even when the spark emitter was place directly over bar number 2 as pointed out in section 5.2.

It was also found during experimental analysis, that the point of highest electric field around a conductive surface need not necessarily be the point of most probable spark attachment. This is because streamer formation is a dynamic process, where the static electric field around the propagating spark (and conductors in the vicinity) is under constant change during spark propagation. This means that highest electric field calculated at a static initial condition applies only to when the spark initiates, and as it propagates further, the dynamic nature of the spark has to be taken into account to accurately model spark attachment. The same theory would apply to actual lightning. Even though highest electric

`

field is used currently in the industry to find points that have high possibilities of attracting lightning, to effectively model the path taken by the spark to attach to receptors, a dynamic model (which changes with respect to time) is required (Garolera et. al., 2013). Thus, as a future extension of this project, incorporating this dynamic feature into the current Comsol model would be ideal.
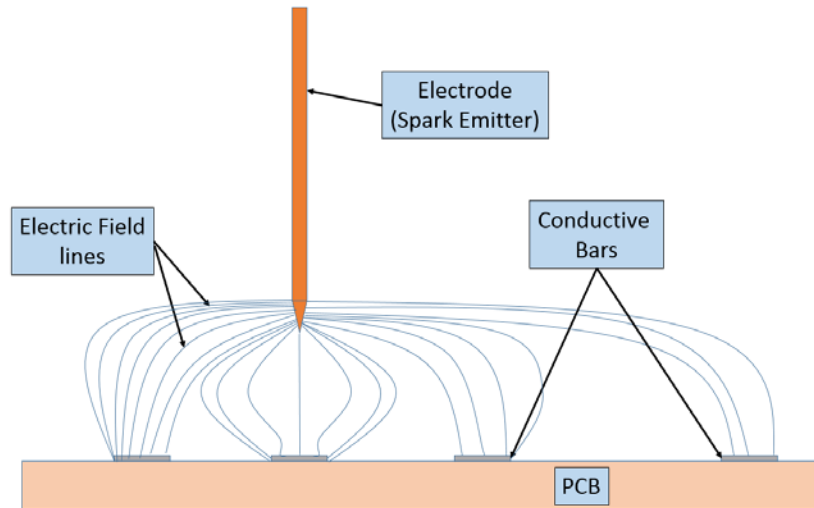

Figure 81 - Concentration of Electric field lines in conductors at end of patterns

This would help in getting an accurate correlation between electric field and probability of lightning attachment as well, which was intended for this study. It could also help in observing how the lightning streamers might actually propagate from the cloud to ground. A full scale model depicting the propagation of lightning streamers has never been developed so far, and as such, it would be an excellent method of studying how changing the receptor shapes really affect lightning attachment.

A simplistic 2D dynamic model was made by researchers to model the dynamic nature of spark attachment, which replicates the path followed by a spark during propagation towards spark attachment (Garolera et. al., 2013). Dynamic principles used in this model could be incorporated in the models used for current study, thus possibly creating a dynamic representation of full scale lightning propagation, and corresponding lightning attachment on wind turbine blades.

Figure 82 shows as example of the path followed by a spark as it propagates towards a grounded conductor. It can be seen that a direct path is not followed here. In fact, for higher spark distances, the spark almost always follows an indirect path towards ground, showing that there are other factors involved in its propagation, rather than just static electric field calculated before the spark starts to travel towards ground.
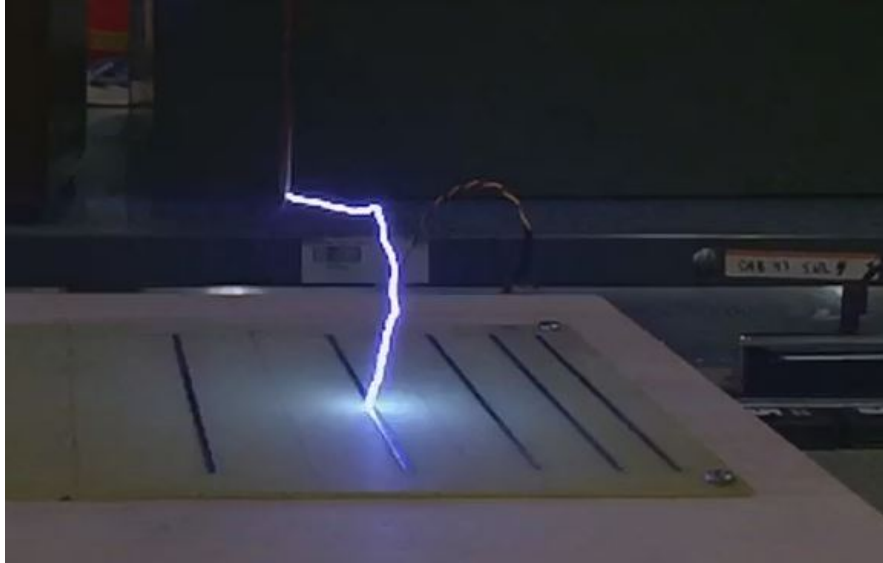
`

Figure 82 - Example of path taken by spark towards grounded conductor in current study

(Gallimberti, 2002) describes in detail the physics involved in streamer propagation. He explains that when high voltage is applied to an electrode, the highest electric field at that instant is at the electrode surface, and as such, negative ions in the air approach these high field surfaces. In the process, free electrons are produced through collision. At a high enough electric field, an electron avalanche is observed, where a large number of electrons get accelerated due to high electric field. This process results in what is called a corona discharge at the end of the electrode. When the free electrons are able to successfully ionize surrounding molecules through collision, the discharge of electrons through a channel (lightning channel) is observed.

Figure 83 depicts a schematic Figure showing the development of an electron avalanche near an electrode surface. During an electron avalanche, there is a rapid movement of electrons towards the electrode surface. A corresponding positive charge is built up, which increases the electric field around the surrounding air. If this built up electric field is high enough, ionization will continue and the streamer will continue to propagate through the formation of new avalanches. These avalanches occur within the actives regions as shown in ***Figure 83***.

Therefore, the fact that streamer formations are a step-by-step process instead of a continuous one is reinforced, and therefore the corresponding electric field FEM models should also incorporate this understanding of lightning physics. The model should ideally consist of multiple active regions, one after the other to depict formation of multiple streamers in a step by step process. Therefore, the change in electric field in surrounding objects will change the direction of streamer propagation, and therefore will provide a more accurate result for where the lightning streamer gets attached.
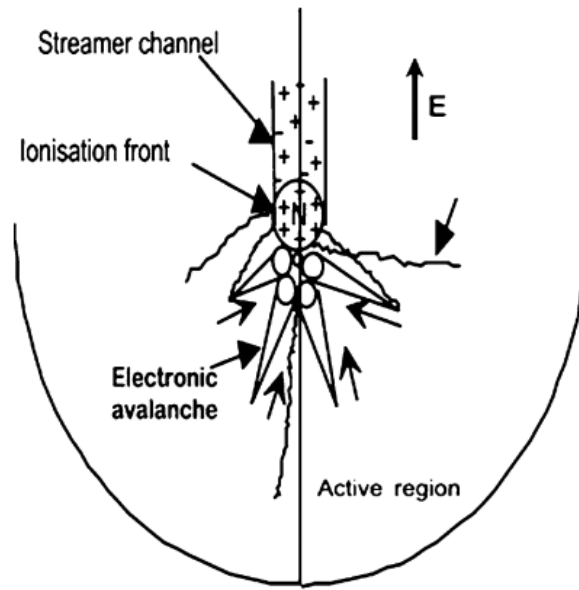
Figure 83 - Electron avalanche and corresponding streamer formation (Gallimberti et. al., 2002)

In addition to the two inferences mentioned above, an important observation from this study was that the sparks always attached to the edges of the conductive bars. This is in accordance with the concentration of electric field observed along the bar edges, as found in the Comsol models. This observation was used to design wireframe receptors which will discussed further in the next chapter.

CHAPTER 6 . NOVEL CONDUCTIVE PATTERNS ON TURBINE BLADE

Based on results obtained from experimental analysis, few inferences were obtained for generating better receptor designs. One of the major observations was that the spark was seen to strike the edges of the conductor in almost all test runs. The other observation gained from literature review is that lightning is attracted to sharp objects. In other words, there is a concentration of electric field that occurs in steep curves (or sharp objects), because of a concentration of charge which occurs at such regions in the presence of a high voltage source. Thus, commonly used lightning receptors in buildings and other general applications use sharp rods and similar shapes for attracting lightning. This is due to the high electric field concentration at the pointy ends of such objects, which attract lightning towards it more effectively.

Using the two observations noted above, a series of possible changes in receptor design has been proposed in this section. The FEM electrostatic model shown in model validation in section 3 was modified to include receptors of different shapes to try and increase the peak electric field obtained at the blade tip, such that the lightning leader would be more inclined to attach to these receptors, reducing the chances of blade damage. In addition, few wireframe receptor designs are also proposed, based on the first observation that sparks tend to strike conductor edges in most cases.

6.1 Diamond Shaped receptors

One of the simplest ways of changing the design to include more edges into the design was to change the circular receptor design to a square (or quadrilateral). *Figure 84* shows examples of the new receptor design being presented here. This design represents a diamond shaped structure with edges pointed towards the leading and trailing edges. Taking reference from the validated Comsol model from section 3, the surface areas for the single round receptors of 0.2 m and 0.3 m radius were obtained from CAD models, and the newly designed diamond shaped receptors have been generated with the same surface areas, such that there can be a direct comparison between the receptors keeping the surface area same. Surface area directly correlates to mass of the receptor used in an actual scenario, and as such, the objective of proposing the new designs is to show an increase in electric field with receptors of same weight as the round receptors in comparison. Surface area for the 0.2 m radius round receptor was found to be 0.127 m^2 and that of the 0.3 m radius round receptor was found to be 0.286 m^2.

A short study was conducted on the diamond shaped receptors to observe how changing its shape would affect the peak electric field generated around the receptor. The angle of top and bottom vertex (let's say vertex angle) of the diamond receptors were parameterized and the peak electric field was obtained for different vertex angles ranging from 90° (Perfect square) to 40°. This study was conducted for 0.127 m^2 and 0.286 m^2 surface areas.

`

Figure 84 - Figure 86 shows contour plots of electric field on the blade tip surface for quadrilateral receptors of different vertex angles with a 0.127 m² surface area. It can be observed that there is a considerable increase in peak electric field when compared to that obtained from the round receptor of 0.2 m radius.
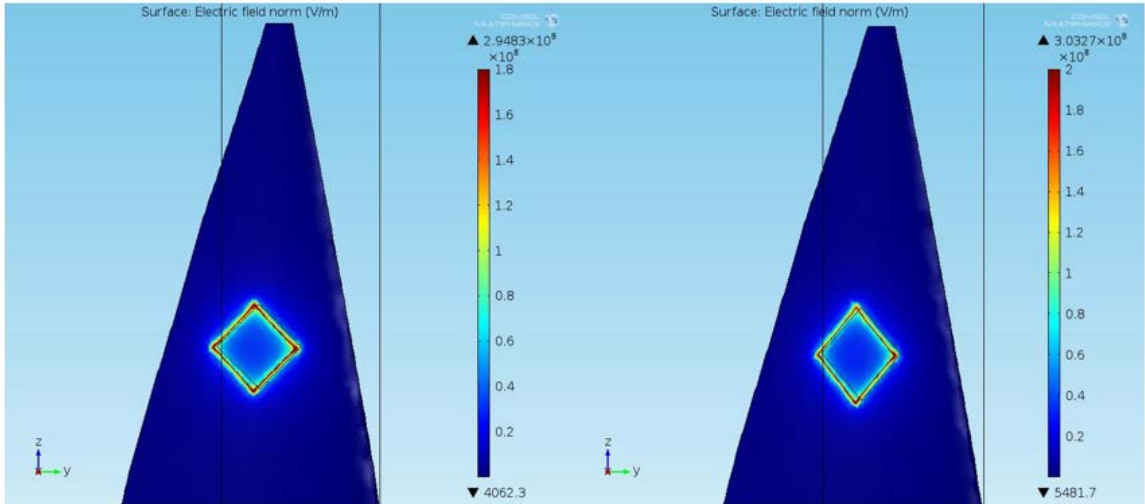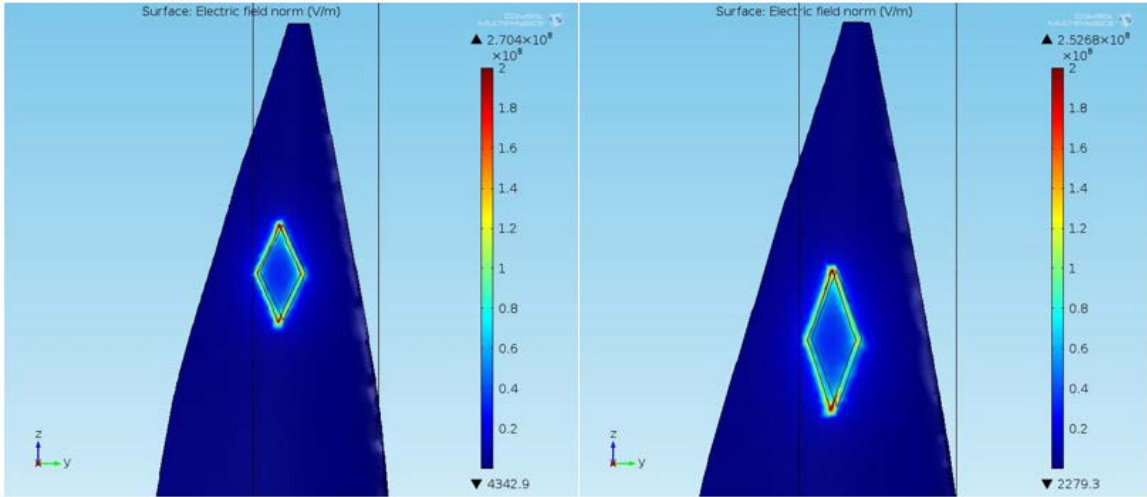

Figure 84 - Left: Quadrilateral receptor with top angle = 90°
Right: Quadrilateral receptor with top angle = 80°
Receptor Surface Area = 0.127 m²
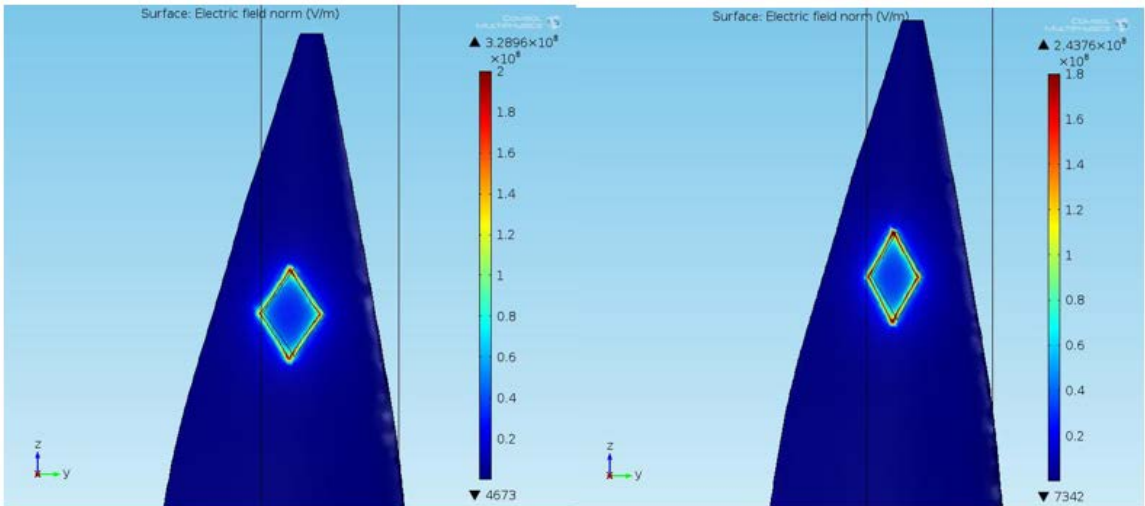
Figure 85 - Left: Quadrilateral receptor with top angle = 70°
Right: Quadrilateral receptor with top angle = 60°
Receptor Surface Area = 0.127 m²

Among all receptor configurations listed in *Figure 84 - Figure 86*, the highest peak field observed is 3.29E+08 V/m at a vertex angle of 70° and the lowest was found to be 2.47E+08 V/m at a vertex angle of 60°. This translates to a 110% and 58% increase respectively in peak electric field when compared to the round receptor with same surface area as shown in *Figure 42*.

Figure 86 - Left: Quadrilateral receptor with top angle = 50°
Right: Quadrilateral receptor with top angle = 40°
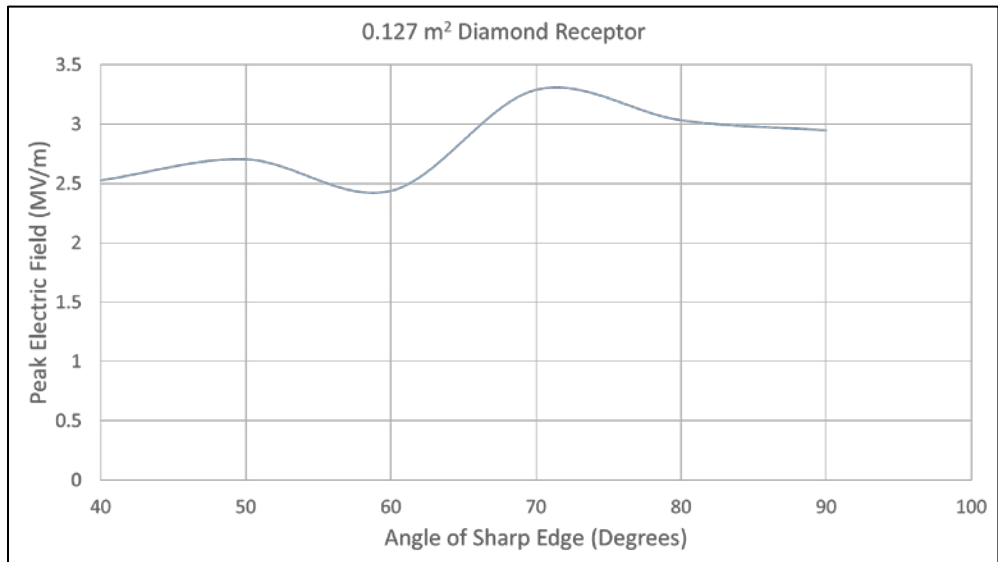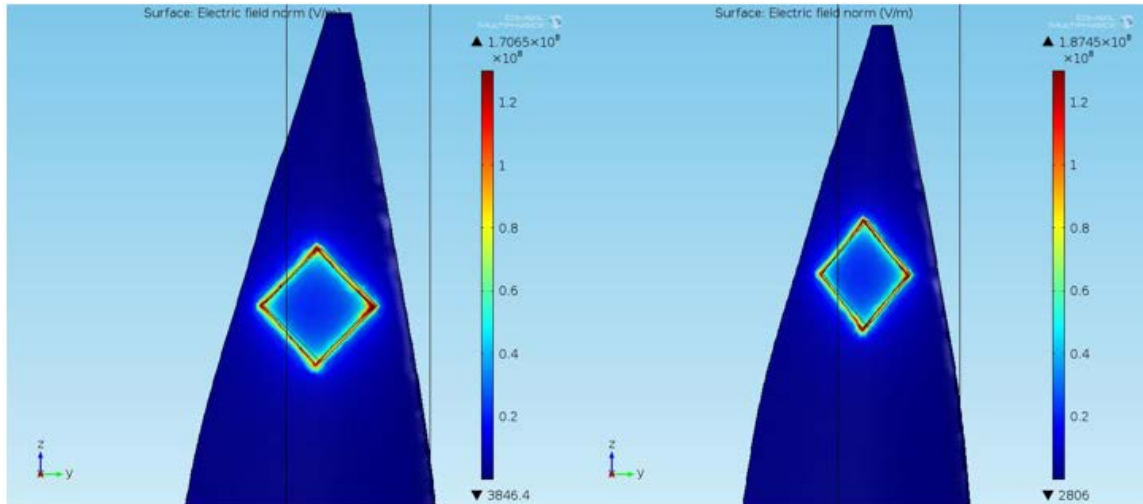*Receptor Surface Area = 0.127 m²*

Figure 87 - Variation of peak electric field with top angle of quadrilateral shaped receptor (Surface area 0.127 m²)

`

The relationship between peak electric fields observed in receptors with 0.127 m² surface area with vertex angles ranging from 90° to 40° is shown in *Figure 87*. The highest and lowest values of peak electric field has been discussed already, however it can be noted that there is no extractable trend being followed by the plot, and as such, the peak electric field would differ for different angles of vertex angles without following a particular trend, however according to electric field literature that has been covered in this study, a sharper edge (vertex) should theoretically have a concentration of electric field.

Even though change electric field increase due to change in vertex angle of the receptor does not follow a specific trend, the peak electric field has been dramatically increased to up to twice what was calculated for the round receptor. Thus, the newly designed diamond receptors would have a better capture efficiency compared to round receptors.

Similar models were made for diamond receptors of 0.286 m² surface area, corresponding to the 0.3 m radius round receptors as seen in *Figure 42*. *Figure 88 – Figure 90* shows the contour plots showing electric field around blade tip regions for different values of vertex angles, like what was done for the previous study.

Figure 88 - Left: Quadrilateral receptor with top angle = 90°
Right: Quadrilateral receptor with top angle = 80°
Receptor Surface Area = 0.286 m²

`
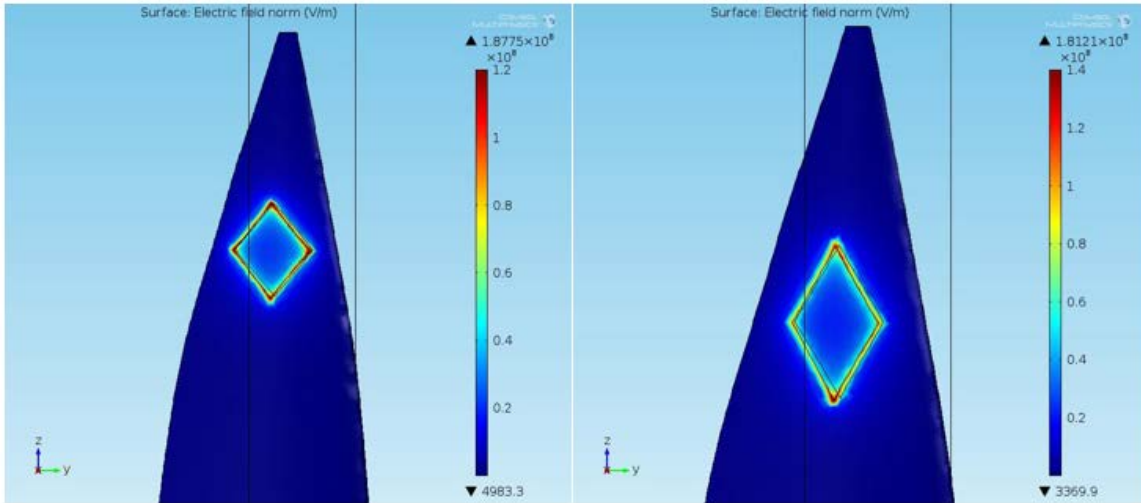
Figure 89 - Left: Quadrilateral receptor with top angle = 70°
Right: Quadrilateral receptor with top angle = 60°
Receptor Surface Area = 0.286 m²
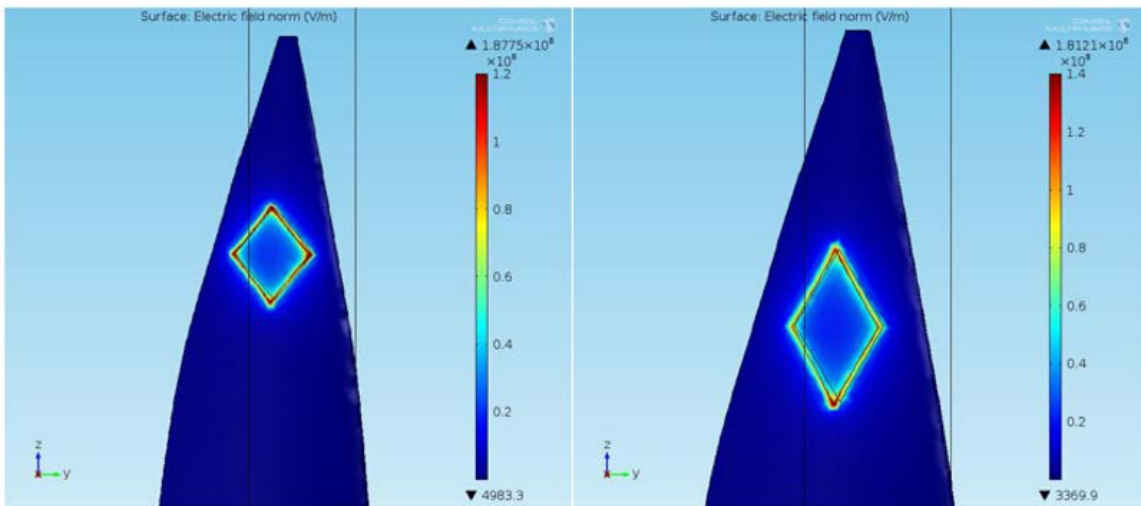
Figure 90 - Left: Quadrilateral receptor with top angle = 50°
Right: Quadrilateral receptor with top angle = 40°
Receptor Surface Area = 0.286 m²

The corresponding 2D plot for change in electric field with respect to vertex angle is shown in ***Figure 91***. The highest peak electric field attained was 1.935E+08 V/m at a vertex angle of 50° and the lowest attained was 1.7E+08 V/m at a vertex angle of 90°. This corresponds to a 66% and 46% increase in peak electric field respectively, when compared to the 0.3 m radius round receptor.
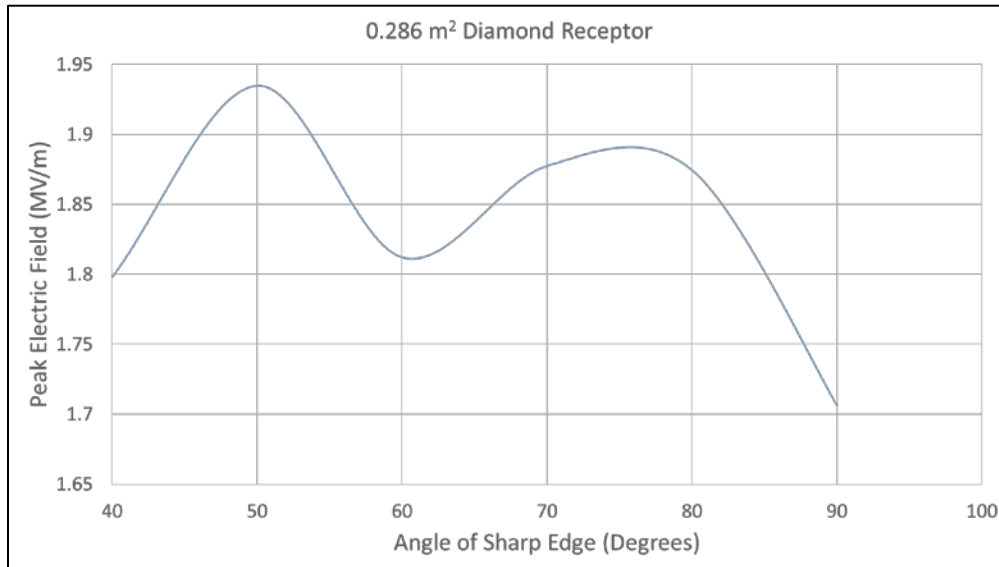
`

Figure 91 - Variation of peak electric field with top angle of quadrilateral shaped receptor (Surface area 0.286 m²)

Similar to *Figure 87*, it can be observed that there is not much variation (or detectable trend) in the peak electric field, however, it is evident that incorporation of sharp edges through a diamond shape for the same receptor surface area has shown an increase in peak electric field on the blade surface.

6.2 Wireframe receptors

One of the major observations from experimental analysis was that electric sparks attached to edges of the conductors in almost all cases. Taking inspiration from this observation, a set of wireframe receptors were designed. Lightning receptors for these patterns are designed as conductive lines with different spacing or different orientations, as shown in *Figure 92* and *Figure 93* respectively. The conductive lines represent ingrained conductive paths, which could be similar to conductive wires on the turbine surface, which runs as a conductive network on the surface of the blade. Similar to previous receptor designs, these pathways would be connected to down-conductor within the blade cross-sections which runs through the blade cavity towards ground.

Edges on blade surfaces were modelled into the turbine CAD models, and then assigned a conductive edge boundary condition in Comsol to represent the conductive pathways. Modelling a wire of minute thickness would be extremely taxing for the current model, which is inherently using multi-scale meshing operations, due to large differences in geometry dimensions. Hence, thickness of the conductive pathways are not assumed for these models, and the corresponding conductive paths are represented by wireframe lines in Comsol.

`

Two different types of wireframe designs were made – One using a horizontal line across the blade connected to perpendicularly vertical lines as shown in **Figure 92**. The other design consists of a center point on the blade surface, from which conductive wires are arranged in different angles as seen in **Figure 93**. Coarse and fine patterns were modelled for both the design types mentioned above.
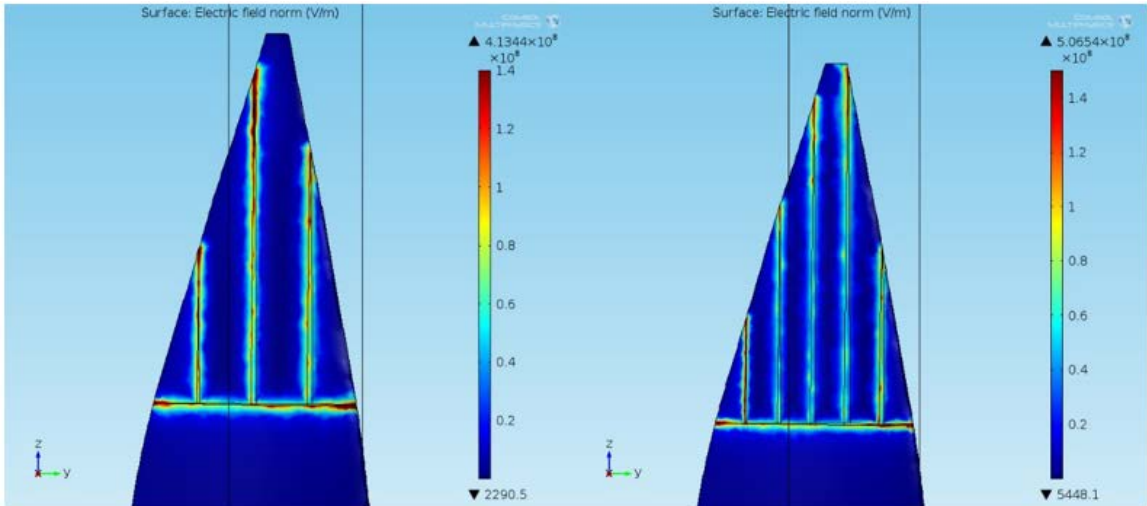

Figure 92 - Perpendicular wireframe receptors
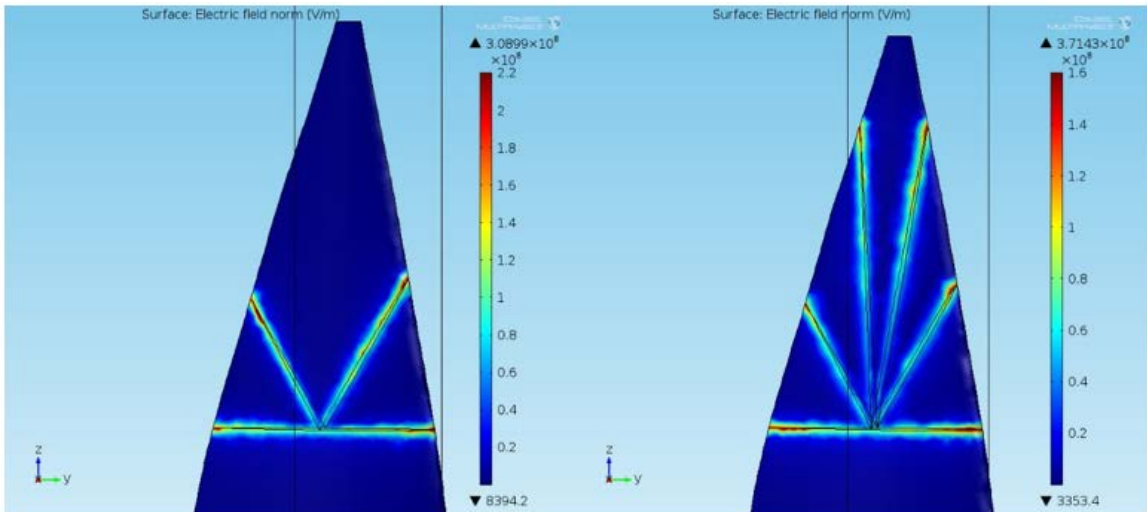*Left: Coarse pattern; Right: Fine pattern*

Figure 93 - Angled wireframe receptors
Left: Coarse pattern; Right: Fine pattern

Figure 92 shows both the coarse and fine pattern models for the perpendicular wireframe receptors. The coarse type model consisted of three vertical conductive lines,

whereas the fine model consisted of five lines with equal spacing. It can be seen that peak electric field is 4.13E+08 V/m and 4.065E+08 V/m for the coarse type and fine type models respectively. The highest peak electric field found among all the models considered for model validation in section 3 was 1.56E+08 V/m for the 0.2 m radius round receptor as mentioned before. Comparing to current values, the peak electric field for the coarse perpendicular wireframe pattern is 2.65 times that of the round receptor and similarly, peak electric field of the fine perpendicular wireframe pattern is 3.24 times that of the round receptor.

Similar to results of the perpendicular wireframe patterns, coarse and fine pattern models were created for the angled wireframe receptors as well, as can be seen in *Figure 93*. The peak electric fields obtained for the coarse and fine pattern is 3.08E+08 V/m and 3.714E+08 V/m respectively. In comparison to maximum peak electric field found in round receptors (maximum electric field = 1.56E+08 V/m), the peak electric field for the coarse and fine pattern for current design is 1.97 times and 2.37 times the peak electric field for the round receptors respectively.

Correlating these increases in peak electric fields to their increase in performance for attracting lightning in the real-world scenario is possible only through experimental testing under conditions close to that faced during an actual lightning strike. However, from results obtained from FEM analysis of the new designs implemented here, it can be argued that peak electric field around the blade tip region has definitely been significantly increased compared to previous designs, and thus the capture efficiency of the new designs could potentially be higher, which would have to be proven with physical experimentation.

When considering physical testing, one major area of interest is the adhesives used to attach receptors to the blade surface during high voltage tests. Improper adhesives or lack of proper insulation could result in damage to the blade even for standard receptor designs, and as such, selection of adhesives and proper insulation should be taken care of while preparing for high voltage testing.

CHAPTER 7 . CONCLUSION

The electrostatic effects of changing lightning receptor designs on wind turbine blades was observed through finite element analysis, using the electrostatics module in Comsol Multiphysics software. From literature and lightning physics known to us currently, it is evident that sharp conductive objects attract lightning towards them due to the concentration of electric field on these edges. Using inspiration from this theory, the standard receptor shape used in wind turbines was changed in this study, and the corresponding peak electric field was observed to be much higher than that of the standard round receptors used on turbine blades currently.

In addition, high voltage tests was done on conductive patterns to gain an insight into the behavior of spark propagation. Observations from this experimental analysis was used to make changes in receptor designs, with potentially higher capabilities of attracting lightning. In addition, the limitations of current computational models were understood, and possible simulation techniques for dynamic analysis of electric field were also been discussed. The following conclusions were made from this study:

1. From experimental analysis, it was found that under high voltage conditions, the sparks in almost all cases, attached to the edges of conductive bars. The corresponding FEM simulation agrees with this observation, as a concentration of electric field is found on conductor edges. This suggests that receptors with considerable surface areas are not ideal for lightning capture, and receptors should be modelled to be a network of conductive paths rather than concentrated points of attraction.

2. Including sharp edges to receptor design (like changing the round receptor to a diamond shape) showed a significant increase in peak electric field acting on the blade surface – of up to 110% increase when compared to round receptors. However, changing the internal angle of the newly introduced diamond receptors does not show considerable change in peak electric field acting on the blade surface.

3. Introduction of wireframe receptors shows a significant increase in peak electric field – with an increase of up to 3.24 times the peak electric field as compared to round receptors. These new receptor designs also cover a wider region of the blade, hence potentially providing much better capture efficiency to the blade, when compared to round or diamond shaped receptors.

4. When a group of conductors are placed together in the vicinity of a high voltage electrode, a concentration of electric field is found on the conductors placed at the far ends.

5. A concentration of static electric field on a conductive surface does not necessarily mean that sparks (or lightning) is most attracted to that point. It was found that lightning was attracted to conductive regions close to the high voltage electrode, even though the peak electric field was found at different regions.

`

A possible reason for the failure to correlate electric field to probability of lightning attachment is suggested to be the difference between the dynamic nature of spark propagation and the static nature of Comsol simulations being generated. Once of the future extensions of this project could be development of an iterative FEM model, which simulates the dynamic nature of lightning streamers, by repeatedly changing the Comsol model geometry, to show how the spark propagates towards the point of lightning attachment, and changes the corresponding electric field around conductors.

In addition, to validate the newly proposed receptor designs, high voltage tests in specialized lightning labs with capabilities of 10 MV and above would be beneficial to compare how it attracts lightning compared to standard receptors. A similar test procedure to what was followed in the current study could be followed, by changing the electrode position for each test run. The corresponding spark attachment on the new receptors could be directly compared with those of the round receptor to verify if is better capture efficiency is obtained.

REFERENCES

Arantegui, R. L., & Jäger-Waldau, A. (2017). Photovoltaics and wind status in the European Union after the Paris Agreement. Renewable and Sustainable Energy Reviews. Eriksson, A. J. (1979). The lightning ground flash: an engineering study

Arinaga, S., Inoue, K., & Matsushita, T. (2006). Experimental study for wind turbine blades lightning protection. development, 4, 5.

Carey, W. J., & Mayes, J. R. (2002, June). Marx generator design and performance. In *Power Modulator Symposium, 2002 and 2002 High-Voltage Workshop. Conference Record of the Twenty-Fifth International* (pp. 625-628). IEEE.

Cooray, V., Rakov, V., & Theethayi, N. (2007). The lightning striking distance—Revisited. Journal of Electrostatics, 65(5), 296-306.

EWEA-Annual-Statistics-2015

Gagné, M., & Therriault, D. (2014). Lightning strike protection of composites. *Progress in Aerospace Sciences, 64*, 1-16.

Gallimberti, I., Bacchiega, G., Bondiou-Clergerie, A., & Lalande, P. (2002). Fundamental processes in long air gap discharges. *Comptes Rendus Physique, 3*(10), 1335-1359.

Garolera, A. C., Holbøll, J., & Mieritz, C. F. (2013). Modelling of lightning streamer formation and propagation in wind turbine blades. In *2013 International Conference on Lightning and Static Electricity.*

Garolera, A. C., Madsen, S. F., Nissim, M., Myers, J. D., & Holboell, J. (2016). Lightning Damage to Wind Turbine Blades From Wind Farms in the US. IEEE Transactions on Power Delivery, 31(3), 1043-1049.

Hernández, Y. M., Castro, A., Kindersberger, J., Lewke, B., DiBella, J., Hardison, R., & Stolper, R. (2010, September). A first approach in the modelling of failures in rotor blades caused by lightning strikes. In Lightning Protection (ICLP), 2010 30th International Conference on (pp. 1-8). IEEE.

Jonkman, J., Butterfield, S., Musial, W., & Scott, G. (2009). *Definition of a 5-MW reference wind turbine for offshore system development* (No. NREL/TP-500-38060). National Renewable Energy Laboratory (NREL), Golden, CO..

Karegar, H. K., & Bagherian, H. (2012). Effects of location, size and number of wind turbine receptors on blade lightning protection. Dianli Xitong Zidonghua (Automation of Electric Power Systems), 36(8), 122-127.

`

Kim, J. "Radar Absorbing Structure with Periodic Pattern Surface for Wind Blade." Session 2P9: 465

Krehbiel, P. R. (1986). The electrical structure of thunderstorms. *The Earth's electrical environment*, 90-113.
Lewke, B., Kramer, S., Méndez Hernández, Y., & Kindersberger, J. (2007). Conductive surface layer on wind turbine blade as lightning protection system. *Proceedings of Windpower, Los Angeles*, 3-6.

Lo, P. M. (2008). A simplified model for lightning exposure of wind turbines (Doctoral dissertation, McGill University).

Lorentzou, M. I., Hatziargyriou, N. D., & Cotton, I. (2004). Key issues in lightning protection of wind turbines. WSEAS Transactions on Circuits and Systems, 3(5), 1408-1414.

Marshall, T. C., & Winn, W. P. (1982). Measurements of charged precipitation in a New Mexico thunderstorm: Lower positive charge centers. *Journal of Geophysical Research: Oceans*, *87*(C9), 7141-7157.

Moore, C. B., Aulich, G. D., & Rison, W. (2000). Measurements of lightning rod responses to nearby strikes. *Geophysical research letters*, *27*(10), 1487-1490.

Peesapati, V., Cotton, I., Sorensen, T., Krogh, T., & Kokkinos, N. (2011). Lightning protection of wind turbines–a comparison of measured data with required protection levels. *IET renewable power generation*, *5*(1), 48-57.

Rachidi, F., Rubinstein, M., Montanya, J., Bermudez, J. L., Sola, R. R., Sola, G., & Korovkin, N. (2008). A review of current issues in lightning protection of new-generation wind-turbine blades. *IEEE Transactions on Industrial Electronics*, *55*(6), 2489-2496.

Sorensen, T., Jensen, F. V., Raben, N., Lykkegaard, J., & Saxov, J. (2001, June). Lightning protection for offshore wind turbines. In *Electricity Distribution, 2001. Part 1: Contributions. CIRED. 16th International Conference and Exhibition on (IEE Conf. Publ No. 482)* (Vol. 4, pp. 5-pp). IET.

Sorensen, T. S., Plumer, J. A., Montanyà, J., Krogh, T. H., Hermoso, B., Birkl, J., ... & Brown, D. (2008, June). The update of IEC 61400-24 lightning protection of wind turbines. In *29th International Conference on Lightning Protection of Wind Turbines*.

Sul, P. (2015). Concept of a modern method of determining lightning protection zones based on the field computational method. Przegląd Elektrotechniczny, 91(7), 27-29.

Wang, Y. (2016). *Modeling of lightning-induced thermal ablation damage in anisotropic composite materials and its application to wind turbine blades*(Doctoral dissertation, The University of Iowa).

`

Wang, Y., & Hu, W. (2017). Investigation of the Effects of Receptors on the Lightning Strike Protection of Wind Turbine Blades. IEEE Transactions on Electromagnetic Compatibility, 59(4), 1180-1187.

Wen, X., Qu, L., Wang, Y., Chen, X., Lan, L., Si, T., & Xu, J. (2016). Effect of wind turbine blade rotation on triggering lightning: An experimental study. Energies, 9(12), 1029.

Wessels, H. R. A. (2002). *Lightning damage of OWECS part1: parameters relevant for cost modelling*. ECN-C-02-053

Yokoyama, S. (2013). Lightning protection of wind turbine blades. *Electric Power Systems Research*, *94*, 3-9.

Yokoyama, S., Honjo, N., Yasuda, Y., & Yamamoto, K. (2014, October). Causes of wind turbine blade damages due to lightning and future research target to get better protection measures. In Lightning Protection (ICLP), 2014 International Conference o (pp. 823-830). IEEE.

`

Similar to the comparisons done for the blade models with the 0.3 m and 0.2 m radius single round receptors, the same analysis was done for a model with two receptors as shown in **Figure 94**. The difference in peak electric field was calculated to be 34% among the two models. The rest of the electric field behavior was observed to be similar to that of the reference model, as seen in the contour plot.
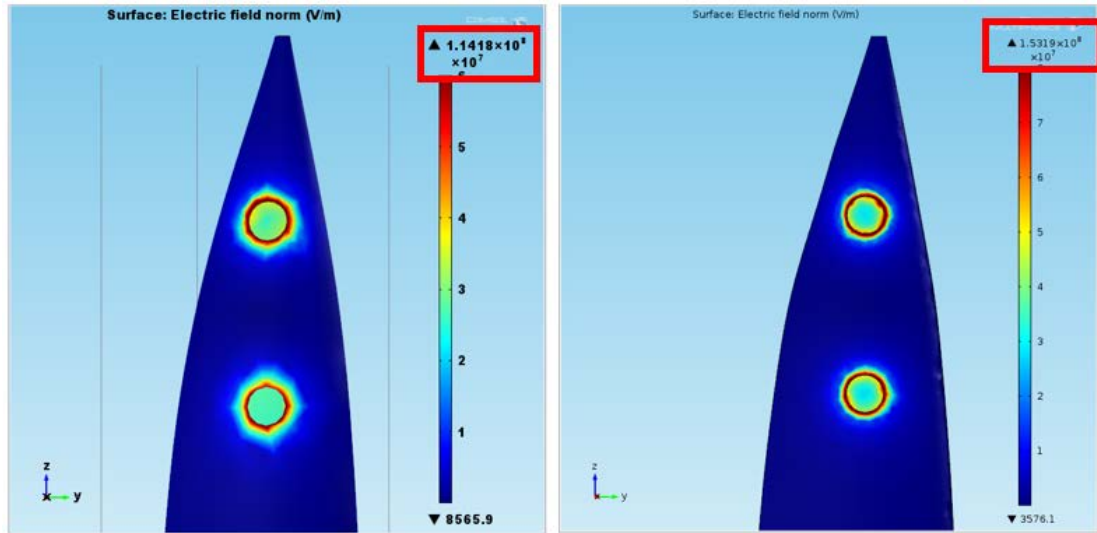

Figure 94 - Comparison of peak Electric field in: Left - Reference model (Wang et. al, 2017); Right - Current model (Double 0.2 m round receptor)
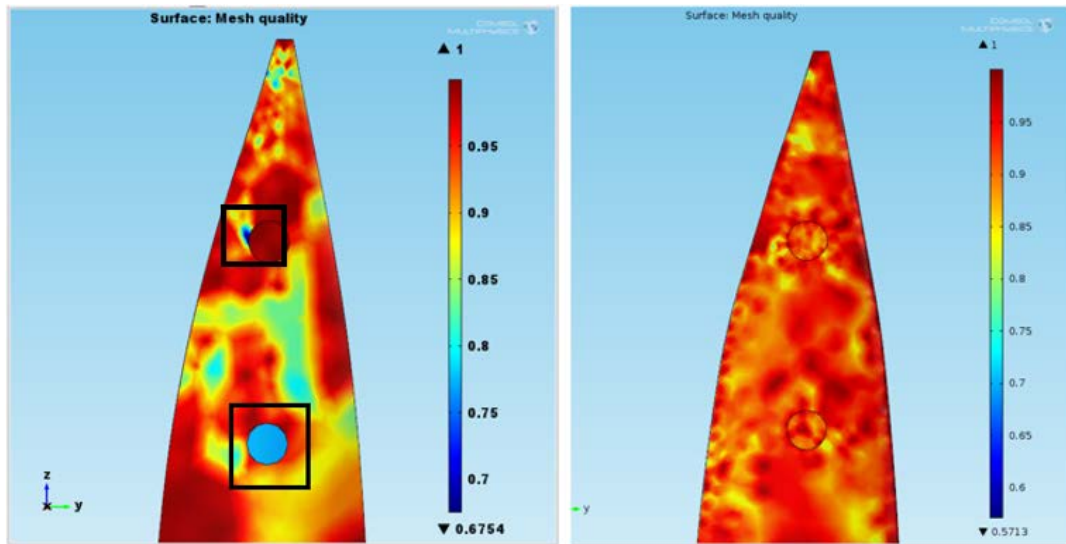
Figure 95 - Comparison of mesh quality among reference model (Left) and current model (Right) for blade with Double 0.2 m round receptor

Few mesh inconsistencies were noted in this model as well. As seen in the left hand image in **Figure 95**, the bottom receptor is seen to have very low quality mesh (light blue circular mesh), whereas, there is also some inconsistency in a highly critical area adjacent to the top receptor (dark blue patch).

Comparison of the electric fields along trailing edge and leading edge of the models are given in **Figure 96** and **Figure 97** respectively. It can be seen that the graphs closely match each other, showing that the current model for the double 0.2 m radius round receptor has been successfully validated.
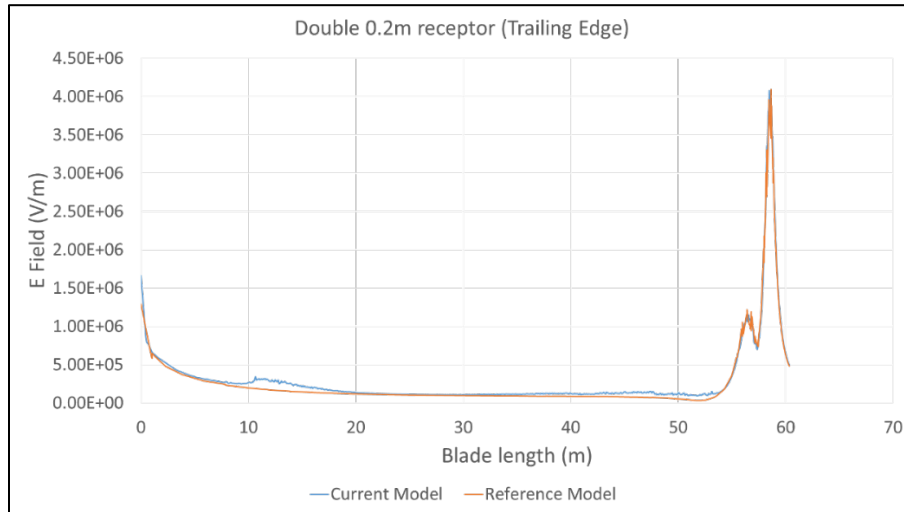
Figure 96 - Comparison of electric field along trailing edge of reference and current model (Double 0.2 m round receptor)
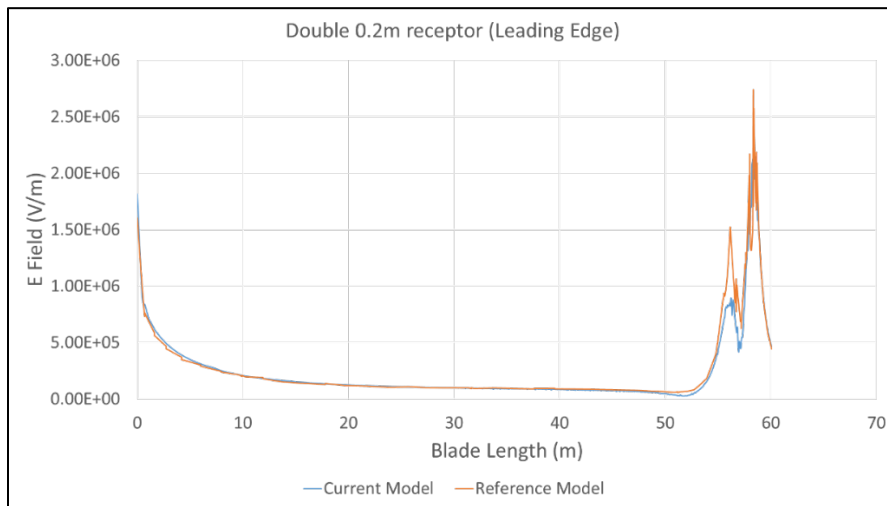

Figure 97 - Comparison of electric field along leading edge of reference and current model (Double 0.2 m round receptor)

`

Figure 98 shows a comparison of the peak electric fields between reference model and the current model for a blade without any receptors. The difference in peak electric field was observed to be 19.4%.
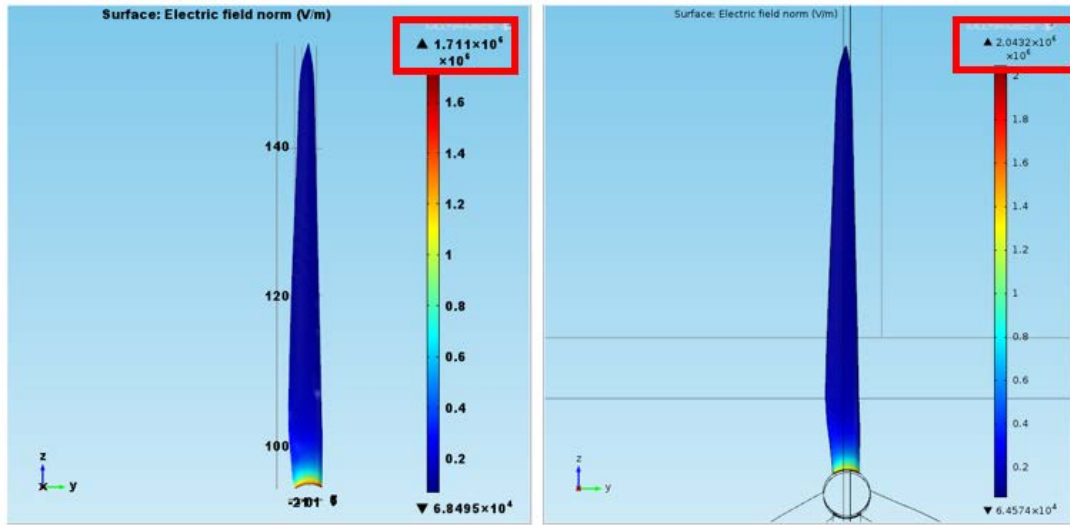

Figure 98 - Comparison of peak Electric field in: Left - Reference model (Wang et. al, 2017); Right - Current model (blade with no receptor)
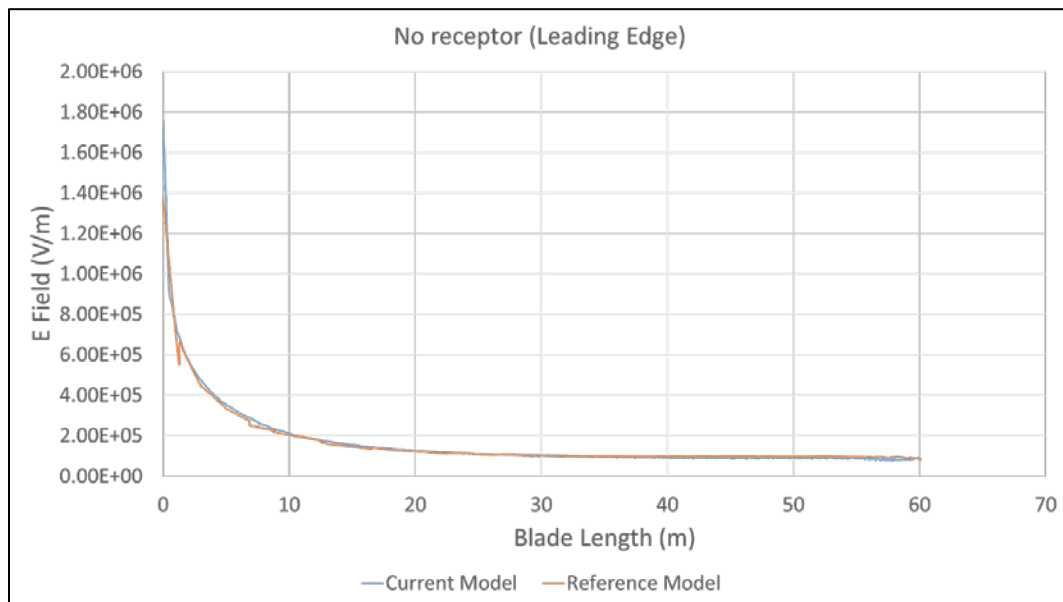

Figure 99 - Comparison of electric field along leading edge of reference and current model (Blade with no receptor)

`

The corresponding comparison between the electric field along leading edge is shown in *Figure 99*. Electric field data along trailing edge and leading edge for the reference model was found to be identical, and as such only one edge has been considered here for validation. It can be seen that there is almost a complete overlap of electric field among the two plots, thereby showing that the model has been validated.

`

APPENDIX B: COPYRIGHT PERMISSIONS

`

INVESTIGATION INTO CONDUCTIVE PATTERNS AND RECEPTOR DESIGNS FOR EFFECTIVE LIGHTNING INTERCEPTION

By SIDHARTH ARUNKUMAR